Fractal-Based Texture Segmentation of Digital X-Ray Mammograms

by

Pamela Karen Gurski

B.Mus., University of British Columbia, 1980

Extended Studies Dipl. Computing Science, Simon Fraser University, 1983

THESIS SUBMITTED IN PARTIAL FULFILLMENT OF
THE REQUIREMENTS FOR THE DEGREE OF
MASTER OF SCIENCE

in the School

of

Computing Science

SIMON FRASER UNIVERSITY
May 1991

Approval

Name: Pamela Karen Gurski

Degree: Master of Science

Title of thesis: Fractal-Based Texture Segmentation of Digital X-Ray Mammograms

Examining Committee:

Dr. Ze-Nian Li, Chairman

Dr. Brian V. Funt
Senior Supervisor

Dr. Ronald Harrop
Supervisor

Dr. Thomas Calvert
School of Computing Science
Faculty of Applied Science
Simon Fraser University
External Examiner

May 16, 1991
Date Approved

PARTIAL COPYRIGHT LICENSE

I hereby grant to Simon Fraser University the right to lend my thesis, project or extended essay (the title of which is shown below) to users of the Simon Fraser University Library, and to make partial or single copies only for such users or in response to a request from the library of any other university, or other educational institution, on its own behalf or for one of its users. I further agree that permission for multiple copying of this work for scholarly purposes may be granted by me or the Dean of Graduate Studies. It is understood that copying or publication of this work for financial gain shall not be allowed without my written permission.

Title of Thesis/Project/Extended Essay

Fractal-Based Texture Segmentation of Digital X-Ray Mammograms.

Author: _____
(signature)

Pamela Karen Gurski
(name)

24 June 1991
(date)

Abstract

Annually across North America approximately 150,000 women are diagnosed as having breast cancer. In British Columbia about 500 women die each year due to the disease. Mammography, x-ray imaging of the breast, is the primary screening and diagnostic tool available for the early detection of breast cancer and other forms of breast disease. To diagnose breast cancer in mammograms the radiologist looks for several specific textural indicators which indicate a growing cancer.

One particular textural model which has received recent interest, especially for its ability to model natural shapes and forms, is that of fractals. This thesis investigates fractal theory as a method of texture analysis and assesses the potential of using fractal-based texture segmentation to identify breast disease in digitized standard film mammograms.

This research focuses on the ability of the fractal model to detect known tumours, cysts and microcalcifications. The effect of various implementation methods, algorithmic noise removal and mask size on the fractal dimension calculations and image segmentation is outlined. A quantitative and qualitative analysis of synthetic and patient images is presented. Finally, cases where fractal-based texture analysis is successful and where it fails are reviewed.

Dedication

To my parents Edward and Eleanore Sauder,

my husband Don,

and my daughter Stephanie.

Acknowledgments

I would like to thank my Senior Supervisor, Dr. Brian V. Funt, for suggesting mammography as an area of radiography in which fractal analysis would be of interest and benefit. I am particularly grateful for his insightful suggestions and expert technical advice on approaches to try when our first results did not turn out as expected.

I would like to thank my Supervisior, Dr. Ronald Harrop, for his mathematical expertise, for his constructive critiques of my work, and his constant encouragement. I am particularly grateful for the generous use of his PET development lab and SPARC station so that I could complete the photographs used in the thesis. I am also grateful to fellow graduate student Ms. Kim Adamson-Sharpe who suggested using her 'Color-Map Editor' software to display the x-rays on the Sparc station.

I would like to thank Dr. D.M.F. McIntosh of Edmonton, Alberta for generously supplying the series of mammograms, and Dr. Heather McNaughton of Eagle Ridge Hospital, Department of Radiology and Dr. Douglas E. Read of Coquitlam, B. C. for supplying the chest x-rays.

Finally, my grateful acknowledgments go to my husband for his financial and moral support, to my parents who looked after my preschool daughter, and to my daughter who enjoyed seeing me do "school work".

Table of Contents

List of Tables

List of Figures

List of Equations

Chapter 1

Introduction

1.1 Motivation

Annually across North America approximately 150,000 women are diagnosed as having breast cancer. In British Columbia about 500 women die each year due to the disease [Knic90]. Although curable when detected in the early stages, breast cancer is the leading cause of cancer deaths among women 30 years and older [SiHo71] [ZhGo88].

1.1.1 Screening Mammography

Since the mid-1960s mammography—x-ray imaging of the breast—has been the primary screening and diagnostic tool used in the detection of breast cancer and other forms of breast disease such as cysts and fibroadenomas [SBDS86] [CDVM87] [CBRE88] [LLBi88] [Mosk88]. It is the only proven method of detecting nonpalpable breast cancers, and consistently detects a significant number of breast cancers at an earlier stage than any other method [GBKS87] [Mosk87].

Generally, small cancers are not large enough to be felt as breast lumps. Studies indicate [Feig79] [ZhGo88] [Knic90] detection rates by physical examination alone do not approach those of mammography until carcinomas reach a size of 2 to 3 centimetres in

diameter, by which time 65 percent have metastasized and spread to involve regional nodes. Detection of breast cancer prior to nodal involvement, when it is still clinically localized, increases the survival rate to 85 percent at five years. Detection at the time of nodal involvement reduces the five year survival rate to 53 percent. The prognosis worsens dramatically as the carcinoma enlarges to two or three nodes and begins to spread to other parts of the body. The average three year survival rate with untreated breast cancer is approximately 40 percent; at five years the survival rate drops to 18 to 20 percent.

A cancer found before it reaches one centimetre in diameter may be treated by lumpectomy—surgical removal of just the cancerous tissue, rather than mastectomy—removal of the entire breast [MASR84] [HHKi85] [VZLu86]. Benefits of early detection not only include increased survival rate but the possibility of functional breast reconstruction which may alter the patient's attitude to therapy and treatment. The basis for early detection is long-term survival—a woman who has a small carcinoma removed has a much better chance than a woman who has removal of a large breast cancer.

Since early detection is imperative and because x-ray dosages required by modern mammography equipment are low, the American College of Radiology recommends all asymptomatic women over 40 have a routine mammogram every 2 years and annually after age 50 [Whit84] [GBKS87] [Mosk88]. As a screening procedure, it has been anticipated that mammography will reduce deaths due to breast cancer by one third and perhaps by as much as 70 percent. Consequently it is becoming more widely used as a mass screening procedure [SBDS86] [CDVM87] [GBKS87] [LLBi88] [Knic90], as exemplified by the recently implemented Breast Screening Mammography Program of British Columbia.

Screening mammography is limited by a number of factors the most significant being the *method of analysis*. Currently mammographic analysis is performed manually by a radiologist using a magnifying glass to scan the film transparency carefully over a lightbox. The radiologist looks for visual indicators or *diagnostic signals* that indicate a growing cancer. Since many of the indicators involve very fine details, manual analysis of mammograms is labour intensive. Table 1.1: Radiological Signs of Breast Cancer lists the diagnostic signals most commonly associated with cancer. While these visual signs often reflect cancer that is locally advanced, emphasis is currently being placed on the less obvious signs such as subtle changes in breast architecture or mammographic texture that may signify the pre-clinical stages of cancer [GBCo87].

To overcome these problems and to aid radiologists in their diagnosis, it is desirable to develop computer-aided mammographic image processing and analysis tools which extract as much information as possible from mammograms. With computer processing of digital mammograms, the opportunity presents itself, as it has for other types of diagnostic x-ray [Conn85] [SSWA85] [CDVS87] [FaOl87] [GDMa87] [Rabk87] [DaFo88], to enhance and compare mammograms in ways impossible even for the eye of the best-trained radiologist.

1.1.2 Computer-Aided Mammography

A number of automated prescreening methods have been suggested for mammography which utilize techniques in image processing and pattern recognition. Most of this work has been aimed at the detection of breast lesions and microcalcifications. The identification of breast lesions has been the focus of [Wins67] [AcGo72] [KOSk77] [SWGS77] [HSAA79] [GRRW87] and [LLBi88]. Approaches have included: *(i)* using

RADIOLOGICAL SIGN	*COMMENTS*
high density tissue	*large areas of light gray or white known as lesions*
spiculation	*a fuzzy texture around an area of high density*
microcalcifications	*sand-like bright spots that appear in clusters*
lesion texture	*homogeneous lesions are likely benign; non-homogeneous are likely malignant*
lesion density	*lesions less dense than surrounding tissue are likely non-malignant; denser lesions are likely malignant*
nipple retraction	*indicates a subcutaneous reaction causing the nipple to be drawn towards the lesion*
ductal prominence	*prominent ducts extending from a lesion towards the nipple strongly suggests malignancy*
skin thickening	*indicates a subcutaneous reaction where the skin surface is drawn towards a lesion*
asymmetry	*structural differences such as size and shape between breasts*

Table 1.1: Radiological Signs of Breast Cancer[1]

four measures of malignancy—calcification, spiculation, roughness and area-to-perimeter ratio—to develop pattern classification techniques to categorize suspicious areas [AcGo72]; *(ii)* distinguishing benign and malignant lesions based on intensity distributions [SWGS77]; *(iii)* comparing textural and shape parameters in the left and right breast images [HSAA79]; and *(iv)* template matching schemes to detect circumscribed masses [LLBi88].

---

1 This table has been compiled from several sources including [Lama85], [AWNB87], [GBCo87], [Mosk87] and [CBRE88].

Microcalcifications, which sometimes appear in large numbers and clusters around a developing tumour, provide one particularly obvious radiological indicator of cancer. Approaches to microcalcification identification have included: *(i)* quantification of the shapes of the calcifications using piecewise linear discriminant functions [WMCT75]; *(ii)* using gray-level statistics and measures of brightness and compactness [Spie79]; *(iii)* adaptive local contrast and feature enhancement [RaNg86]; and *(iv)* spatial filtering to suppress the background while using signal-extraction techniques based on the physical characteristics of microcalcifications to enhance their presence [CDVM87].

1.1.3 Texture in Mammography

Image texture can be considered a spatial arrangement of different gray-level intensities and is the primary characteristic used in the analysis of radiological images. The spatial arrangement of the differing intensities within a particular region of an image may be more or less regular, may be random, or may have a linear, structural or probabilistic dependency of one upon another. Frequently the spatial arrangement is *qualitatively* described as having the properties of fineness, coarseness, smoothness, granulation, randomness, lineation, or being mottled or irregular.

In mammography the radiologist evaluates image texture within an area of the film image by looking at the composition of the fine detail and the overall spatial organization of this detail. Any changes in either the linear or coalescent densities permits the radiologist to differentiate between normal and abnormal areas. These textural changes are frequently described using the above qualitative terms and are the basis of several of the radiological indicators mentioned in Table 1.1.

In computer-aided mammography several researchers have used changes in image texture to classify physical areas of an image. In particular [KSFW79] [MCOB85] [CSHJ90] have used texture-based classification schemes to predict the risk of developing breast cancer. While using different methods, these programs are all similar in that they assess the radiographic densities of mammographic parenchymal patterns and determine a statistical correlation which best coincides with a specific risk category of the *Wolfe Classification System* [Wolf83]. [KSFW79] analyzed the gray-level variations of digitized mammograms to determine which statistics best represented a particular texture classification. [MCOB85] investigated the automatic determination of a *risk coefficient* using both global and local parameters as measures of risk. Unfortunately these parameters did not provide enough discriminant information to permit accurate classification among various mammographic patterns. The application of *fractal* theory to radiological images is evident in the recent work of [CSHJ90]. Fractals measure the degree of roughness of a surface, and [CSHJ90] correlates globally-derived fractal dimension values to specific risk categories in the Wolfe system.

1.2 Scope

This thesis investigates fractal theory as a method of texture analysis, and in particular assesses the potential of using *fractal-based texture segmentation* to identify breast disease in digitized standard film mammograms. A key premise is that, as projected on a two-dimensional x-ray, a carcinoma has a texture (i.e., pattern of gray-level intensities) which is distinct from the surrounding normal tissue, and that any changes between normal and abnormal tissue can be described by a corresponding change in fractal dimension. Thus, changes in the fractal dimension should correspond to the anatomical features of the breast—normal and abnormal—and may be used to segment the image.

A basic problem in the application of fractal theory to mammography is the estimation of the *fractal dimension* or D value. Several methods, [Pent84] [LOKS86] [LOKW86] [Dell87] [OhLu87] [Vern87] [ChDF89] [KeCh89] [KCRW89] [CSHJ90], have been presented for calculation of this parameter. In order to simplify our evaluation process, we chose to implement Pentland's *Intensity Statistics Method* for estimating the fractal dimension [Pent84]. This method calculates the fractal dimension of a small area—mask—surrounding each pixel directly from the gray-level intensities of the x-ray. From these calculations a *fractal image* is created in which the gray-level intensities are proportional to a particular D value. Texture segmentation is via the fractal image.

To assess the effectiveness of fractal-based texture segmentation in mammography this research focuses on the following issues:

(i) The ability of the fractal estimator to detect both large- and small-scale anatomical features. The objective is to detect features that are not obvious to the human eye. It is also imperative that details that are clearly visible are not lost. Two implementations of the fractal estimator will be evaluated.

(ii) Determination of an appropriate mask size for detecting both large- and small-scale anatomical features. Several researchers [Vern87] [Dell87] [StHa88] have indicated that small mask sizes are more sensitive to noise, while larger mask sizes lead to averaged or smoothed D estimations. Both of these situations will be investigated to determine which will produce more reliable results.

(iii) An investigation of the effect of noise on the fractal calculations and the subsequent impact on fractal-based texture segmentation.

(iv) An investigation of the effect of algorithmic noise removal prior to performing fractal dimension calculations. In particular, can noise removal be used prior to

fractal-based texture segmentation and still produce consistent and reliable results?

(v) An evaluation of the potential of combining data from the original gray-level x-ray with data from the fractal image as a means for enhancing fractal-based texture segmentation.

1.3 Strategy

Computer-aided mammography can be broken into three stages: the image formation stage, the image acquisition stage, and the image analysis stage as shown in Figure 1.1. Each of these processes is based on particular physical models and has an associated series of assumptions and limitations. These assumptions and limitations directly affect the behaviour of the fractal model as a texture segmentation technique in radiology.

The first two stages, the image formation and acquisition stages, will be explained in Chapter 2. Penetrating radiation systems and radiographic image formation, including image, quantizer and sensor noise are discussed.

Chapters 3, 4 and 5 are concerned with the image analysis stage. Chapter 3 deals with fractal theory; particular emphasis is placed on the application of fractal analysis as it pertains to radiology. Chapter 4 presents the experimental outline and discusses the algorithms used in the experiments. Chapter 5 presents and discusses the results of the experiments. Chapter 6 presents the conclusions and suggests future research directions.

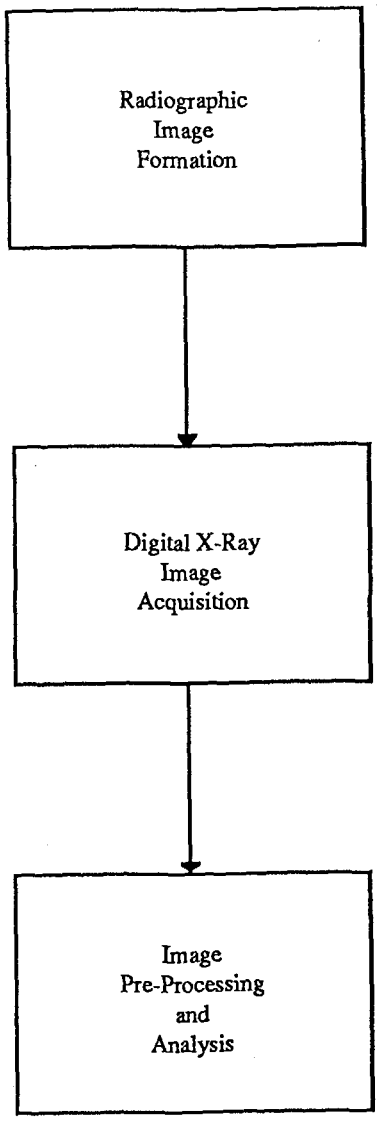

Figure 1.1: Three stages of computer-aided mammography

Chapter 2

Diagnostic X-Ray Imaging

This chapter discusses key characteristics of radiographic image formation and digital x-ray image acquisition which have been found to affect fractal-based texture segmentation of digital x-rays.

2.1 Radiographic Image Formation

The x-rays used in conventional radiography are produced by passing a high voltage, usually between 50 and 150 kilovolts, across two terminals in an evacuated tube causing free electrons to hit a tungsten target. A small portion of the resulting x-ray beam escapes through an opening in the surrounding metal casing. It then passes through the object of interest and is recorded on film.

2.1.1 Film Images

X-ray image formation is a chemical process in which silver particles are deposited on film in response to x-ray exposure. A photographic effect results when film is placed between two fluorescent screens that emit light on exposure to x-rays. The light emitted by the fluorescent screens intensifies the effects of the x-ray beam and causes the blackening of the developed film. The type of phosphor coating on the screen, its x-ray absorption

characteristics and its efficiency in converting absorbed x-ray energy to light determine the sensitivity of the screen. The amount of metallic silver deposited on a particular area of film in response to the quantity of light emitted by the flourescent screen is referred to as the *film density* [Yu83]. For maximum sensitivity, the spectral response of the film must be matched to the light emitted by the screen.

According to [AnHu77] [Yu83] [RaSh87] [Loats88], the capability to detect or reproduce biomedical detail is limited by the silver grains' response to x-ray exposure and by the microstructure of the film. Essentially silver grains have two states: highly developed (i.e., exposed) and marginally developed (i.e., unexposed). Due to the limited number of responsive silver halide grains per surface area of film, there is a upper limit on the amount of energy that is detected at a particular location on the film surface. This is known as the *saturation level* of the film. After saturation has been reached, further exposure to x-rays does not significantly alter the local density of the image; it only exposes film grains more distant from the source of the emissions. Even in areas of film that are not exposed to any x-rays, reactions occur between the developer and the silver grains. This produces a background density or *fog level* which causes a loss of image sharpness and resolution. Thus two boundaries—the *fog level* and the *saturation level*—define the limits of film density.

Another factor also contributing to loss of image sharpness and resolution is *film-grain noise*. According to [AnHu77] and [Yu83], a fundamental randomness exists in the deposition of silver grains. They are randomly distributed with respect to size, shape and location in the film emulsion even when identical conditions of exposure and development exist.

While various mathematical models exist to explain film-grain noise, it is generally agreed that film-grain noise is aperture size dependent, is not constant but varies with the average film density in a region of film, and can be approximated by a random process [AnHu77] [Yu83]. Unfortunately the imaging characteristics of the x-ray systems which produced the films used in this thesis are not known. Let it suffice to say that several of the x-ray films contained a significant amount of film-grain noise. As suggested by [AnHu77], we approximated film-grain noise by a random noise process and used this in our experiments which assessed the impact of noise and its algorithmic removal on the fractal model.

2.1.2 Image Projections

The image on an x-ray film is two-dimensional. It is a *shadow projection* of the interior of the object—all the structures along the path of the beam are projected onto the same point of the film. The shadows are produced by four basic densities—*gas*, *fat*, *soft tissues* and *calcified structures*. According to [AWNB87] x-rays passing through air are the least absorbed and cause the most blackening of the film. Calcium absorbs the most x-rays, therefore bones and other calcified structures appear white. Soft tissues, such as the sold viscera, muscle, blood and bowel wall, all have the same absorptive capacity and appear the same shade of gray. Fat absorbs slightly less x-rays and appears a little blacker than the other soft tissues. Radiologically, the greater the *differential absorption* of the tissues the more satisfactory the film contrast, which in turn determines the visibility of structures and of disease.

According to [Lama85], x-ray images embody three principal characteristics: they are *conical*, *composite* and *contrasted* projections. They are *conical* projections because the

x-ray beam extends in different directions from an apex and then passes through the object of interest to be recorded on film. Images are *composite* because each portion of the beam is projected onto a single given point of the film. In other words, for a particular (x, y) location in the film image the gray-level intensity at that point is due to a summation of the point contributions along a particular beam path through the object [AnHu77]. Images are *contrasted* projections because each point on the film shows a darkening depending on the intensity of the rays received (i.e., as determined by the density of the object) following transition through the tissue.

The weakening of the x-ray beam due to the density of the object is referred to as *attenuation* [AnHu77]. Projection geometry and radiation scatter also modify the x-ray beam and consequently affect the film image. Radiation scatter occurs when the x-ray beam is scattered from its path resulting in a deflection of radiation about a point. Projection geometry dictates that edges not directly in the path of the radiation source are spread out.

Thus, the developed x-ray image as we view it is a projection of all point contributions from the structures of the object along a path of the beam—gas, fat, soft and calcified tissues—including modifications of the x-ray beam due to density, radiation scatter and projection geometry. The amount of information present on an x-ray image is related to the differential absorption of the tissues which dictates the sharpness of the image, its clarity and its contrast.

2.1.3 Mammogram Image Formation

Mammography differs from conventional radiology in that low energy x-rays in the 20 to 35 kilovolt range are used in an effort to reduce the possible harmful effects of

repeated exposure to high voltage ionizing radiation [AWNB87] [GBKS87] [Mosk87] [Mosk88]. The breast, classed as a soft tissue, is composed mainly of fat and fibrous connective tissue. When projected on film, fat is clear while connective and fibrous tissue is opaque. The variable amount of fatty tissue (a function of the breast's thickness) and the relationship between fatty and connective tissues determine the structures seen on projection. Together these two extremes produce the image of a mammograph.

Unfortunately, due to its composition, the breast has weak differential absorption. In addition, the small differences in density between normal and tumourous tissues create relatively weak contrast between tumour areas and image background. The presence of anatomical structures (e.g., ducts and glands) further increases the background variations which in turn decrease contrast. A further reduction of contrast also occurs from the limited capability of photographic film to develop maximum contrast over an extended range of exposure values; the high x-ray penetration of the objects; scatter radiation; image blurring produced by the finite size of the focal spot; the thickness of the intensifying screen; and improper procedure and poor film processing techniques. The result is poor quality mammogram images which exhibit reduced contrast, sharpness and resolution.

According to [Lama85] [AWNB87] [GBKS87] [Mosk87] [CBRE88] [Mosk88], reducing the thickness through which the x-ray beam passes by compressing the breast enhances the clarity of structures seen on the projection images. Breast compression is also performed for a number additional reasons: it enables a reduction in the x-ray dose; it improves image contrast due to the reduction in scatter radiation; and it improves the sharpness of the film image because the breast is closer to the receptor. The improved quality of image obtained by using breast compression has made this the norm in mammography.

2.2 Digital X-Ray Acquisition

Digital x-ray acquisition seeks to provide accurate, reliable quantization of x-ray images which extracts as much data as possible from the original film image. Figure 2.1 shows the major components of the acquisition system used in this thesis. Quantization of x-ray images is performed using a sensor, in this case a video camera, that converts the gray-level intensity variations of the x-ray into an analog electrical signal. A signal converter—in our case the IIS image processor—transforms the analog signal into digital form for computer processing and analysis.

According to [Loats88] the quantization process imposes an inherent accuracy limit on the representation of the gray-scale information present on digitized x-rays. This limit is principally determined by the quantization capabilities of the acquisition device and the sensor noise characteristics of the system.

The quantization capabilities of the acquisition device are determined by two factors: the smallest discernible detail in the original x-ray image, and the spatial resolution capabilities of the video camera/analog-to-digital (A/D) converter system. We have already mentioned how the details of the original x-ray images are determined by several factors. The resolution capabilities of our particular system are discussed in Chapter 4.

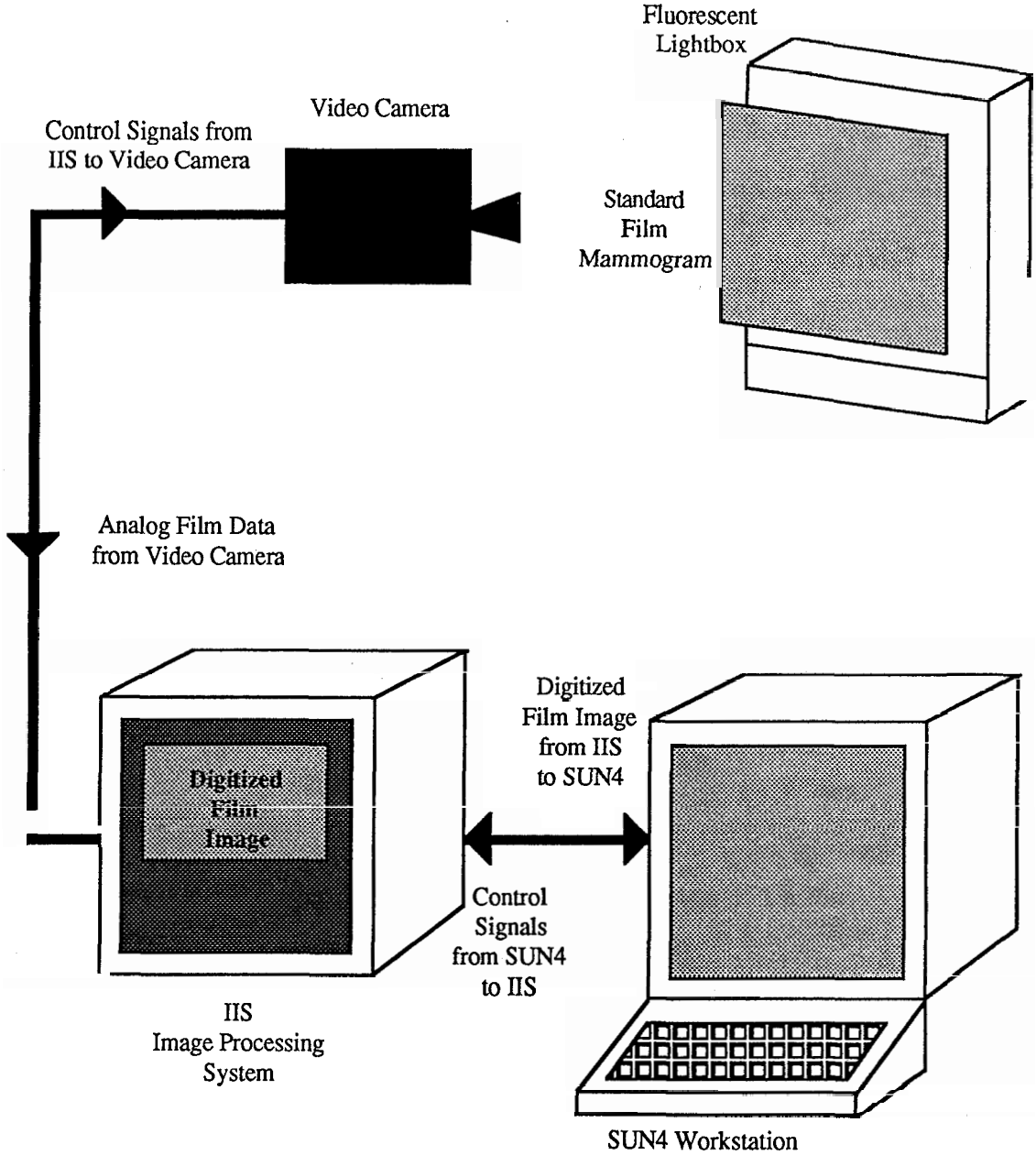

Figure 2.1: Digital X-Ray Image Acquisition System in the Vision Laboratory of the School of Computing Science

The sensor noise characteristics of the acquisition system impose a further accuracy limit on the representation of the gray-scale information present on the digitized x-ray. [Loats88] points out that noise in a digital image system comprises *image*, *sensor* and *quantizer noise*. Image noise refers to the visual quality of the film images, which as previously mentioned is determined by several factors. Sensor noise arises primarily from the video camera, whereas quantizer noise arises primarily from distortions in either the optical system of the digitizer or the A/D converter. As a result, digitized x-ray images often have degraded edge and texture definition which may significantly impair accurate diagnosis and have impact on the diagnostic value of the processed image. Consequently, a number of image preprocessing and restoration techniques have been developed to improve the quality of digitized images.

2.2.1 Image Preprocessing and Restoration

Image preprocessing and restoration techniques fall into two classes: geometric and radiometric. Geometric techniques include corrections to compensate for spatial non-uniformities introduced by the sensor. The distortions may be on the sensor chip itself or may arise when the analog signal is converted to digital format. Chapter 4 discusses the geometric corrections performed in this thesis to compensate for spatial distortions which are present in this particular digital image acquistion system.

Radiometric techniques include: noise removal, and the enhancement of contrast, edge and texture quality. These techniques have been the focus of considerable research [GoRa84] [Selz84] [DBGo86] [DLGo86] [RaNg86] [FaOl87] [DhLe88] [LLBi89]. They are aimed at improving the quality of x-ray images by bringing out the unseen or barely seen features and textures for better human visibility without an additional x-ray dose to the

patient. Unfortunately the selection of suitable enhancement functions for mammography is difficult—often these algorithms intensify the noise and background variations so that the desired features cannot be clearly seen. Recently [LLBi89] presented a comparison of edge-preserving noise removal and contrast enhancement methods for specific use in mammography. Several of these algorithms seem to enhance the diagnostic information without intensifying noise or other background variations. From this comparison the *Kth-Nearest Neighbour Method* was chosen to enhance the contrast and remove noise from the digitized x-rays.

2.3 Summary

X-ray images are shadow projections of the interior of the object where all structures along the path of the beam are projected onto the same point of the film. The relatively weak differential absorptive capacity of the breast makes compression necessary in order to enhance the clarity of the internal structures and improve image contrast. Radiologists interpret changes in relative image intensity—directly related to the strength of the x-ray received—as changes in image texture indicative of possible breast cancer.

Reproduction of radiographic detail on x-ray film is governed by the initial quality of the film x-ray, and by the accuracy/inaccuracy of the imaging system. A significant amount of noise may be present in the film image. In addition, quantizer and sensor noise are introduced during the digitization process. Image preprocessing and restoration techniques are utilized to compensate for spatial distortions and for noise removal.

The effect of noise, and its algorithmic removal, on the behaviour and stability of the fractal model requires investigation. The experiments in chapter 5 attempt to determine

its impact on the fractal model as it pertains to texture-based segmentation of radiological images. The next chapter, Chapter 3, will present the Fractal Brownian model and review its application to radiology.

Chapter 3

Fractals in Radiology

An important goal of texture-segmentation research is the identification of texture models that facilitate the discrimination of various textures. One particular textural model which has received recent interest, especially for its ability to model natural shapes and forms, is based on a relatively novel class of mathematical functions known as *fractals*. Fractal geometry has received considerable attention as a model for natural phenomena in physiology and medicine, and as a means of texture description and segmentation of medical images.

This chapter discusses fractals in biology and physiology, basic concepts of fractal theory and in particular the fractional Brownian motion model as it has been applied to scene analysis, image segmentation and radiography.

3.1 Fractals in Biology and Physiology

The complex interrelations between size, scale and shape to form, function and development are commonly encountered in anatomy and physiology. Exploration of these interrelations has led to the formulation of several scaling relationships which describe how proportions vary as an animal grows. According to [WeGo87] these relationships rely on the assumptions that biological processes are *continuous*, *homogeneous* and *regular*.

However, observation and experiment have suggested the opposite—most biological systems are *discontinuous*, *nonhomogeneous* and *irregular*.

Seizing upon the fact that many anatomical structures show elements of both similarity and randomness over a range of scales, researchers have used fractal theory to describe the behaviour of several systems in physiology. These systems include: the different sized tubes of the vascular system and its branching throughout the body; the bile duct system; the urinary collecting tubes in the kidney; the brain; the lining of the bowel; the nervous system; the placenta; the heart with its system of coronary arteries and veins held together by branching strands of connective tissue; the heart's His-Purkinje system—a network of nerves which conduct electrical impulses; and the various branchings and tube sizes of the lung [WeGo87].

Research has also suggested that as well as describing healthy physiological variability, alterations in fractal scaling (i.e., fractal dimension) may underlie a number of diseases including congestive heart failure, fetal distress syndrome and certain types of chronic leukemia. The notion that alterations in fractal scaling may underlie disease and the possibility that such alterations may be detected on radiographs is key in the formulation of this thesis.

3.2 What is a Fractal?

Fractals form a class of mathematical functions that express the geometrical properties of some sets. The mathematician Benoit Mandelbrot coined the word *fractal* to describe complex geometric forms that mimic the randomness found in nature and yet exhibit a paradoxical combination of variability and order. Mandelbrot elegantly states

> "Clouds are not spheres, mountains are not cones, coastlines are not circles, and bark is not smooth, nor does lightning travel in a straight line."[2]

In classical Euclidean geometry objects are often defined by parametric equations specifying their surface or volume. In classical geometry these objects have an *integer dimension* or *topological dimension* T. A point is referred to as having zero dimension, a line one dimension, an area two dimensions and a solid three dimensions. The term *fractal* refers to objects possessing a non-integer or *fractional dimension* D, where the fractal dimension is greater than the topological dimension. The dimension of a fractal is related to the way it scales and is a measure of how well it fills the Euclidean space in which it is embedded. As the fractal dimension increases the irregularity of the object increases. This corresponds to our intuitive notion of *roughness* or texture—the lower the D value the smoother the object, the higher the D value the rougher the object.

According to [GoWe87] fractal objects possess some interesting properties—*heterogeneity, self-similarity* and the *absence of a well-defined or characteristic scale of length.* Fractal curves, surfaces and volumes are neither smooth nor homogeneous. Examination at increasingly stronger powers of magnification reveal levels of detail not present in the classical forms. Seemingly endless levels of irregular structure emerge—wrinkles on wrinkles on wrinkles—in which the small scale structure of the fractals resembles the large scale form, that is they are *self-similar.*

Self-similarity is the basic property which is the key to real-world modeling of natural objects. According to [Voss85] and [StHa88] natural objects exhibit a *statistical*

---

2 Mandelbrot, B. B., *The Fractal Geometry of Nature*, New York: W. H. Freeman and Company, 1983, p. 1

self-similarity rather than an a *exact* self-similarity. An object possessing *exact* self-similarity is composed of many copies of itself, with possible translations and rotations, each of which is scaled down by a specific ratio at all positions of the object. An object displaying *statistical* self-similarity is described by a statistical law that governs the self-similarity of probability distributions of specific properties, such as gray-level intensity, measured at different scales. The degree of self-similarity is directly related to the fractal dimension. The statistical model most frequently assumed for this purpose is fractional Brownian motion.

The fractional Brownian motion model (fBm), introduced by Mandelbrot and Van Ness [MaVN68], is an extension of the concept of *Brownian motion* that plays an important role in physics and mathematics. This model regards naturally occurring rough surfaces as the end result of *random walks* which are the basic physical processes in our universe. A characteristic of these processes is that they modify shape through local action and after innumerable repetitions they typically produce a fractal shape. Application of the fBm model has been extended to the intensity surfaces of film images by Pentland in [Pent84] and is of particular interest to this thesis.

3.3 Fractional Brownian Motion and Film Images

Pentland's research uses fractional Brownian motion to explain how natural objects and textures are mapped onto a two-dimensional film image intensity surface. Several researchers, [Dell87] [Vern87] and [ChDF89], have used Pentland's fractal model for the texture analysis of radiographs. Like [Dell87] [Vern87] and [ChDF89] this thesis assumes the applicability of Pentland's model for the analysis of x-ray film images. The following

discussion is a synthesis of the method as presented by Pentland. Detailed discussions are found in [Pent84] and [Pent85].

3.3.1 Fractal Brownian Functions and Surfaces

A function I(z) is a fractal Brownian function of Hurst coefficient H if the cumulative distribution function F(y) defined by

$$F(y) = Pr\left(\frac{I(z + \Delta z) - I(z)}{\| \Delta z \|^{H}} < y \right) \tag{3.1}$$

where Pr is a probability measure, z is a vector, Δz is a given increment of z, and the parameter H being constant is independent of z and Δz. If the topological dimension of the domain of z is T, then the fractal dimension D of the graph described by I(z) is

$$D = (T + 1) - H \tag{3.2}$$

If H = 1/2 and F(y) comes from a zero-mean Gaussian with unit variance, then I(z) is a classical Brownian function.

Interpreting z and Δz as vector quantities allows an extension to two or more topological dimensions. When z is scalar, the fractal dimension D of the graph described by I(z) for T = 1 is

$$D = 2 - H \tag{3.3}$$

In digitized images z is a vector of the spatial coordinates *(x, y)*, I(z) is a function representing surface behaviour (i.e., the gray-level intensity) at the spatial coordinates z, and Δz is the separation distance between a pair of points I(z) and I(z + Δz). In this context, since T = 2, the fractal dimension of the image intensity surface is

$$D = 3 - H \tag{3.4}$$

In practice when D = 2.0 the surface is a flat plane and when D = 2.9 the surface is a very rough stalagmite covered plane.

Since fractals, like most mathematical abstractions, can only approximate natural objects over a range of physical parameters, a reasonable definition of a fractal Brownian surface is a continuous function that obeys the statistical description given by equation (3.1) where z is a two-dimensional vector at all scales and values of Δz are between some smallest (Δz_{min}) and largest (Δz_{max}).[3] Practical limitations dictate the lower bound not be less than the smallest constituent particle (i.e., the size of the projected pixel), while the upper bound not exceed the size of the object of interest (i.e., the size of the examined surface patch or mask size).

3.3.2 Pentland's Intensity Statistics Method

Pentland's method estimates the "fractal dimension" of a natural surface from an image intensity representation of a film image of that surface, realizing that the dimension may not be constant across the whole surface. His method computes the average gray-level

---

3 Pentland, A.P., "Fractal-Based Description of Natural Scenes", *IEEE Transactions on Pattern Analysis and Machine Intelligence*, Vol. PAMI-6, No. 6, Nov. 1984, p. 663

mean and variance of pixel pairs over decreasing scales within a local surface area (i.e., mask) surrounding a particular *(x, y)* location on the surface of the film image. The logarithms of the averaged mean and variance are then linearly regressed onto the logarithm of the discretized scale. From the linear regression and the parameter H, the fractal dimension of the mask is calculated. By calculating the fractal dimension for every point on the image surface, we get a measure of texture as it varies from point to point. The resultant fractal surface description provides a means of describing and evaluating textural variations that occur on the film surface.

More specifically, to estimate the fractal dimension of an image, equation (3.1) can be rewritten according to [Pent84] as

$$E(|\Delta I_{\Delta z}|) \, \| \Delta z \|^{-H} = E(|\Delta I_{\Delta z = 1}|) \tag{3.5}$$

or

$$\| \Delta z \|^{H} = \frac{E\{|I(z + \Delta z) - I(z)|\}}{E\{|I(z + 1) - I(z)|\}} \tag{3.6}$$

where $E(|\Delta I_{\Delta z}|)$ is the expected value of the absolute value of the change of intensity for the range Δz.[4] To estimate H, and thus D, the quantities $E\{|I(z + \Delta z) - I(z)|\}$ are calculated for various Δz.

H is estimated by taking the logarithm of both sides of equation (3.6) to give

$$H \, \text{Log} \, \| \Delta z \| = \text{Log} \, (E\{|I(z + \Delta z) - I(z)|\}) - \text{Log} \, (E\{|I(z + 1) - I(z)|\}) \tag{3.7}$$

---

4 Given two points z = (x, y) and z' = (x', y'), the distance between the points or range Δz is obtained using the Euclidean distance formula $\Delta z = \text{sqrt}\{(x' - x)^2 + (y' - y)^2\}$

Equation (3.7) is then used as the basis for a linear regression of samples of Log ($E\{ | I(z + \Delta z) - I(z) | \}$) taken at different Δz, onto Log $\| \Delta z \|$. Using least-squares fit, H is the slope of the best-fit line given several data pairs. The fractal dimension is then calculated according to equation (3.4). It should be noted that linear regressions, and consequently this method, require a sufficient number of sample points to obtain reasonable results in terms of linear fit. Further discussion of this topic is found in Chapters 4 and 5.

3.3.3 fBm and the Imaging Process

Pentland's fractal model facilitates our understanding of how the imaging process maps a three-dimensional fractal surface shape onto a two-dimensional image intensity surface. [Pent84] indicates for specific conditions (i.e., the surface is a homogeneous[5] Lambertian[6] surface with constant illumination and albedo[7]) that:

(i) A three-dimensional surface which is fractal Brownian produces a film image whose intensity surface is fractal Brownian.

(ii) A linear transformation of a fractal Brownian function is a fractal Brownian function with the same fractal dimension.

(iii) The fractal dimension of a fractal Brownian function is invariant over transformations of scale.

(iv) If an image intensity surface is a two-dimensional fractal Brownian then the imaged three-dimensional surface must also be fractal Brownian.

---

5 Pentland states a homogeneous surface refers to natural surfaces that are of a similar composition or structure throughout and that its homogeneity may be determined from imaged colour.

6 Such a surface is commonly referred to as a matte surface.

7 Albedo refers to the fraction of incident light that is reflected by a surface.

Radiography differs from the photography used in Pentland's model in one important aspect: it does not map three-dimensional surfaces onto the film image, rather the x-ray formation process maps a shadow projection of the contents of a volume onto the two-dimensional image intensity surface (refer to 2.1.1 Film Images and 2.1.2 Image Projections). We assume that an imaged volume which is fractal Brownian produces a film image whose intensity surface is also fractal Brownian. Since photography and radiography use the same photochemical process to deposit the silver grains on the film surface, this assumption seems reasonable. This assumption allows us to apply Pentland's fractal theory to the analysis of x-ray film images and derive a fractal surface description.

For the analysis of medical images, the fractal surface description provides a means of relating textural changes to structures in the interior of the human body. Since an x-ray image is a shadow projection of the structure of the interior of the object, any changes in the structure of the interior of the object are projected as changes in texture on the film surface. Therefore, changes in the fractal dimension between different areas of the x-ray image are a function of the physical differences in image intensity and directly correspond to changes in the interior structure of the object. Assuming that an anatomical feature, such as a carcinoma, has a texture which is distinct from the surrounding tissue, then such textural differences should be evident by a corresponding change in the fractal dimension. For the purpose of texture-based image segmentation, the changes in the fractal dimension assist in determining the edges and segmenting the image; hence there is no need for edge detection in a formal sense. An advantage of fractal-based image analysis is that, if an image intensity surface is fractal, the fractal surface description alone may be sufficient to describe the image structure [Pent84] [Dell87].

3.4 Related Work

Researchers have used several fractional Brownian models including Pentland's for the analysis of a number of diseases in radiology. This section briefly discusses their findings as it pertains to this research.

a) Bone Diseases

The focus of [LOKS86] and [OhLu87] has been quantification of texture changes which occur in bone loss diseases such as osteoporosis. The researchers developed a Maximum Likelihood Estimator (MLE) for estimating H in the two-dimensional case from the power spectrum of digitized x-rays of the human calcaneus (heel).

Of particular importance to this thesis was the research into the behaviour of fBm in the presence of additive Gaussian noise. It was found that the effect of noise was not uniform. Even with signal-to-noise ratios of 30 dB significant estimation errors result, particularly for high values of H. This implies that surfaces which are smoother are more sensitive to noise than those that are rougher. Since the performance of the estimator H in noise is important, especially if one is attempting to make structural inferences about an object from the data, it was concluded that noise must be either removed from the data before processing or incorporated into the estimation model to achieve reliable results [LOSK86].

Other authors continuing the work on diagnosis of osteoporosis are [HKMS87] and [KHNM87]. Of particular interest was the use of the fractal dimension in combination with other statistics derived from the x-rays. Three textural features were estimated: the run

length statistics, the relative extrema density, and the fractal dimension. Together these estimators were used to determine bone loss. Favourable conclusions were reached regarding the appropriateness of digital image texture analysis and the usefulness of fBm in the analysis of radiographs.

b) Coronary Angiograms

In subsequent work, [LOKW86] extended the MLE to three dimensions and applied it to sequences of digital coronary angiograms for the purpose of fractal-based texture segmentation. The fractal dimension is used to separate dye-filled blood vessels from the background and used to create a gray-level fractal image where the intensity is related to D value. Unfortunately, these images are often difficult to interpret and poorly differentiated due to the behaviour of the background tissue (i.e., normal tissue).

c) Lung Diseases

[Dell87] and [Vern87] assess the effectiveness and limitations of fractal-based texture segmentation in x-rays of the human lung containing pathological nodes. The Intensity Statistics method is used to compute the fractal dimension and a fractal image was generated where intensity is a function of the D value. This image was then used for texture-based segmentation to indicate regions that are differently textured. Their results show that fractal images can point out differences between normal and pathological tissues.

Noteworthy is their investigation into mask size. Masks that are too small can give noise dependent D estimations. Masks that are too large can give averaged or smoothed D estimations. In these situations the fractal approach did not allow regions to be easily

segregated. However, [Vern87] points out that smaller mask sizes achieve a higher spatial resolution, which is important in the detection of pathological tissues especially very small tumours, and concludes that this behaviour confirms the appropriateness of employing small mask sizes.

More recently [Vehel90] has continued research on identification of lung diseases. Vehel's approach combines both fractal and integral geometry for the purpose of developing a computer-based classification system of pulmonary disease from SPECT images. This work provides additional confirmation on the appropriateness of applying fractal-based texture segmentation for the purpose of disease identification in radiological images.

d) Liver Disease

The goal of [Carg88] is the development of a fractal-based liver disease classifier from the power spectra of nuclear medicine scans. Nuclear medicine scans, like radiographic images, suffer image degradation due to scatter, attenuation, collimator and detector blur, and noise. Knowledge of the imaging system allowed corrections for image degradation in the fractal calculations. While the goal of disease classification differs from that of fractal-based texture segmentation, the compensation techniques developed by [Carg88] may be useful in future research (refer to Chapter 6).

e) Dental Radiographs

Application of fractal texture analysis to the segmentation of dental radiographs is the focus of [KCRW89]. The fractal dimension of the radiographs was estimated from the

Fourier power spectra. A three dimensional feature space—determined by the fractal dimension, radiograph intensities and the regression analysis correlation coefficient—was used to partition dental x-rays into bone, teeth or boundary areas. Noteworthy is the finding that the regression analysis has a degree of error, and that various regression techniques can significantly effect the accuracy of results, which is also corroborated by [StHa88].

f) Chest X-Rays

The work of [ChDF89] focuses on edge enhancement and segmentation of chest x-rays, and is similar in approach to this thesis. The Intensity Statistics method was used to calculate the fractal dimension of each pixel in the image, using a 7 x 7 pixel block centered on each respective pixel. A fractal image is created where the gray-level of each pixel corresponds to a specific D value between 2 and 3. The chest x-ray is clearly segmented into bone versus non-bone areas. The results of this work were used as a reference in verifying the results of this thesis.

g) Mammography

The development of a fractal parameter of risk for breast disease is the goal of [Cald90]. Fractal theory is used in the analysis of standard film mammograms to relate the Wolfe classification system to specific fractal dimensions. Measuring the radiographic density of the various breast tissue patterns, mammograms are differentiated into one of the four Wolfe classes (i.e., N1, P1, P2 and DY) on the basis of two independently calculated fractal-dimensions. The first is the average fractal dimension of the entire breast image; the second, a fractal dimension calculation performed on a region of interest adjacent to the

nipple. In contrast with the work of [Cald90], the goal of this thesis is the identification of possible lesion sites in the x-ray image through the use of fractal-based texture segmentation rather than the development of a fractal-based risk classifier.

3.5 Summary

As indicated in the literature review, the application of fractal theory to the analysis of x-ray textures has met with considerable success, particularly for tissues with great differential absorption. However, since soft tissues present weakly contrasted projections with poor differential absorption, a number of questions need to be addressed when applying fractal-based texture segmentation to mammography. The next chapter outlines the equipment, methods and procedures used to assess the appropriateness of fractal-based texture segmentation for mammography.

Chapter 4

Materials and Methods

4.1 Method Overview

Figure 4.1 shows an overview of the order of processing used in this thesis. First, standard film x-rays were digitized using the camera system in the Vision Laboratory of the School of Computing Science. Second, digital unwarping was performed on the digitized x-ray images to correct for spatial distortions that occurred in the analog-to-digital conversion process. Third, a series of synthetic images were generated as control data to aid in the evaluation of the fractal model for this particular application. These images were designed to emulate the behaviour of the gray-level intensities on the surface of film images with and without noise. Fourth, noise removal was performed on noisy images to limit the effects of image and sensor noise. Fifth, the images—with and without noise—were input into our implementations of the Intensity Statistics method to produce fractal images. Finally, the fractal images were used in combination with the original images—digitized x-rays and synthetic images—to produce subtractive fractal images. Four images—the original image, the fractal image, the correlation coefficient image and the subtractive fractal image—were used together in the evaluation of fractal-based texture segmentation of digital x-ray mammograms.

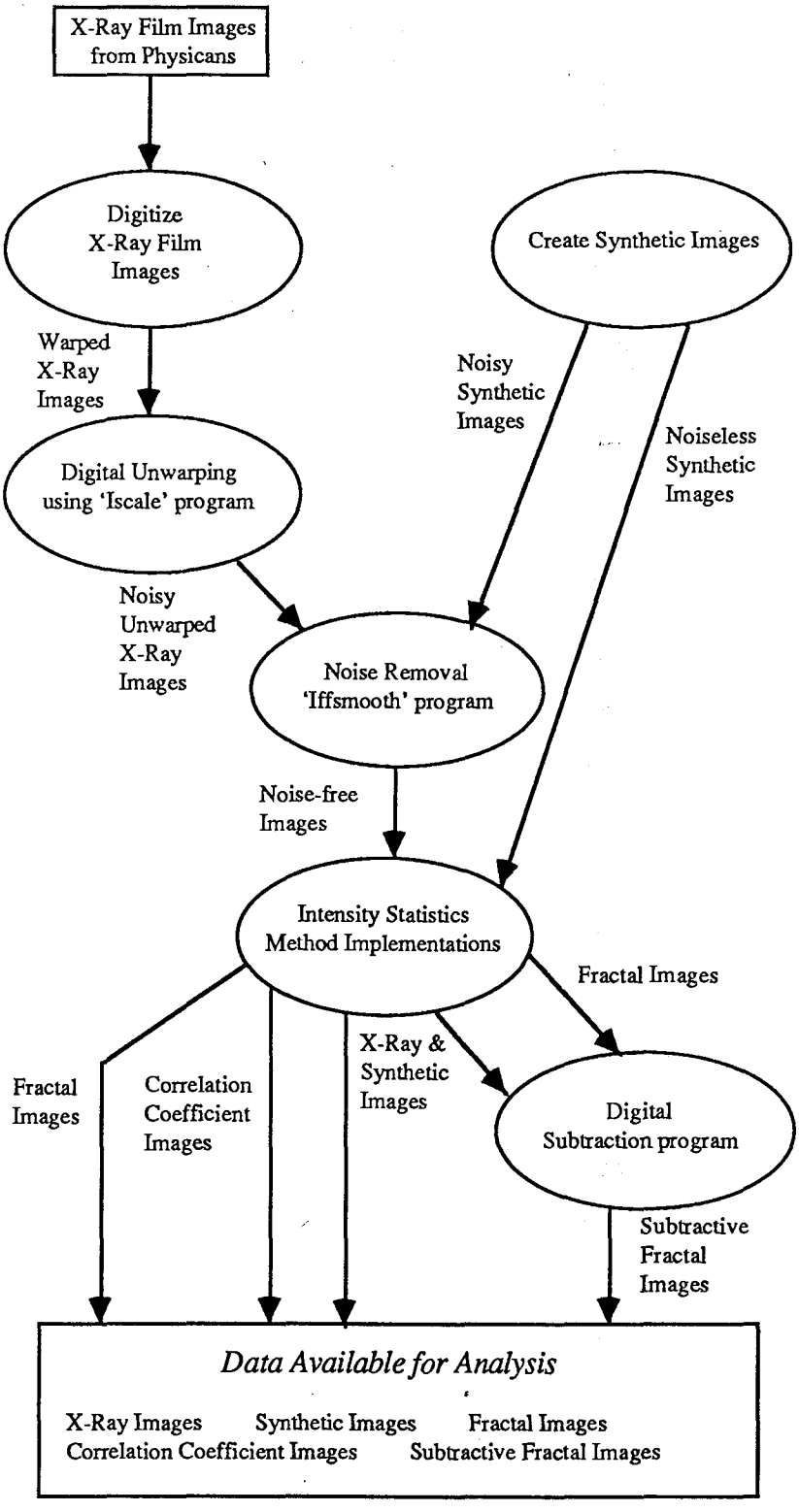

Figure 4.1: An overview of the order of processing

4.2 Hardware Components

Figure 2.1 illustrates the hardware components used in this thesis. The image acquisition system consists of a fluorescent film illuminator, a video camera, an analog-to-digital converter and a workstation.

The film illuminator utilizes an opaque diffusing surface placed over three fluorescent tubes to facilitate back illumination of the x-ray images. It operates at 118 volts, 60 Hz and up to 1.1 amps for a maximum output of 129.8 Watts.

The video camera is a VSP Labs model SC505. This solid state video camera uses charge coupled (CCD) frame transfer technology. It has 604 horizontal x 485 vertical active elements and conforms to the RS170/NTSC (National Television System Committee) standards. The camera was mounted with a Vivitar 72mm variable focal length closeup lens and an infrared filter.

Connected to the camera is the International Imaging Systems (IIS) Model 75F image processing system. The IIS provides the following functions: real-time display of images being photographed by the VSP video camera; digital capture of images from the camera for storage and processing on a workstation; display of images processed on other workstations; and performance of several complex image processing routines (e.g., convolution, edge detection, thresholding) in real-time on images via its own software utilities. For this thesis the IIS was used to convert the analog camera output into a digital image with 8-bit resolution for a possible 256 gray-scale intensities. Storage of the images was on a SUN4 workstation. Image processing and analysis of the images was performed on the same workstation running UNIX 4.1 using the C programming language. Display

of processed images was on both the IIS and on the SUN4. Display of the images on the IIS was performed using software from the Image File Format software library [IFFlib90]. Display of images on the SUN4 workstation was performed using a program called 'Color-Map Editor' developed by Ms. Kim Adamson-Sharpe. As well as facilitating the display of images on a SUN workstation, this program allows real-time user-controlled adjustment of image brightness and contrast. All photographs included in this thesis were taken from the SUN4 using the 'Color-Map Editor' program.

4.3 Image Acquisition

Dr. Donald McIntosh of the Primrose Ultrasound and Breast Clinic, Edmonton, Alberta, generously provided mammograms and accompanying clinical reports for ten patients. Mediolateral oblique and craniocaudal views—using breast compression—were provided for the left and right breasts in most cases. Several cases were accompanied by ultrasound films. The cases contained instances of benign breast disease, surgically and pathologically confirmed malignancy, and instances where no indication of breast disease could be found. Dr. McIntosh also included cases where mammography did not indicate any pathological process but where ultrasound confirmed the presence of breast disease. Markings indicated the films were taken using the Kodak Min-R rare earth screen. Unfortunately technical difficulties occured during the digitization process for several of the x-ray films which limited the final number of patients studied to eight. A synopsis of these eight patients' clinical reports is found in Appendix A.

Dr. Heather McNaughton of the Eagle Ridge Hospital, Department of Radiology and Dr. Douglas Read of Coquitlam, British Columbia, assisted by providing the chest x-rays and clinical reports for two patients. These films were obtained in order to compare

our results with those reported by [Dell87], [Vern87] and [ChDF89]. Since both x-ray films were very similar, a single patient was chosen to include in our experiments. A synopsis of this patient's clinical report is also found in Appendix A.

4.3.1 Digitization of X-Ray Films

The x-ray films were digitized by placing them against the lightbox—on maximum wattage—for back illumination. All excess light from the illuminator was masked out using heavy-duty black cardboard. The CCD camera was placed perpendicular to the illuminator at approximately 1.5 meters from the film surface and manually focused for each film image. All images were taken in the evening in a darkened room supplied with black-out drapes. A total of 17 mammograms and 2 chest x-rays were digitized.

The accurate digitization of the x-ray films was a important goal of this thesis. Unfortunately several problems were encountered which reduced the radiometric accuracy possible using this method of digitization. Initially, the CCD camera was found to be sensitive to the 60 cycle flicker of the fluorescent tubes in the film illuminator. This feedback caused distinct diagonal phase bars to appear in the digitized images. To reduce most of the radiation bars detected by the digitizer, the illuminator was coupled to two series linked phase protectors, and the CCD camera was linked to a single separate phase protector.

Next, examination of the video camera imagery produced by this particular CCD camera revealed several distortions within its optical system. [Evans87] determined that

some of these distortions with this camera are a result of fall-off,[8] vignetting[9] and non-uniform spatial sensitivity across the sensor chip. These distortions cause different regions within the camera's field of view to respond differently to the same input light intensity, producing a number of aberrations including spots and a darkening of the image towards the edges of the sensor chip.

Finally, we determined that a spatial distortion[10] occurs when the image is converted from NTSC standard format (i.e, 604 horizontal x 485 vertical elements) to digital format (i.e., 512 x 512 elements) causing degradation of image accuracy due to the loss and distortion of the original analog data.

4.3.2 Image Preprocessing

The inaccuracies and distortions introduced during the digitization of the film images necessitated the use of preprocessing techniques. We found the distortions within the camera's optical system were often imperceptible on the digitized back illuminated films, and therefore did not warrant correction. However, the spatial distortion which occurred during the A/D conversion process was significant and necessitated the use of software correction.

---

8 Fall-off is a variation in gray-level intensity associated with the distance an image point is from the center of the focal plane. Intensity is maximum at the center of the focal plane and decreases with the distance from the center.

9 Vignetting is the internal shadowing from the lens mount and aperature surfaces within the camera onto the image plane.

10 Spatial distortion refers to a change in the size, shape and position of objects in the digital image with respect to their true proportions and position.

a) Geometric Unwarping

Geometric unwarping of the digital images was performed using an available software program called 'Iscale' [IFFlib90]. Unwarping was performed using cubic convolution in a two-step process. First, the image was reduced vertically from 512 to 485 pixels (i.e., each pixel was reduced by approximately 0.947 percent). Second, the reduced image was expanded horizontally from 512 to 604 pixels (i.e., each pixel was expanded by approximately 1.179 percent). Table 4.1 shows our estimation of the amount of data lost due to conversion between NTSC and digital formats. This is a loss of image resolution of approximately 10.5 percent. After unwarping the digitized images more closely represented the physical proportions of the objects imaged on the original film data.

Array Size	*Total Number of Pixels*
Video camera: 604 x 485	292,940
Digitizer: 512 x 512	262,144
Number of pixels lost	30,796

Table 4.1: Number of pixels lost from conversion between NTSC and digital formats

b) Noise Removal and Contrast Enhancement

Despite the previously mentioned problems with the camera's optical system it was determined that the camera was sensitive enough to detect film-grain noise present in the film x-rays. To reduce the variation in image texture due to noise the digitized x-ray images were smoothed using the *Kth-Nearest Neighbour Method.*

The Kth-Nearest Neighbour method reduces the overall variation in image texture due to noise while simultaneously performing contrast and feature enhancement. It is based on the idea that pixels in the same region should have similar gray values. This is accomplished by taking the average using the *k* neighbours within a given neighbourhood region whose gray levels are closest to that of the given pixel. It does not require that neighbours involved in the averaging are adjacent. An integral part of this method is that the averaging scheme avoids crossing edges, but it makes no attempt to detect the presence of edges. This is accomplished by restricting the averaging to a subset of neighbourhood pixels chosen so that the most likely edge in a neighbourhood does not cross the subset. By keeping the mask size and the number of nearest neighbours relatively small, this method is able to reduce noise artifacts and enhance edges and contrast without loosing fine spatial detail.

Iteration #	*Mask Size*	*# of Nearest Neighbours*
1	5 x 5	3
2	5 x 5	3
3	3 x 3	3

Table 4.2: Parameters used in *Kth-Nearest Neighbour Smoothing* of digital images.

Smoothing was performed using an available software program called 'Iffsmooth' [IFFlib90]. This program was chosen because it allows specific control of mask sizes, number of nearest neighbours and numbers of iterations performed. The parameters used are shown in Table 4.2. A three-pass iterative approach in which the smoothed image from each iteration was the input to the next iteration is used. The parameters were chosen to

retain as much of the fine spatial detail of the x-rays as possible without averaging out details that could be possible lesion sights.

4.3.3 Generation of Synthetic Images

The limitations imposed upon the digitized x-ray images, a function of both the radiographic image formation process and the digital acquisition process, raised questions regarding the behaviour of the fractal model where these limitations were not a factor. This necessitated the generation of a series of synthetic images which were used to characterize the behaviour of the fractal model in certain situations found in the digitally acquired images. Specifically we wanted to:

- Determine how the fractal model behaves in various gray-level ranges;
- Determine the behaviour of the fractal model with and without the presence of noise;
- Determine whether noise affects the model uniformly across all gray-level ranges;
- Compare the results of our implementations of the intensity statistics method given identical conditions;
- Characterize the behaviour of the subtractive fractal image.

The behaviour of the synthetic images is extrapolated to the digitized x-ray images and used to explain the results of the fractal-based texture segmentation of digitized mammograms.

A SUN4 workstation was used to generate 8 test images—two groups of four images each—which were designed to imitate the behaviour of the gray-level intensities on

the surface of an x-ray film. These 8 images were used in the experiments to confirm that our implementations of the fractal model were working appropriately in ideal conditions.

4.4 Implementations

Two versions of the Intensity Statistics method—the *Center Surround* version and the *Patch* version—were developed and compared. The significant difference between the Center Surround and Patch versions arises from different interpretations of the phrase "centered on a pixel" found in [Pent84]. In the first interpretation—the Center Surround version, the fractal dimension is calculated specifically as it relates to the pixel on which the mask is centered. In the second interpretation—the Patch version, the center pixel has no particular importance other than as a position marker on the image; the fractal dimension is calculated for the area surrounding the center pixel, but it does not relate specifically to that pixel. Once calculated, both versions similarly assign the fractal dimension to the location corresponding to the center pixel of the mask. Finally, three images are generated. First, a *correlation coefficient image* is generated from the array of fractal values and its associated array of correlation coefficient values. This image is used to indicate what portion of the fractal image has a 'good' fit when the linear regression is performed. Second, a *fractal image* is generated from the array of fractal dimension values alone. Third, the fractal image is used together with the original image to produce a *subtractive fractal image.*

4.4.1 The Center Surround Version

In this version of the Intensity Statistics method, the center pixel of the mask is a fixed reference point for all calculations. The average gray-level mean and variance of all pixel pairs at all distances surrounding the center point of the mask are computed and used

pixel pairs at all distances surrounding the center point of the mask are computed and used to calculate the fractal dimension. Figure 4.2 shows a simple example using a 5 x 5 mask centered on pixel (3,3).

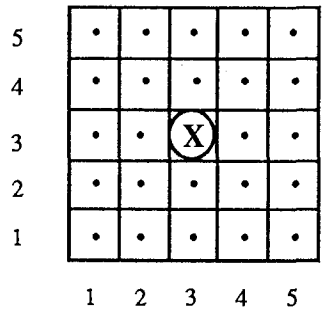

Figure 4.2: This is an example of the Center Surround version using a 5 x 5 mask. The circle indicates the center pixel of the mask. X indicates the position being used as a reference point for calculating the distances and absoluate values of the change of intensity. Note that the center pixel of the mask and X are the same, and that the reference point X does not move in the mask. The change in intensity and distance is calculated between X and each position marked by a •. Calculations are then made within the mask by using equation (3.7). As a result, the fractal dimension calculated according to this algorithm reflects a relationship specifically between the center pixel and its surrounding area.

Using the Euclidean distance formula, the distance Δz is calculated from the center pixel to each surrounding pixel location within the mask. The absolute value of the change of intensity between this pixel and each surrounding location is calculated and an average variance obtained for each possible Δz within the mask. The distance Δz's and their associated variances are then used in equation (3.7) and the number of points available for the linear regression are determined. The number of different Δz's obtained for various mask sizes are summarized in Table 4.3. The slope of the best-fit line from the regression, H, is then used to calculate the fractal dimension D using equation (3.4). D is then assigned to the location corresponding to the center pixel of the mask in the fractal image.

4.4.2 The Patch Version

In this version of the Intensity Statistics method the center pixel of the mask serves solely as a position marker for the mask on the image. As illustrated in Figure 4.3, the reference point for the average gray-level mean and variance calculations moves throughout the mask. Consequently, the fractal dimension is calculated for the area surrounding the center pixel but it does not relate specifically to the center pixel.

Initially, the reference pixel X starts at position (1,1) as shown figure 4.3 (a). As in the previous version, the Euclidean distance formula is used to calculate Δz from this pixel to the other locations within the mask. The absolute value of the change of intensity between this current X and the other locations within the mask are calculated. Once complete, location (1,2) becomes the next reference pixel as is shown in figure 4.3 (b). Again the calculations are performed between this new X and the other locations within the mask. Note that location (1,1) is excluded since the absolute value of the change of intensity between (1,1) and (1,2) was already included in the previous step. Figures 4.3 (c) to (f) show the movement of X through the remainder of the first row. This process continues until location (5,5) becomes X. Thus, the variance for distance Δz is evaluated on the average absolute value taken over *all* pixel pairs within the mask whose centers are Δz apart. Finally, an average variance is obtained for each possible Δz within the mask. The distance Δz's and their associated variances are then used in equation (3.7) and the number of points available for the linear regression are determined. The slope of the best-fit line from the regression is then used to calculate the fractal dimension D using equation (3.4). D is then assigned to the location corresponding to the center pixel of the mask in the fractal image.

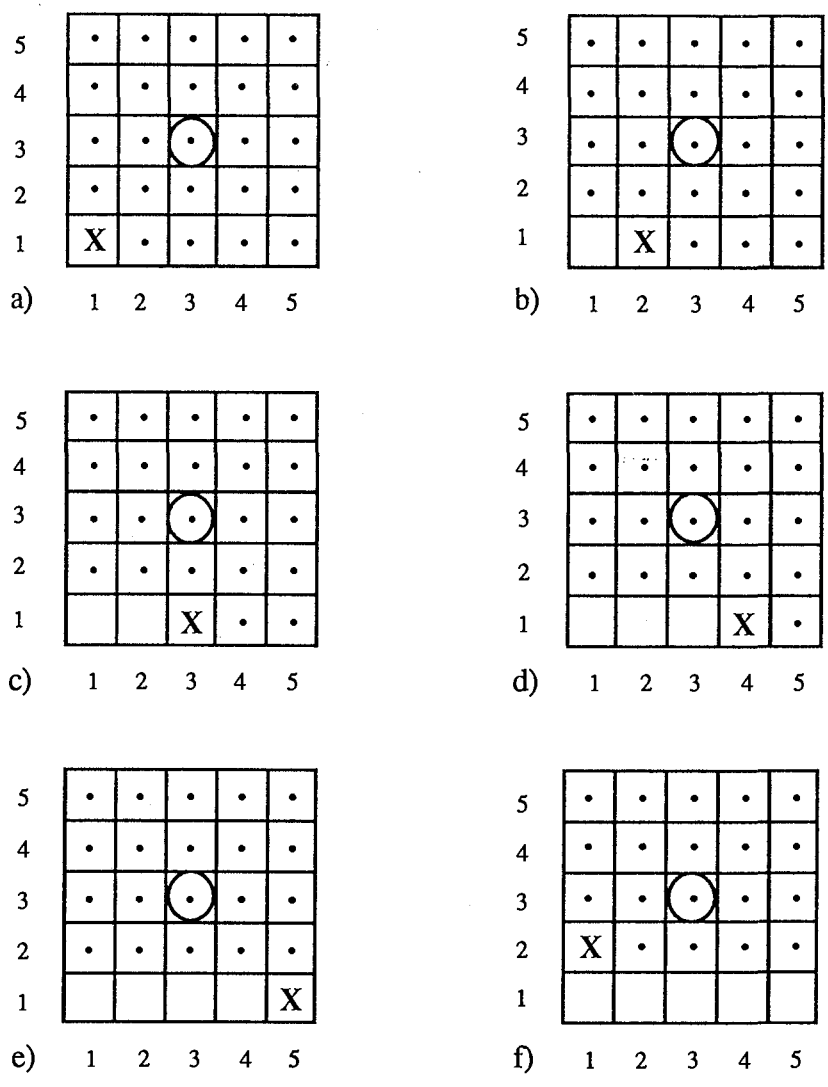

Figure 4.3: This is an example of the Patch Version using a 5 x 5 mask. The circle indicates the center pixel of the mask. X indicates the position being used as a reference point for calculating the distances and absoluate values of the change of intensity. Note that the center pixel of the mask and X are not the same, and that the reference point X moves throughout the mask. The change in intensity and distance is calculated between X and each position marked by a •. The diagram shows the first 6 positions for X and the other points used for the calculations. When the fractal dimension D is assigned to the center pixel, it reflects more a fractal dimension of the area surrounding the center pixel than just of that pixel.

Table 4.3 illustrates the computational strength and weakness of the Center Surround method. Due to the limited number of distances possible from the center pixel using a fixed reference point, equivalent mask sizes provide fewer points for the linear regression than the Patch method. Consequently, the Center Surround method is faster than the Patch method.

	Number of Regression Points	
Mask Size	*Center Surround Version*	*Patch Version*
3 x 3	2	5
5 x 5	5	14
7 x 7	9	26
9 x 9	14	41
11 x 11	19	56

Table 4.3: Depending on the mask size chosen, the Center Surround and Patch implementations generate different numbers of distances within a mask. Consequently the number of points that contribute to the averages and for the linear regression varies according to the particular implementation method.

4.4.3 Correlation Coefficient Image Generation

After fitting a regression line to our data for each *(x, y)* position in the image the *correlation coefficient* is used to evaluate how closely the points fit the regression line. The

correlation coefficient[11] R varies between -1 and +1. When R is positive the regression line has an upward slope; when R is negative the regression line has a downward slope. If R = +1 or R = -1 all the variation is explained and all points lie on the regression lie—a rare occurrence. If R = 0 the variables are not correlated.

To assess the 'goodness of fit' the fractal image was decomposed according to the R and D values. R was arbitrarily determined to be $|R| \geq .80$.[12] D was determined to fall into either of three possible categories: (1) $2.0 \leq D \leq 3.0$ as defined by fractal theory; (2) $D < 2.0$; (3) $D > 3.0$. From this decomposition a correlation coefficient image was generated and a black and white image created according to the particular D, R combination chosen. The statistics used in the derivation of the correlation coefficient image are evaluated for both the synthetic and 'real' images and compared between the implementation methods.

4.4.4 Fractal Image Generation

Generation of a fractal image is a simple mapping process. The computed fractal dimensions ranging between 2.0 to 3.0, are converted into corresponding gray-level values in the range of 0 to 255. For example, a fractal dimension of 2.0 or less appears as gray-level 0 or black, 2.5 appears as grey-level 127 or medium gray, and 3.0 or more as gray-level 255 or white. Consequently, the smoother the object and the lower its fractal dimension, the darker it will appear in the fractal image. The rougher the object and the higher its fractal dimension, the lighter it will appear in the fractal image.

---

11 It should be noted that R^2, the *Coefficient of Determination*, may also be used as another measure of the goodness of fit. R, the square root of the coefficient of determination, was chosen to remain consistent with the results reported by previous researchers.

12 In this thesis R is not being used to represent some result of particular correlation significance, but is just being taken as something representative of the goodness of fit for the regression line.

4.4.5 Subtractive Fractal Imaging

An important benefit of computer-based image analysis is the ability to correlate and combine different images using a quantitative process such as subtraction, for the purpose of extracting information not readily apparent on visual examination. Subtraction of images is used to enhance specific structures of interest while at the same time cancel out structures which interfere with the visual interpretation of the image. According to [Selz84], [Cao88] and [Loats88] the subtraction of digital images has been particularly successful in the field of cardiology, especially in the area of subtractive angiography.

Given this precedent, we combined data from the original image with that of the fractal image through as process we termed *subtractive fractal imaging*. Our goal was to determine whether the process of subtraction and the resulting subtractive fractal image could be used to: cancel structures, such as 'normal' background tissue, which often interfere with visual interpretation; verify tumour sites; as another means of image segmentation based on a combination of quantitative data types; and finally to extract information not readily apparent on visual examination of either the original x-ray image or the fractal image. Generation of a subtractive fractal image is not difficult. The gray-level values of the fractal image are subtracted from those of the original x-ray giving a subtractive fractal image. The next chapter discusses the results of our experiments.

Chapter 5

Results

The results in this chapter are presented as follows:

(i) The Patch and Center Surround methods are compared using synthetic images. The relationship between the fractal dimension D and and the correlation coefficient R is investigated to determine if the fractal models are providing reasonable results in terms of fit. The impact of various mask sizes and noise removal on D and R is evaluated. In particular, the conditions which generate D values that are out of bounds as defined by fractal theory (i.e., $D < 2.0$ or $D > 3.0$) are of special interest. These observations provide a basis from which comparisons can be made between real and synthetic images.

(ii) The Patch and Center Surround methods are compared using data from digitized x-rays. To evaluate the ability of the fractal model to detect large and small scale anatomical features, three patients with known tumours, cysts and microcalcifications are chosen for detailed discussion. As before, attention is focused on mask size, noise removal, the relationship between D and R, and the goodness of fit. The results are compared to those from the synthetic images. In addition, both methods are evaluated from a qualitative viewpoint. Finally, a rationale is given for preference of the Center Surround

implementation method for fractal-based texture segmentation of mammograms.

(iii) The potential for utilizing a subtractive fractal image in conjunction with the original image is analyzed.

(iv) The results obtained from applying the Center Surround method to all the digitized x-rays are discussed.

5.1 Comparison of Implementation Methods—Synthetic Images

To make this comparison, 8 synthetic images were analyzed using mask sizes for each method which generate the same number of data points for the linear regression. The 3 x 3 and 5 x 5 masks were chosen for the Patch method, and the 5 x 5 and 9 x 9 masks were chosen for the Center Surround method. Use of the same number of data points for both cases assists in attributing differences between the results to the method of implementation.

The synthetic images used for the comparison were:

(i) a flat plane corresponding to low valued pixels in the x-ray image (i.e., all pixels have the value 20);

(ii) a continuum of values corresponding to low- through mid-range values in the x-ray image (i.e., pixel values range from 50 to 149);

(iii) a continuum of values corresponding to mid-range through low values in the x-ray image (i.e., pixel values range from 149 to 50) which is the inverse of *(ii)*);

(iv) a continuum of values corresponding to mid- through high-range pixel values in the x-ray image (i.e., pixel values range from 150 to 249).

The first group of test images does not contain noise. The second group of images is identical to the first except that a randomly generated noise image corresponding to approximately 1.5 percent random white noise was added to each of the first images.

The following criteria was used to compare the D and R values generated by both methods:

(i) a D value is 'good' if $2.0 \leq D \leq 3.0$;

(ii) a D value is 'poor' if $D < 2.0$ or $D > 3.0$;

(iii) a R value is 'good' or has a'good fit' if $|R| \geq .80$;

(iv) a R value is 'poor' or has 'poor fit' if $|R| < .80$.

Note that criterion *(i)* and *(ii)* are defined by fractal theory,[13] whereas criteria *(iii)* and *(iv)* were arbitrarily chosen as reasonable limits.

5.1.1 Synthetic Images Without Noise—Observations and Discussion

Table 5.1 summarizes the goodness of fit results for synthetic images without noise. As expected, the fractal dimension for the flat plane was $D = 2.0$ and its goodness of fit or correlation value was $R = 1.0$. The observation that virtually no values $2.0 \leq D \leq 3.0$, are found in images *(ii)*, *(iii)* and *(iv)* was also anticipated since they are really a series of edges with no texture associated with them. In other words, the images are inclined planes of 45° slope, each successive pixel being one higher than the previous, without any

13 Voss, R.F., "Random fractal forgeries", *Fundamental Algorithms for Computer Graphics* (Editor R.A. Earnshaw), Springer-Verlag, Berlin Heidelberg, 1985, p 817

% of Total Image Where 2.0 ≤ D ≤ 3.0 and |R| ≥ .80				
	Patch Method		*Center Surround Method*	
Synthetic Image	*(3 x 3)*	*(5 x 5)*	*(5 x 5)*	*(9 x 9)*
i) Flat plane	100 %	100 %	100 %	100 %
ii) Low-mid plane	0	0	0	4
iii) Mid-low plane	0	0	0	4
iv) Mid-high plane	0	0	0	4

Table 5.1: Comparison of Patch and Center Surround methods on synthetic images ***without noise***. A D value is 'good' if $2.0 \leq D \leq 3.0$ and it has a 'good' fit if $|R| \geq .80$.

texture imposed on them. The small percentage (4 percent) noted for the Center Surround method,9 x 9 mask, is due to larger mask sizes being affected more by the physical borders of the image than the smaller mask sizes.

The observation that the fractal values for synthetic images *(ii)*, *(iii)* and *(iv)* were less than the topological dimension (i.e. $D < 2.0$), is consistent with the results reported in [Pent84]. Pentland explains that boundaries between homogeneous regions "do not fit well" into the fractal model. They seem to be the "most common event" giving rise to a non-fractal intensity surface and provide a method of detecting image points that are likely to be edges. Pentland states

> "When we observe a measured fractal dimension that is less than the topological dimension, therefore, we can reasonably expect that we have found a texture edge."[14]

Analysis of the D values generated from the Patch and Center Surround methods applied to the synthetic images *(ii)*, *(iii)* and *(iv)* suggests that certain conditions exist when

14 Pentland, A., "Fractal-based description of natural scenes," *IEEE Transactions on Pattern Analysis and Machine Intelligence*, **(PAMI-6:6)**, November 1984, p. 667

there are a consecutive number of edges. First, when the fractal value $D < 2.0$, then the $|R|$ value is usually greater than .80. Second, the direction of the step function does not appear to impact the D and R values (i.e., *(i)* and *(ii)* are inclined in opposite directions and give similar results). The combination of these observations with Pentland's comments suggest the conclusion that an edge has probably been detected when $D < 2.0$ and $|R| \geq .80$. These observations are used in later explanations of results on live data.

It should also be noted that fractal values greater than 3.0 were not generated. Such values were found to occur when noise was added to the synthetic images.

5.1.2 Synthetic Images With Noise—Observations and Discussion

Tables 5.2 and 5.3 summarize the goodness of fit results for synthetic images containing noise. The Patch (3 x 3) and Center Surround (5 x 5), and the Patch (5 x 5) and Center Surround (9 x 9) have been grouped together to facilitate comparisons between the methods. The table structure accounts for all points in the image and the D values are grouped according to R value. The column of values $D > 3.0$ are of particular concern since they indicate a fractal dimension greater than the topological dimension. These values are not only inappropriate from a theoretical basis but are also of no known value in the detection of abnormalities in the x-ray images.

It should also be noted that in Tables 5.2 and 5.3, images *(ii)* and *(iii)*, anomalies are evident which are due to a fault in the boundary extension algorithm [IFFlib90] and not to the fractal calculation methodology. All points that lie within the original image matrix are valid and give identical results.

Statistical Analysis of D and R									
Patch Method: (3 x 3)									
	For $2.0 \leq D \leq 3.0$			For $D < 2.0$			For $D > 3.0$		
Synthetic Image	% of Image	With good R	With poor R	% of Image	With good R	With poor R	% of Image	With good R	With poor R
i) Flat plane	60.52	7.76	52.76	26.26	20.54	5.72	13.22	0.00	13.22
ii) Low-mid plane	52.64	11.58	41.06	41.89	36.56	5.33	5.47	0.00	5.47
iii) Mid-low plane	53.82	11.58	42.24	41.29	36.06	5.23	4.89	0.00	4.89
iv) Mid-high plane	52.64	11.58	41.06	41.89	36.56	5.33	5.47	0.00	5.47
Center Surround Method: (5 x 5)									
i) Flat plane	44.44	10.23	34.21	4.79	4.09	0.70	50.77	8.88	41.89
ii) Low-mid plane	72.01	27.64	44.37	13.12	12.49	0.63	14.87	1.49	13.38
iii) Mid-low plane	72.24	27.39	44.85	13.02	12.39	0.63	14.74	1.45	13.29
iv) Mid-high plane	72.01	27.64	44.37	13.12	12.49	0.63	14.87	1.49	13.38

Table 5.2: Comparative analysis of D and R calculated by the Patch and Center Surround methods on synthetic images ***with noise*** using masks that generate 5 data points for the linear regression.

Statistical Analysis of D and R									
Patch Method: (5 x 5)									
	For $2.0 \leq D \leq 3.0$			For $D < 2.0$			For $D > 3.0$		
Synthetic Image	% of Image	With good R	With poor R	% of Image	With good R	With poor R	% of Image	With good R	With poor R
i) Flat plane	86.36	2.49	83.87	0.58	0.56	0.02	13.06	0.00	13.06
ii) Low-mid plane	77.01	64.21	12.80	22.99	22.98	0.01	0.00	0.00	0.00
iii) Mid-low plane	77.52	64.94	12.58	22.48	22.47	0.01	0.01	0.00	0.01
iv) Mid-high plane	77.01	64.21	12.80	22.99	22.98	0.01	0.00	0.00	0.00
Center Surround Method: (9 x 9)									
i) Flat plane	49.19	0.23	48.96	0.06	0.04	0.02	50.75	0.05	50.70
ii) Low-mid plane	90.41	49.15	41.26	9.53	9.29	0.24	0.06	0.00	0.06
iii) Mid-low plane	90.19	49.53	40.66	9.74	9.53	0.21	0.07	0.00	0.07
iv) Mid-high plane	90.41	49.15	41.26	9.53	9.29	0.24	0.06	0.00	0.06

Table 5.3: Comparative analysis of D and R calculated by the Patch and Center Surround methods on synthetic images ***with noise*** using masks that generate 14 data points for the linear regression.

Several observations about $D > 3.0$ values were made which indicate an objective of the analysis of images should be to minimize the generation of these values and the impact they may have on lesion sight detection. In particular, the following characteristics have been noted and can be deduced from the tables:

(i) The values $D > 3.0$ seem to be related to noise as these values were not found in the noise-free synthetic images. The importance of optimal noise removal techniques is implied.

(ii) The values $D > 3.0$ almost always tend to have a 'very poor' associated goodness of fit (i.e., tending towards zero). A significant improvement in the fractal-based texture segmentation and detection results may occur by removing the $D > 3.0$ values from the visual display. This result can be readily achieved by selecting D values that only have good R values (i.e., $|R| \geq .80$).

(iii) Small mask sizes tend to generate more $D > 3.0$ values than larger ones. A comparison of the percentage of the D values in Table 5.2 versus Table 5.3 supports this deduction. This implies that selection of the appropriate mask size is important in reducing the generation of these values.

It also appears that mask size affects generation of the number of 'good' D values (i.e., where $2.0 \leq D \leq 3.0$) which have 'good' R values (i.e., $|R| \geq .80$). These fractal values seem to be providing valuable texture information of a visual nature. A comparison between the tables also indicates that larger mask sizes provide better goodness of fit for the D values within this range. This was expected and was due to a smoothing effect of the larger mask sizes.

Interestingly, the number of $D < 2.0$ values with a good associated R (i.e., edge detection values) decreases as the mask size increases. This was expected as smaller mask sizes generate a larger number of 'false edges' which are a result of noise. Dellepiane et al [Dell87] mention that smaller masks allow the detection of a fractal edge (i.e., two different slopes), while larger masks tend to produce a single intermediate slope.

The smoothing effect of the large mask sizes does not facilitate the easy segregation of differently textured regions. Choosing the appropriate mask size becomes a balancing act between texture differentiation and edge detection capabilities. Obviously the detection of fractal edges cannot be sacrificed totally if you wish to find small anatomical features, particularly those indicating the earliest stages of cancer. This analysis suggests that an improvement in the detection capability of abnormalities in mammograms may be achieved if a mask size of 5 x 5 or 9 x 9 is used, and if all fractal dimensions $D \leq 3.0$ with a 'good' R are displayed. This approach combines the values $2.0 \leq D \leq 3.0$ which provides textural information and $D < 2.0$ which provides edge detection.

A comparison between the Patch and Center Surround methods indicates both approaches have limitations which should be recognized. The Patch method can produce disturbing results at small mask sizes. By definition a flat plane should not have any D values outside of the range of $2.0 \leq D \leq 3.0$, and particularly not in the range $D < 2.0$ (i.e., edge points). However, Table 5.2 indicates that in the presence of noise the Patch method (3 x 3) finds 26.26 percent of the total D values less than 2.0. In contrast, on the same image the Center Surround method (5 x 5) finds only 4.79 percent of the total D values less than 2.0. The Patch method seems more sensitive to noise and consequently erroneously allocates a greater proportion of the image as edge points than does the Center Surround method.

Conversely at the higher mask size the Center Surround method can produce fewer D values with a corresponding 'good' R value than the Patch method. Ultimately the final decision on which implementation method to choose is dependent on the method's performance in terms of accuracy and quality of the visual representation on the x-ray images of the patients.

5.1.3 Noise Removal Applied to Synthetic Images with Noise

To evaluate the impact of noise removal on the fractal model, Kth-Nearest Neighbour smoothing was applied using a three-pass iterative approach to the synthetic images containing noise. The smoothing parameters were identical to those applied to the digitized mammograms. The Center Surround method was then applied to the smoothed images. The objective of this experiment was twofold. First, to determine to what extent noise removal affects the calculated fractal dimensions and the correlation coefficient. Second, to determine whether it was possible to reproduce results similar to those obtained from the synthetic images before noise was added. Table 5.4 summarizes the goodness of fit results for the synthetic images before and after noise removal.

Table 5.4 demonstrates that a modest improvement—20 percent[15]—is made towards obtaining the same results (i.e., 100 percent for *(i)* and 4 percent for *(ii)*, *(iii)* and *(iv)* respectively) as those in the original noise-free synthetic image. Though this is not very encouraging, it does imply that using noise removal techniques does not negatively impact the process. The number of iterations could be increased to further improve the results. Unfortunately this would eliminate much of the fine detail which radiologists

15 Image *(i)* : (58.86 - 49.19) + 49.19 = 19.65 %
Images *(ii)*, *(iii)*, *(iv)* : (90.41 - 75.39) + 75.39 = 19.92 %

Synthetic Image	% of Image	With good R	With poor R	% of Image	With good R	With poor R	% of Image	With good R	With poor R
Statistical Analysis of D and R									
Center Surround (9 x 9) Without Noise									
	For $2.0 \leq D \leq 3.0$			For $D < 2.0$			For $D > 3.0$		
i) Flat plane	100.00	100.00	0.00	0.00	0.00	0.00	0.00	0.00	0.00
ii) Low-mid plane	4.00	4.00	0.00	96.00	96.00	0.00	0.00	0.00	0.00
iii) Mid-low plane	4.00	4.00	0.00	96.00	96.00	0.00	0.00	0.00	0.00
iv) Mid-high plane	4.00	4.00	0.00	96.00	96.00	0.00	0.00	0.00	0.00
Center Surround With Noise									
i) Flat plane	49.19	0.23	48.96	0.06	0.04	0.02	50.75	0.05	50.70
ii) Low-mid plane	90.41	49.15	41.26	9.53	9.29	0.24	0.06	0.00	0.06
iii) Mid-low plane	90.19	49.53	40.66	9.74	9.53	0.21	0.07	0.00	0.07
iv) Mid-high plane	90.41	49.15	41.26	9.53	9.29	0.24	0.06	0.00	0.06
Center Surround After Algorithmic Noise Removal									
i) Flat plane	58.86	1.75	57.11	0.40	0.28	0.12	40.74	0.08	40.66
ii) Low-mid plane	75.39	55.27	20.12	24.54	24.14	0.40	0.07	0.00	0.07
iii) Mid-low plane	74.49	54.83	19.66	25.45	25.16	0.29	0.06	0.00	0.06
iv) Mid-high plane	75.39	55.27	20.12	24.54	24.14	0.40	0.07	0.00	0.07

Table 5.4: Comparative analysis of D and R calculated by the Center Surround method on synthetic images ***with noise*** using a 9 x 9 mask before and after Kth-Nearest Neighbour smoothing.

examine when diagnosing cancer. Figures 5.1 (a) and (b) illustrate the typical results obtained by applying the Kth-Nearest Neighbour smoothing to digitized x-ray images. In general it seems apparent that noise removal is much more of an 'art' than a 'science' as one must carefully balance the number of iterations and window sizes in order to bring out both the fine and coarse details of the x-ray image. Clearly there is a great deal of room for improvement in the area of noise removal. Any significant developments in noise removal may produce dramatic improvements in fractal-based detection techniques which can be used for identifying abnormalities in x-ray mammograms.

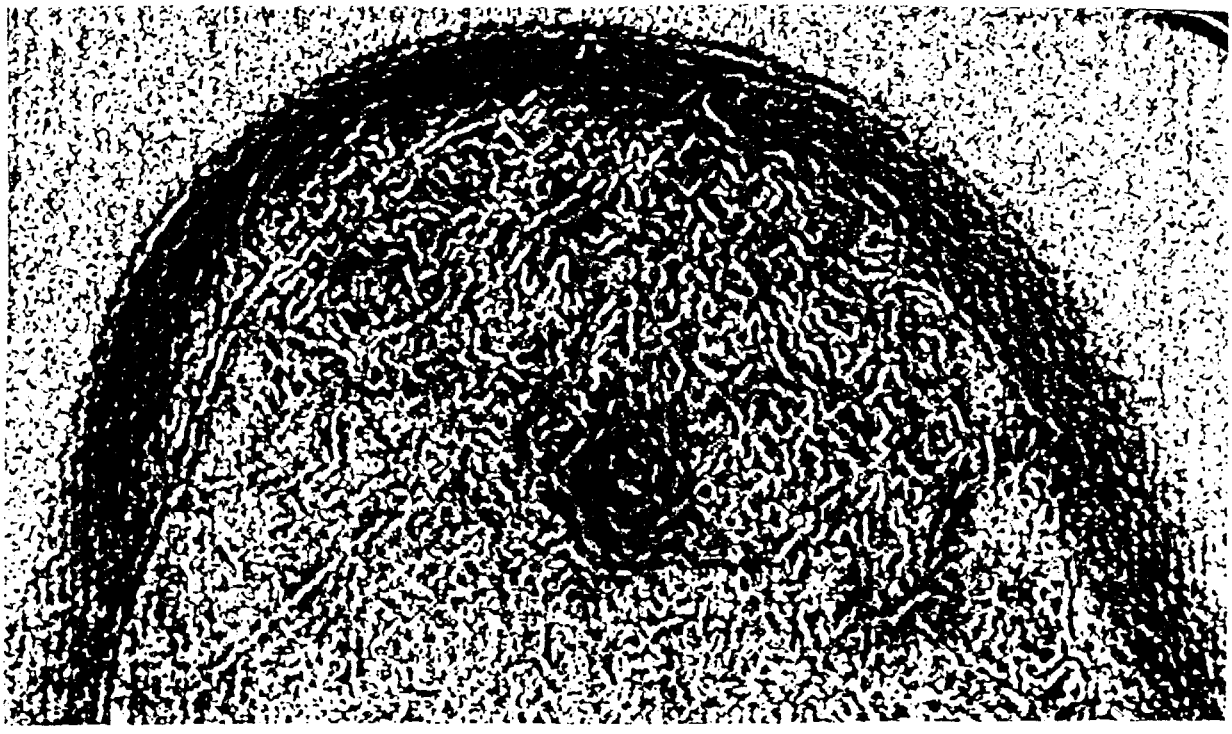

Figure 5.1: (a) Fractal image generated from 'raw' data without any algorithmic noise removal. Note the generally fuzzy appearance of the image. The sensitivity to noise is evident in the amount of white—indicating fractal values D > 3.0—throughout the image.

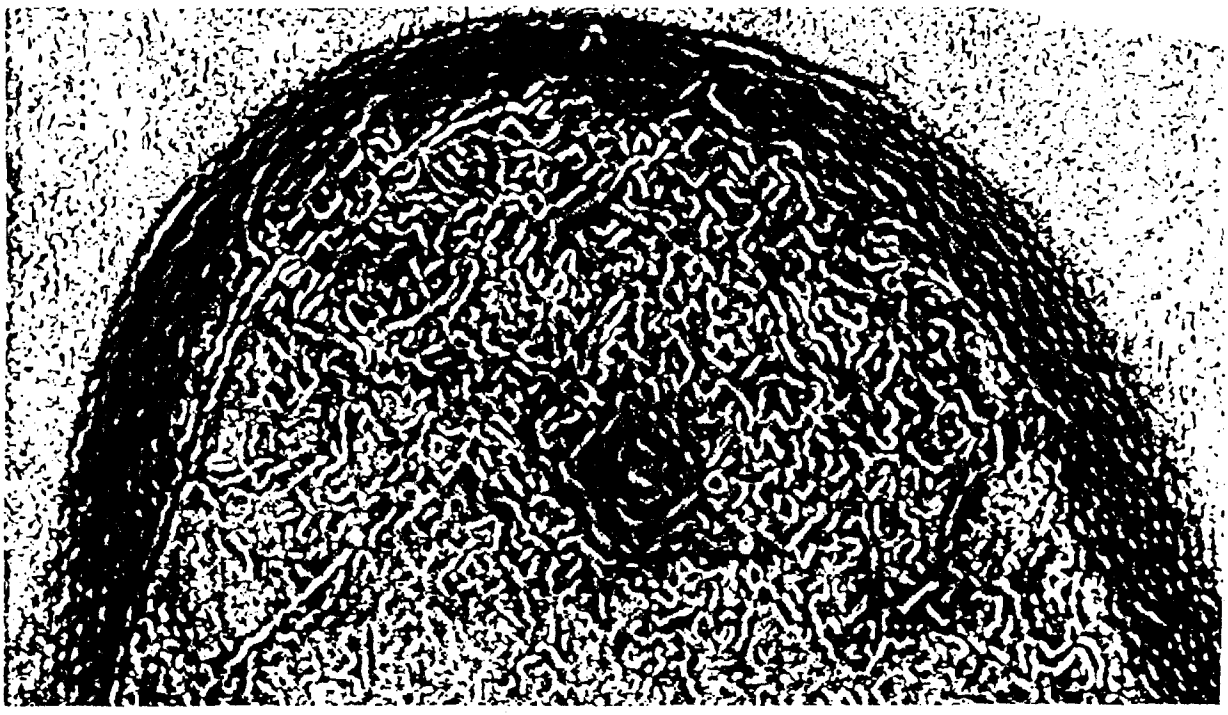

Figure 5.1: (b) Fractal image generated after Kth-Nearest Neighbour smoothing. The amount of white throughout the image has decreased and the image has become less fuzzy and more defined.

5.2 Comparison of Implementation Methods—X-Ray Images

Tables 5.5, 5.6 and 5.7 summarize the goodness of fit results for 'real' images containing known tumours, cysts and microcalcifications. These images—Figures 5.2, 5.3 and 5.4 respectively—are taken from patients 8, 2 and 1 of Appendix A. To facilitate visual analysis the figures consist of the original image, the fractal image and the correlation coefficient image.[16] Since the analysis applied to the x-ray images is similar to that used on the synthetic images, the tables have an identical format. All major observations for the synthetic images were verified for the 'real' images and are used to assist in analyzing the results obtained from the live data.

As previously indicated, a central objective is to minimize the generation of fractal values where $D > 3.0$ which seem to be a result of noise. This has been achieved two ways. First, Kth-Nearest Neighbour smoothing is applied to all x-ray images prior to fractal analysis. Figures 5.1 (a) and (b) illustrate the improvement in visual quality of the fractal image after smoothing. Second, larger mask sizes (i.e., 5 x 5 and 9 x 9) are used. As well as being less sensitive to noise, the larger sizes provide an additional advantage of improved R values without elimination of their edge detection ability. The following analysis focuses on how well the Patch (5 x 5) and Center Surround (9 x 9) methods detect the abnormalities in the mammograms of the selected patients.

16 As noted by the observations in sections 5.1.1, 5.1.2 and 5.1.3, improved edge detection and texture segmentation may occur when the fractal dimension are in the ranges $D \leq 3.0$ where the correlation coefficient is $|R| \geq .80$. The correlation coefficient image displays all pixels meeting this criterion as black and all others as white.

5.2.1 Analysis of Patch and Center Surround Methods—Tumour

Table 5.5 summarizes the results for the image containing a large tumour. At the larger mask size less than four percent of the image has a fractal dimension $D > 3.0$ which, is acceptable. Virtually all of the edge detection fractal values (i.e., $D < 2.0$) have good R values, which can be used to detect the tumour. The Center Surround method out performs the Patch method by providing approximately 48 percent[17] more values in the range $2.0 \leq D \leq 3.0$ which are used to detect changes in texture.

Statistical Analysis of D and R—Tumour

	For $2.0 \leq D \leq 3.0$			For $D < 2.0$			For $D > 3.0$		
Method/Mask Size	% of Image	With good R	With poor R	% of Image	With good R	With poor R	% of Image	With good R	With poor R
Patch: (3 x 3)	37.43	12.82	24.61	56.39	52.67	3.72	6.18	0.01	6.17
(5 x 5)	63.93	26.81	37.12	32.21	31.87	0.34	3.86	0.00	3.86
Center Surround:									
(5 x 5)	57.84	37.02	20.82	36.44	35.42	1.02	5.72	0.69	5.03
(9 x 9)	70.15	39.75	30.40	27.31	26.11	1.20	2.54	0.02	2.52

Table 5.5: Comparative analysis of D and R calculated by the Patch and Center Surround methods on an image containing a large tumour.

Visually Figures 5.2 (a) and (b) provide dramatic evidence of texture change and tumour shape. Generally the fractal image mirrors the tumour's circular pattern, while the distance between the texture lines within the tumour itself seem farther apart than those of the surrounding area. Interestingly the fractal image seems to indicate an appendage—perhaps growth—into the surrounding tissue at the lower right corner of the tumour which is not very obvious in the x-ray image. Finally, as indicated from the gray-level the fractal

[17] Center Surround (9 x 9) versus Patch (5 x 5): (39.75 - 26.81) ÷ 26.81 = 48.26 percent

(a)

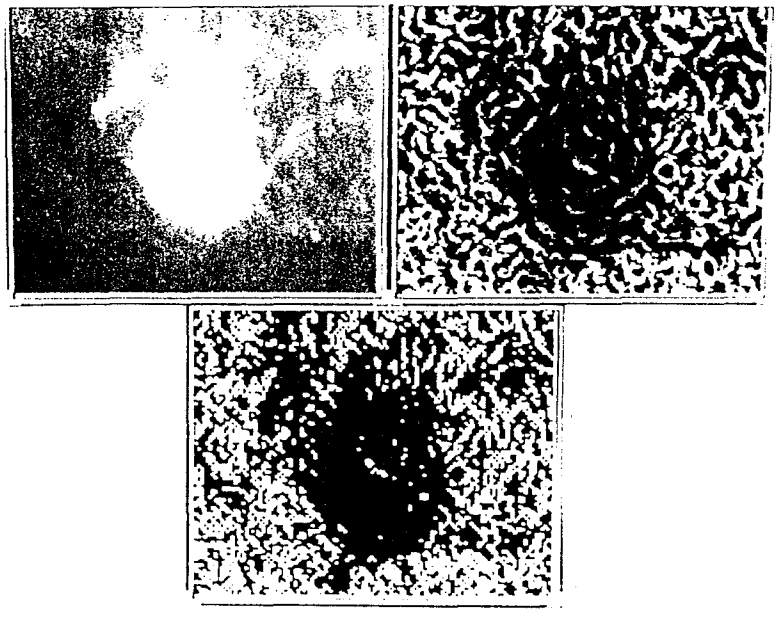

(b)

(c)

Figure 5.2: (a) Original digitized x-ray image showing large tumour from patient 8.
(b) Fractal image generated by Center Surround method using a 9 x 9 mask.
(c) Correlation coefficient image generated from image b). Dark areas are fractal values in the range $D \leq 3.0$ where $|R| \geq .80$.

(d)

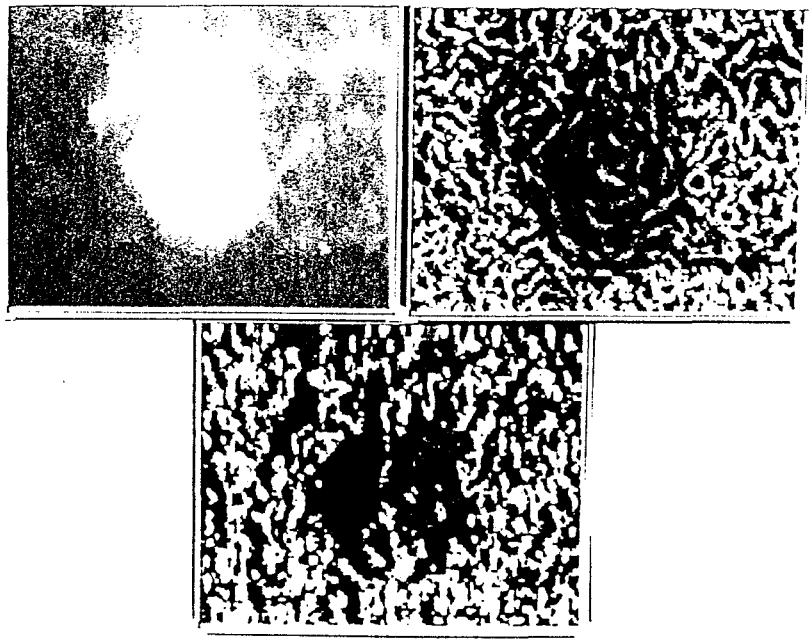

(e)

(f)

Figure 5.2: (d) Original digitized x-ray image showing large tumour from patient 8.
(e) Fractal image generated by Center Surround method using a 9 x 9 mask.
(f) Fractal image generated by Patch method using a 5 x 5 mask.

dimension is significantly less than that of the surrounding area.

The display of all fractal values with a 'good' R indicates that there is a very good fit for all D values in the tumour region. The correlation coefficient image Figure 5.2 (c) provides vivid confirmation of the tumour's shape and edges, and suggest that displaying values $D \leq 3.0$ with a good R may be useful in assisting the edge detection/segmentation capabilities of the fractal method.

A comparison of Figures 5.2 (e) and (f) indicates that the Center Surround method is not only quantitatively but also qualitatively superior. In particular, the Patch method does not define the boundaries of the tumour as sharply. However, one must temper the successful results for this image with the knowledge that this patient's abnormality was readily detectable on the original mammogram. To be genuinely useful this technique needs to be able to detect less obvious abnormalities such as small cysts and microcalcifications.

5.2.2 Analysis of Patch and Center Surround Methods—Cysts

Table 5.6 summarizes the results for the image containing cysts. Again at the larger mask sizes less than four percent of the image has a fractal dimension of $D > 3.0$, and the edge detection fractal values (i.e., $D < 2.0$) have mainly good R values. As before the Center Surround method out performs the Patch method—approximately 57 percent[18] more values in the range $2.0 \leq D \leq 3.0$ which are used to detect changes in texture.

18 Center Surround (9 x 9) versus Patch (5 x 5): (44.77 - 28.53) ÷ 28.53 = 56.92 percent

Statistical Analysis of D and R—Cysts

	For $2.0 \leq D \leq 3.0$			For $D < 2.0$			For $D > 3.0$		
Method/Mask Size	% of Image	With good R	With poor R	% of Image	With good R	With poor R	% of Image	With good R	With poor R
Patch: (3 x 3)	37.20	12.48	24.72	54.93	50.98	3.95	7.87	0.03	7.84
(5 x 5)	62.90	28.53	34.37	33.53	33.17	0.36	3.57	0.00	3.57
Center Surround:									
(5 x 5)	57.26	38.93	18.33	38.37	37.56	0.81	4.37	0.39	3.99
(9 x 9)	67.96	44.77	23.19	30.53	29.64	0.89	1.51	0.00	1.51

Table 5.6: Comparative analysis of D and R calculated by the Patch and Center Surround methods on an image containing cysts.

Visually Figures 5.3 (a) and (b) provide evidence of texture change and cyst shape. The cysts have a circular pattern which is fairly evident on the fractal image, although they are quite a bit smaller and therefore less dramatic than the tumour. It should be noted that the patient's report indicated the cysts were difficult to see on the mammogram. Again the gray-level indicates the fractal dimension is less in the area of the cysts than that of surrounding areas.

The correlation coefficient image Figure 5.3 (c) indicates that there is a good fit for D values in the cysts region and provides a particularly dramatic outline of the cysts especially when viewed in conjunction with the fractal image. A comparison of Figures 5.3 (e) and (f) once again show that the Center Surround method provides a superior visual display. Generally the fractal method is still having some success in identifying the cysts, although it becomes more difficult to detect the characteristic circular patterns in the fractal image. As a result the correlation coefficient image becomes more useful in confirming this particular analysis.

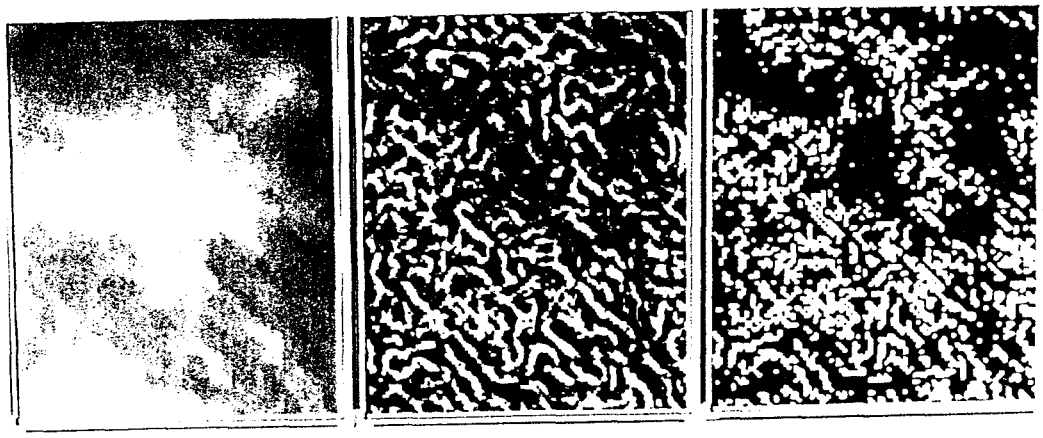

(a) (b) (c)

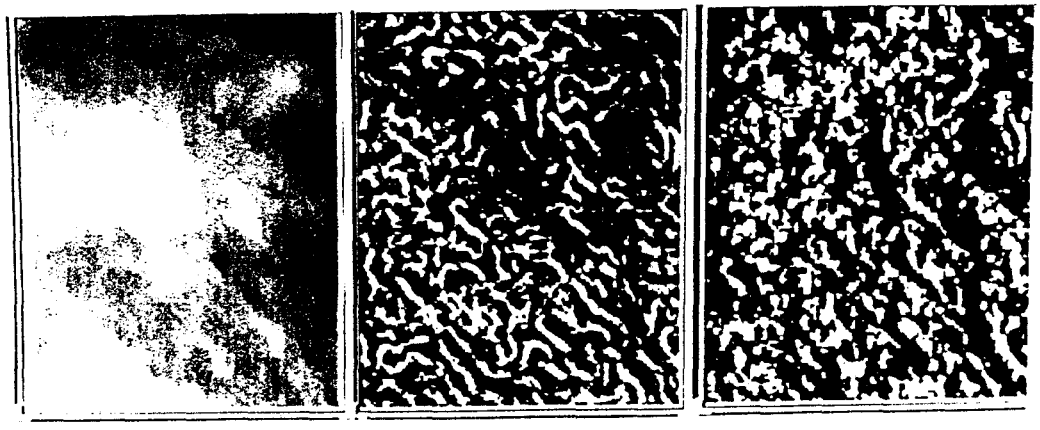

(d) (e) (f)

Figure 5.3: (a) Original digitized x-ray image showing cysts from patient 2.
(b) Fractal image generated by Center Surround method using a 9 x 9 mask.
(c) Correlation coefficient image generated from image (b). Dark areas are fractal values in the range $D \leq 3.0$ where $|R| \geq .80$.
(d) Original digitized x-ray image showing cysts from patient 2.
(e) Fractal image generated by Center Surround method using a 9 x 9 mask.
(f) Fractal image generated by Patch method using a 5 x 5 mask.

5.2.3 Analysis of Patch and Center Surround Methods—Microcalcifications

Table 5.7 summarizes the results for the image containing the microcalcifications. It indicates that two percent or less of the image contains fractal values $D > 3.0$, which are some of the best results achieved. As in the previous x-ray images virtually all of the edge detection fractal values have a 'good' R. Once again the Center Surround method out performs the Patch method—approximately 62 percent[19] more values in the range $2.0 \leq D \leq 3.0$ which are used to detect changes in texture.

Statistical Analysis of D and R—Microcalcifications

	For $2.0 \leq D \leq 3.0$			For $D < 2.0$			For $D > 3.0$		
Method/Mask Size	% of Image	With good R	With poor R	% of Image	With good R	With poor R	% of Image	With good R	With poor R
Patch: (3 x 3)	30.21	13.10	17.11	64.98	62.25	2.73	4.81	0.01	4.80
(5 x 5)	49.80	27.95	21.85	48.05	47.85	0.20	2.15	0.00	2.15
Center Surround:									
(5 x 5)	51.75	41.94	9.81	46.61	45.85	0.76	1.64	0.12	1.52
(9 x 9)	58.74	45.43	13.30	40.54	39.75	0.79	0.72	0.00	0.72

Table 5.7: Comparative analysis of D and R calculated by the Patch and Center Surround methods on an image containing microcalcifications.

Visually, Figures 5.4 (a) and (b) provide minimal evidence of texture change and microcalcification shape. The microcalcifications appear as partial circles, but these are very small and difficult to detect. The patient's report also noted that the microcalcifications were difficult to see and as a result were marked on the mammogram by the consulting physician. The display of the fractal values with a 'good' R in Figure 5.4 (c) is also incon-

19 Center Surround (9 x 9) versus Patch (5 x 5): (45.43 - 27.95) ÷ 27.95 = 62.54 percent

(a)

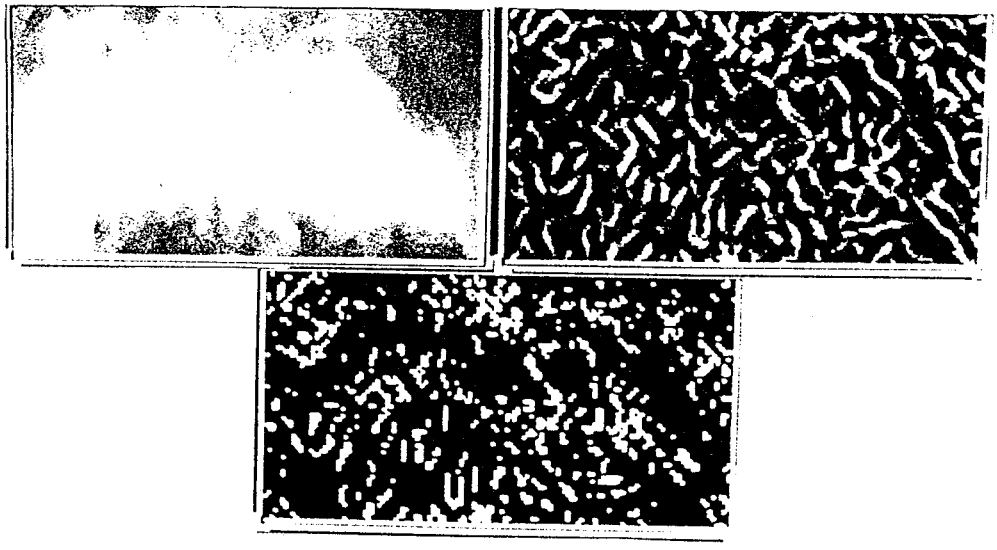

(b)

(c)

Figure 5.4: (a) Original digitized x-ray image showing microcalcifications from patient 1.
(b) Fractal image generated by Center Surround method using a 9 x 9 mask.
(c) Correlation coefficient image generated from image b). Dark areas are fractal values in the range $D \leq 3.0$ where $|R| \geq .80$.

(d)

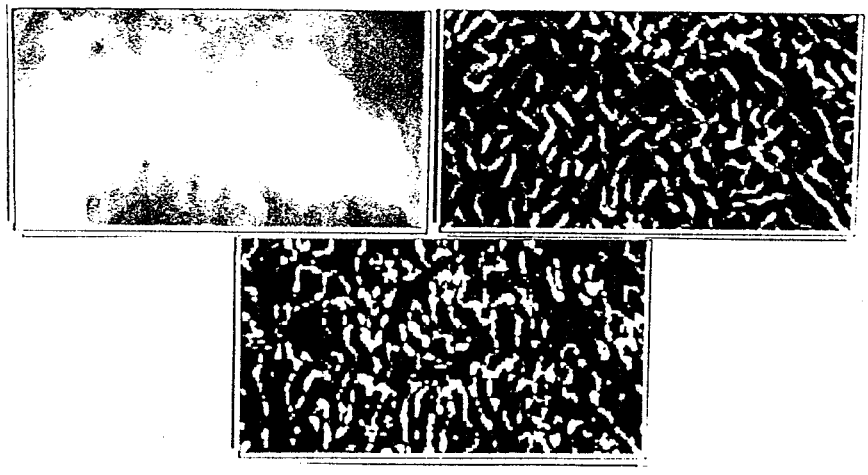

(e)

(f)

Figure 5.4 (d) Original digitized x-ray image showing microcalcifications from patient 1.
(e) Fractal image generated by Center Surround method using a 9 x 9 mask.
(f) Fractal image generated by Patch method using a 5 x 5 mask.

clusive and vague. The evidence may exist but it appears to be quite subtle and not easy for the human eye to detect. A comparison of Figures 5.4 (e) and (f) also indicates that both the Patch and Center Surround methods provide inconclusive results. Further refinements to the fractal method may be needed before conclusive results can be reported in regards to the method's ability to detect such minute abnormalities as microcalcifications.

5.2.4 Rationale for Preference of Center Surround Method

Quantitative and qualitative evidence has been presented throughout this chapter that illustrates differences between the Patch and Center Surround methodologies. In particular:

(i) Synthetic images whose D values were calculated using the Patch method using small mask sizes produced unusual results (i.e., false edges) and were more unstable than the Center Surround method.

(ii) The Center Surround method at comparable mask sizes consistently produces more values in the range $2.0 \leq D \leq 3.0$ with good R values on real data than the Patch method.

(iii) The Center Surround method consistently produces visually superior fractal and correlation coefficient images than the Patch method.

(iv) The Center Surround method is computationally faster than the Patch method due to the fewer number of calculations performed within each mask.

On the basis of these findings, the Center Surround method, 9 x 9 mask, was used to generate the fractal images for all of the patients. These images are shown together with the

original digitized x-ray films in the Appendix. A fractal image of a chest x-ray was also generated using the Center Surround method. It was compared to the image reported in [ChDF89] and used to confirm the 'correctness' of our generated images.

5.3 Utilization of Subtractive Fractal Imaging

As mentioned in the previous chapter, the goal of subtractive fractal imaging was to determine whether data from the original x-ray and the fractal image could be combined through the process of subtraction in order to extract information not readily apparent on the visual examination of either image. Figures 5.5 (a), (b) and (c) illustrate the results obtained by subtracting the fractal image from the original digital x-ray using the tumour, cyst and microcalcification images previously discussed.

Unfortunately, little evidence was obtained indicating that the ability to detect abnormalities was improved. In general, the subtractive images did not segment the image as well as the fractal image and were felt not to be appropriate for this application.

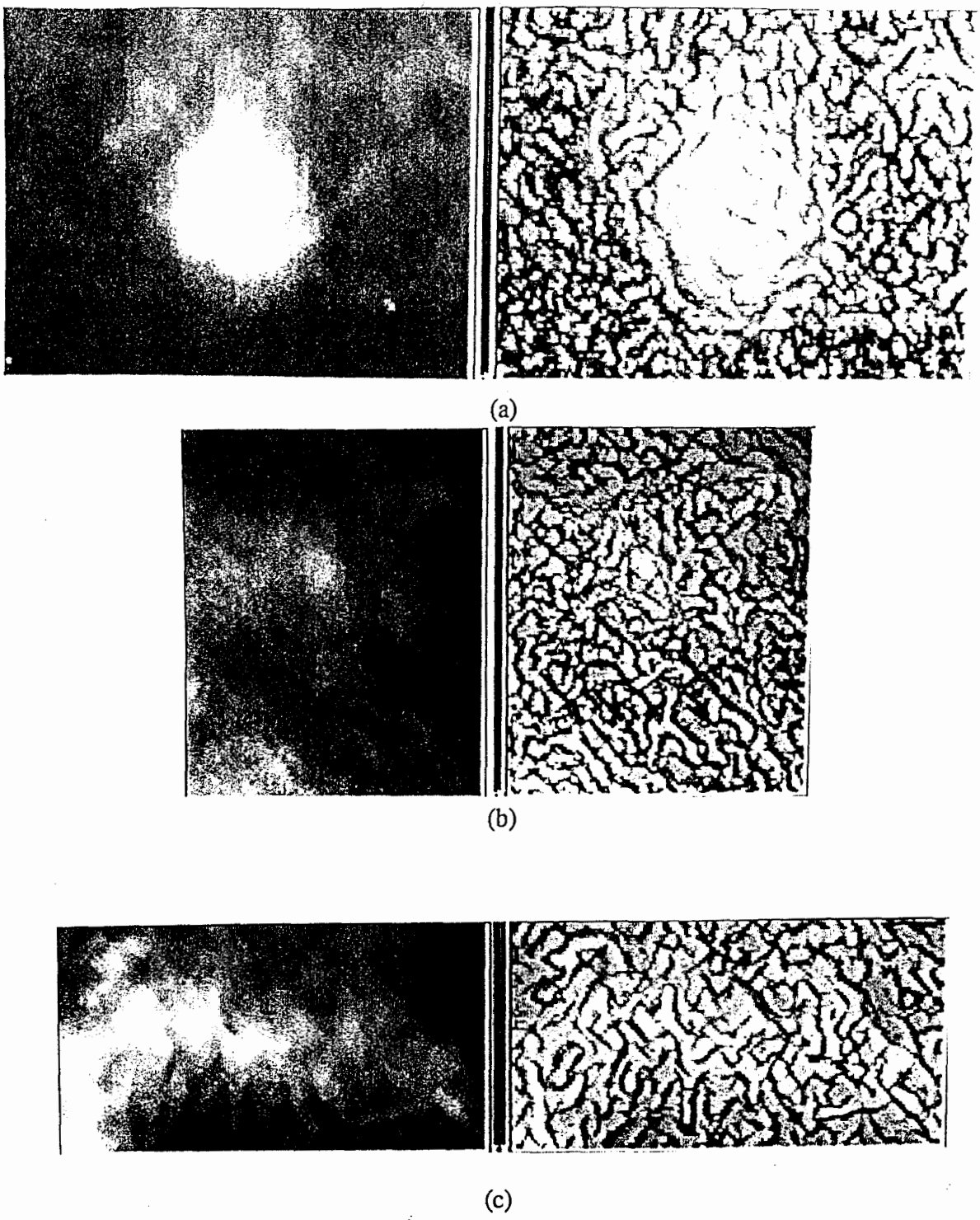

Figure 5.5: (a) X-ray image showing large tumour and subtractive fractal image.
(b) X-ray image showing cysts and subtractive fractal image.
(c) X-ray image showing microcalcifications and subtractive fractal image.

5.4 Summary of Results for all Digitized X-Ray Images

As in the previous tables, the fractal images for all the patients are analyzed in terms of edge detection fractal values (i.e., $D < 2.0$ and $|R| \geq .80$) and fractal values which provide textural information (i.e., $2.0 \leq D \leq 3.0$ and $|R| \geq .80$). These measures are used in combination to indicate abnormalities in the x-ray images. Table 5.8 summarizes the statistical results for all patients using the Center Surround method with a 9 x 9 mask. There is a significant increase in $D > 3.0$ values from those reported in the earlier analysis of the three test patients. For patient 1 (microcalcifications) the $D > 3.0$ values increased from .72 to 15.70 percent, patient 2 (cysts) the $D > 3.0$ values increased from 1.51 to 13.15 percent, and patient 8 (tumour) the $D > 3.0$ values increased from 2.54 to 9.34 percent. It should be noted the fractal images of Table 5.8 contain the entire mammogram including a significant amount of background from the back plate, whereas the images in Tables 5.5, 5.6, 5.7 contain only selected areas with known abnormalities and no back plate. It seems clear that the increase in $D > 3.0$ values is a function of the amount of background in the image. A decrease in these values can be achieved by cropping the digitized image.

The decrease in $2.0 \leq D \leq 3.0$ and $D < 2.0$ values with a good R can also be attributed to the amount of background in the image. The relative stability of the D values between the cropped and full images of patient 8 (tumour), 39.75 versus 32.61 percent, and 26.11 versus 26.38 percent, is due to the fact that these images have less total background area than patients 1 and 2. This supports the approach of removing as much background from the image as possible to improve the D value statistics.

Statistical Analysis of D and R by Patient

Patient/Breast/Image	For 2.0 ≤ D ≤ 3.0			For D < 2.0			For D > 3.0		
	% of Image	With good R	With poor R	% of Image	With good R	With poor R	% of Image	With good R	With poor R
A.1.1 Left view*	62.81	26.30	36.51	21.49	20.69	.80	15.70	.04	15.66
A.2.1 Left view**	58.23	29.38	28.85	28.62	27.71	.91	13.15	.05	13.10
A.2.2 Left side view	59.43	31.79	27.64	29.11	28.46	.65	11.46	.04	11.42
A.3.1 Left view	62.93	30.83	32.11	24.95	23.92	1.03	12.12	.05	12.07
A.3.2 Left side view	59.16	34.30	24.86	31.02	29.85	1.17	9.82	.03	9.79
A.3.3 Right view	60.29	31.80	28.49	27.79	26.56	1.23	11.92	.05	11.87
A.3.4 Right side view	60.15	35.30	24.85	30.46	29.45	1.01	9.39	.03	9.36
A.4.1 Left view	58.94	28.36	30.58	23.75	23.20	.55	17.31	.07	17.24
A.4.2 Left side view	59.24	29.12	30.12	25.60	24.90	.70	15.16	.05	15.11
A.4.3 Right view	57.83	26.08	31.75	23.18	22.43	.75	18.99	.08	18.91
A.4.4 Right side view	59.00	34.60	24.40	31.09	30.19	.90	9.91	.03	9.82
A.5.1 Left view	61.50	29.39	32.11	25.07	24.35	.72	13.43	.03	13.40
A.6.1 Left view	61.19	27.88	33.31	22.73	22.12	.61	16.08	.06	16.02
A.6.2 Right view	60.52	28.61	31.91	24.78	24.02	.76	14.70	.07	14.63
A.7.1 Left view	58.59	28.31	30.28	24.91	24.49	.41	16.50	.06	16.44
A.7.2 Right view	58.05	27.48	30.57	26.05	25.61	.43	15.90	.04	15.86
A.8.1 Left view	63.47	32.71	30.76	27.51	26.26	1.25	9.02	.04	8.98
A.8.2 Left side view	59.26	37.92	21.34	35.43	34.09	1.34	5.31	.02	5.29
A.8.3 Right view***	63.08	32.61	30.47	27.58	26.38	1.20	9.34	.03	9.31
A.8.4 Right side view	62.43	37.01	25.42	31.54	30.33	1.21	6.03	.02	6.01
A.9.1 Chest front view	62.02	33.57	28.45	31.01	29.99	1.02	6.97	.03	6.94

Table 5.8: Comparative analysis of D and R calculated by the Center Surround method, 9 x 9 mask, on x-ray images of all patients included in the Appendix. Patient and image numbers correspond to those found in the Appendix. *contains microcalcifications, **contains cysts, ***contains large tumour.

Correlation coefficient images (i.e., $D \leq 3.0$ where $|R| \geq .80$) of the entire mammogram are also included in the Appendix for the three test patients. Though the correlation coefficient images of the complete breast successfully indicate areas where abnormalities are known to exist, they also tend to indicate falsely other areas as having abnormalities when they are not perceived on the mammogram. Of particular concern are the edges of the breast and the nipple regions. While from a diagnostic point of view it would be difficult to use these images without further research, these findings then seem to be of a false-positive rather than a false-negative nature.

In general, the results for the fractal images are quite consistent. A review of the fractal images in the Appendix shows several interesting characteristics. First, anatomical features such as blood vessels and bone are clearly delineated. Second, in 'normal' tissue the texture lines differ from those within an abnormality. Darker, circular patterns (i.e., low fractal dimension) seem to be in the vicinity of an abnormality and the texture lines seem to move toward the object. Normal tissue is characterized by higher fractal dimension (i.e., lighter colour) and the texture lines do not seem to move in a specific direction. Finally, film grain noise is evident in the back plate areas of the fractal image in the form of very high fractal values (i.e., white and almost white areas).

Chapter 6

Conclusions

6.1 Conclusions

In summary, the fractal model performed satisfactorily for some images but was difficult to interpret for the remainder. On the positive side, for relatively large abnormalities such as tumours and cysts, the fractal model provided assistance in detecting problem areas. Generally these abnormalities were depicted in the fractal image as circular patterns with texture lines which were further apart than those of the surrounding area. The fractal dimensions of these areas were usually less than (i.e., darker) the surrounding area.

Unfortunately, as the abnormalities decreased in size the ability of the fractal method to provide clear evidence of texture change and object shape also decreased. Small cysts and microcalcifications were translated into relatively small changes in a 'busy' fractal image. The evidence may have existed but it became very subtle and difficult to interpret or easily detect.

It appears that in some cases radiologists may actually have an advantage if they only use the original x-ray image. The digitization process introduces noise into what may not be a very good image in the first place. The modest improvement of 20 percent for the fractal method provided by the Kth-Nearest Neighbour smoothing indicates that noise

removal does not negatively impact the process. Probably the greatest opportunity for improving the fractal method lies in this area.

Clearly the method of implementing the fractal model impacts the results. The analysis of the Center Surround and Patch approaches demonstrates that the choice of algorithms can produce significantly different results. The final choice of approach should be based on both quantitative and qualitative results, perhaps with a slight bias towards the visual quality of the final fractal images.

It was also determined that inappropriate mask sizes and misinterpretation of D value statistics can further deteriorate the fractal approach. In particular, for the Intensity Statistics method:

(i) $D < 2.0$ and $|R| \geq .80$ values were found to be an indicator that an edge has been detected. The direction of the slope on the edge does not appear to affect the fractal model's ability to detect the edge.

(ii) $D > 3.0$ values are related to noise and usually have a 'very poor' associated goodness of fit. These values negatively impact the fractal-based texture segmentation and detection results and should be minimized when possible.

(iii) Small mask sizes tend to generate more $D > 3.0$ values than large ones.

(iv) Larger mask sizes tend to provide better R values for $2.0 \leq D \leq 3.0$.

(v) Improved detection capabilities of abnormalities in mammograms occurs if fractal dimensions with a 'good' R are displayed, including $2.0 \leq D \leq 3.0$ for

textural information and D < 2.0 for edge detection. Recall that D > 3.0 usually do not have 'good' R values. These abnormalities tend to have less texture (i.e., are smoother) than the surrounding tissue and consequently achieve a low D value with a high R when subjected to fractal analysis.

(vi) Removing as much background as possible from the image by cropping before applying the fractal method will significantly improve the D and R statistics (i.e., fewer D > 3.0 and more D values with good R values).

(vii) Correlation coefficient images are the most effective in the areas of the breast which are not near the breast edges.

The above conditions need to optimized for a particular set of x-ray images. A commercial package would require an automated optimization feature to ensure that errors in this area are minimized.

In conclusion, while this method seems "slightly ahead of its time" there is sufficient promise to continue work in this area. With the advent of digital radiography which eliminates several of the problems associated with the x-ray film processes, fractal-based texture segmentation may prove useful. At best I would currently recommend that this method be used only by those radiologists who are prepared to develop some degree of comfort with reading fractal images as an aid in their analysis of mammographic images.

6.2 Future Research

Future research could focus on a number of topics. Knowledge of the noise and sensor characteristics of the radiographic imaging system should be incorporated as part of the fractal model in the hopes of minimizing or correcting for the effects of scatter, collimator and detector blur within the x-ray image. Details of the type of film/screen combination and its optical characteristics could possibly assist in bringing out the details of the x-ray, especially in poorly contrasted areas. Also a detailed investigation of the digitization equipment (i.e., camera, lenses, x-ray illumination sources) is required to ensure that the digitized x-ray is of the highest quality possible. Precise calibration of the digitization equipment followed by an analysis of anomalies, should be accounted for in the fractal model whenever possible.

Finally, further tests need to be undertaken in a clinical setting and performed in close conjunction with radiologists who are experts in the field of mammography. A large collection of images is necessary for both supervised and blind tests. A database of visual fractal indicators needs be developed. This database should be correlated with the radiological indicators currently used for the diagnosis of cancer, and also with the clinical findings for patients who have undergone mammography.

Appendix A

Patient Synopses

This Appendix is organized as follows. For each patient, a brief synposis of the clinical report is given. This is followed by the digitized x-ray images, fractal images and correlation coefficient images for a few selected patients; all views of the left breast are given before those of the right. The fractal images were created using the Center Surround method, 9 x 9 mask. It should be noted that the images do not duplicate the fine detail or subtle gray-level variation that is evident when viewed on the workstation screen.

Patient 1:

Age: unknown

Diagnosis: A detailed report is not available. Microcalcifications are present and proved to be cancerous. The patient had a left mastectomy. The images for this patient are on the following page.

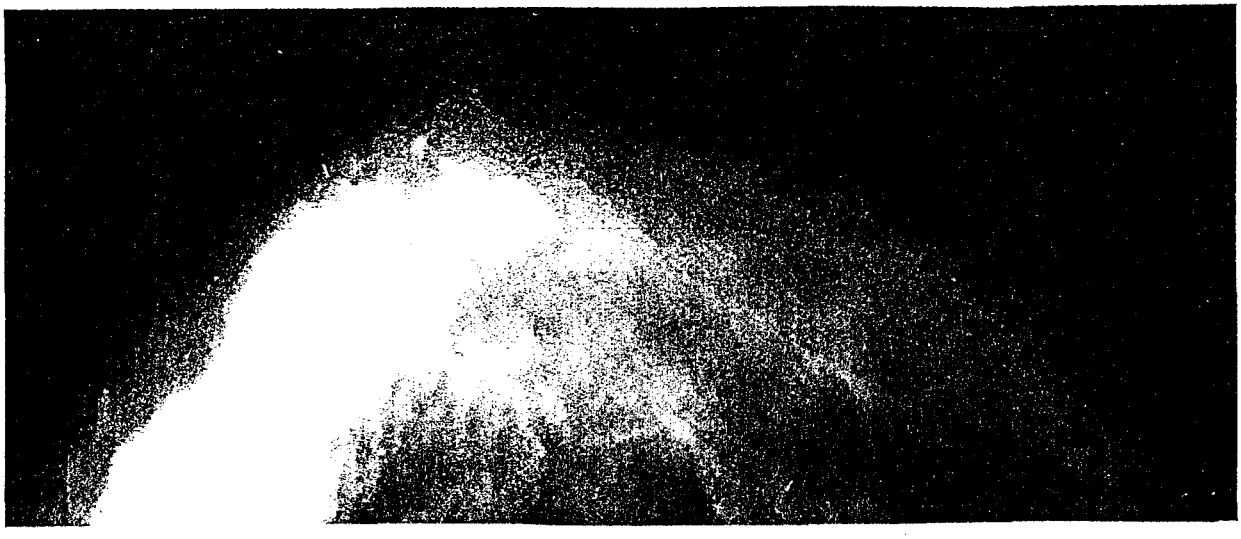

Figure A.1.1 (a) Left breast, x-ray image.

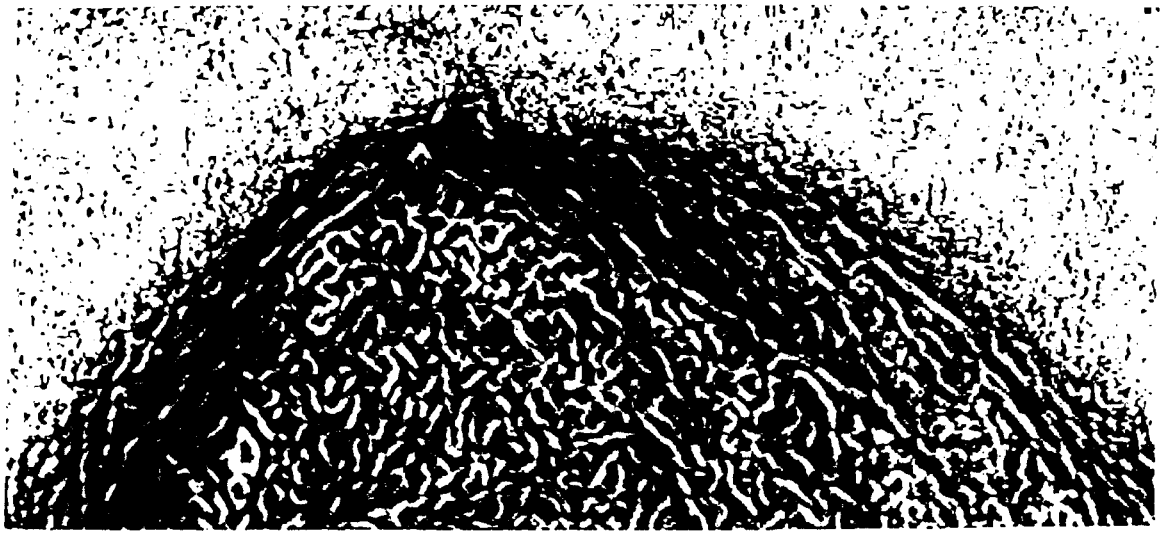

Figure A.1.1 (b) Left breast, fractal image.

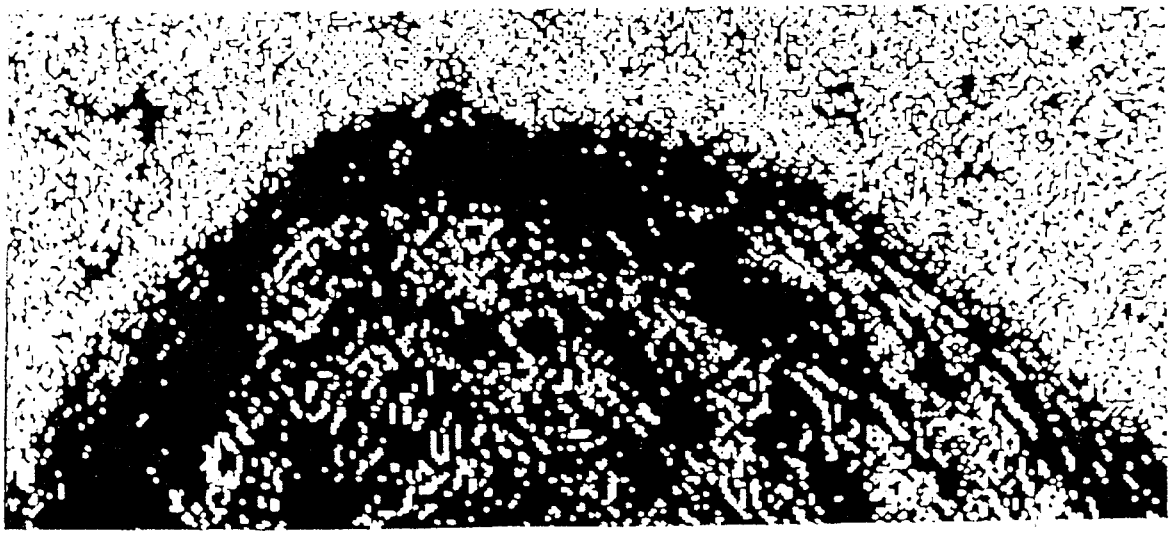

Figure A.1.1 (c) Left breast, correlation coefficient image.

Patient 2:

Age: 49

Diagnosis: Mammography of both breasts. Radiographic dense breast tissue (DY Wolfe classification) without evidence of a malignant lesion, skin thickening or nipple retraction. Ultrasound and light scans show a non-uniform pattern indicative of fibrocystic breast disease. Multiple cysts are noted in the left breast. The patient was given a negative mammographic report.

Figure A.2.1 (a) Left breast, x-ray image.

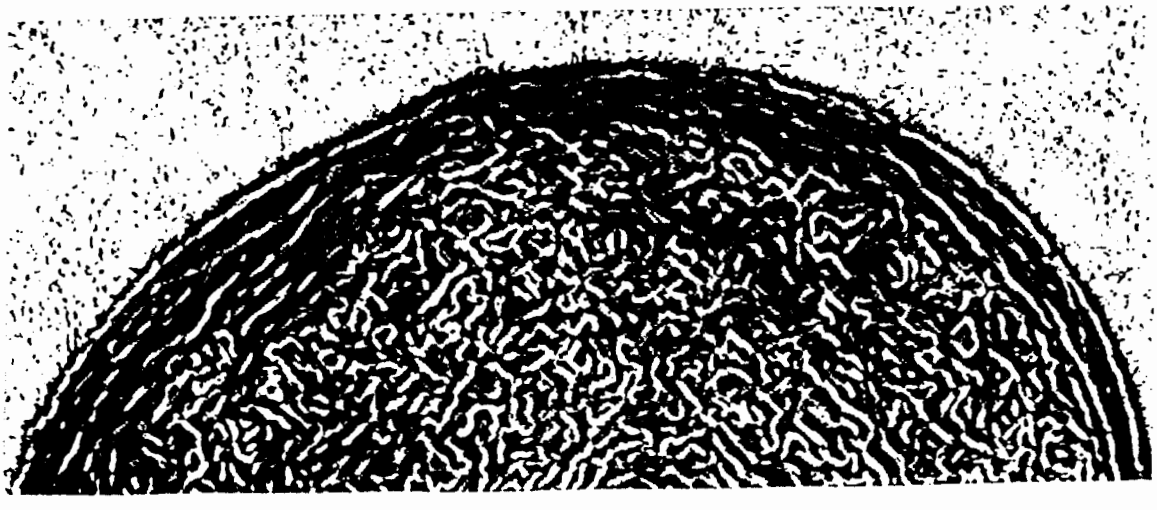

Figure A.2.1 (b) Left breast, fractal image.

Figure A.2.1 (c) Left breast, correlation coefficient image.

Figure A.2.2 (a) Left side breast, x-ray image.

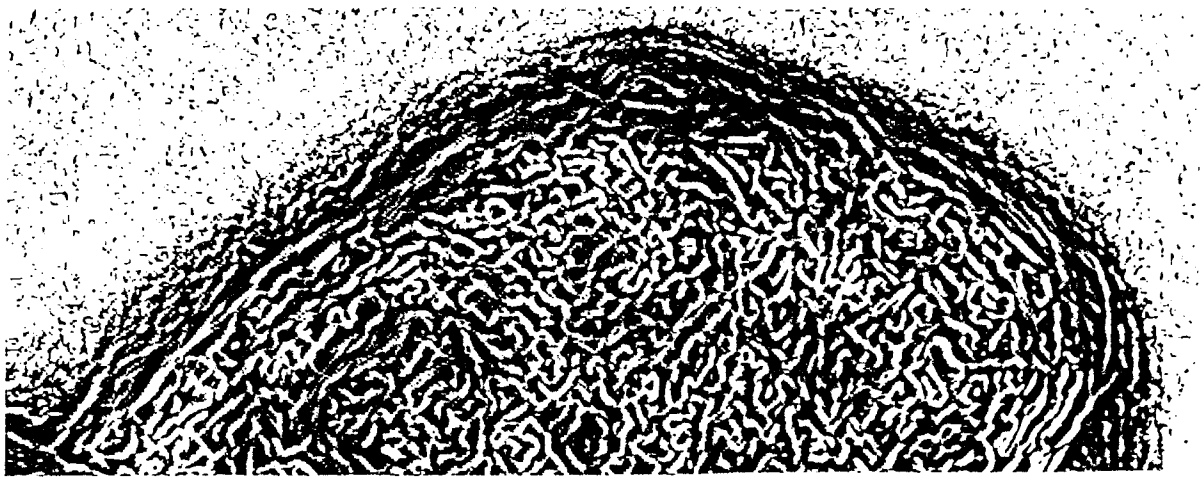

Figure A.2.2 (b) Left side breast, fractal image.

Figure A.2.2 (c) Left side breast, correlation coefficient image.

Patient 3:

Age: 43

Diagnosis: Mammography of both breasts. Radiographic dense breast tissue (DY Wolfe classification) without evidence of a malignant lesion, skin thickening or nipple retraction. Ultrasound and light scans show a non-uniform pattern indicative of fibrocystic breast disease. The patient was given a negative mammographic report.

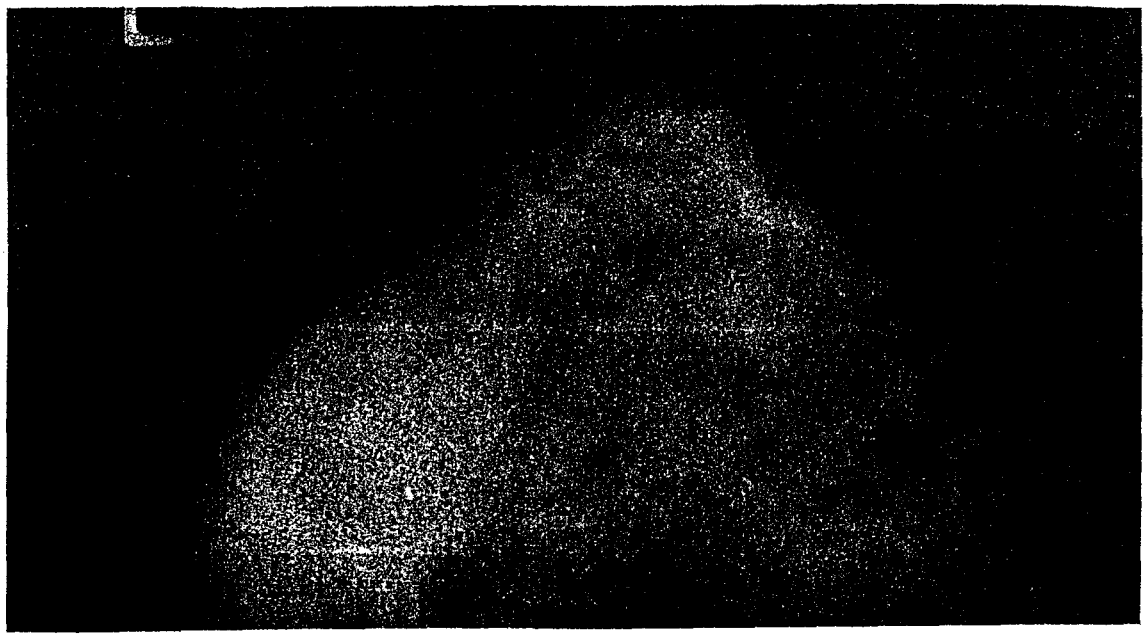

Figure A.3.1 (a) Left breast, x-ray image.

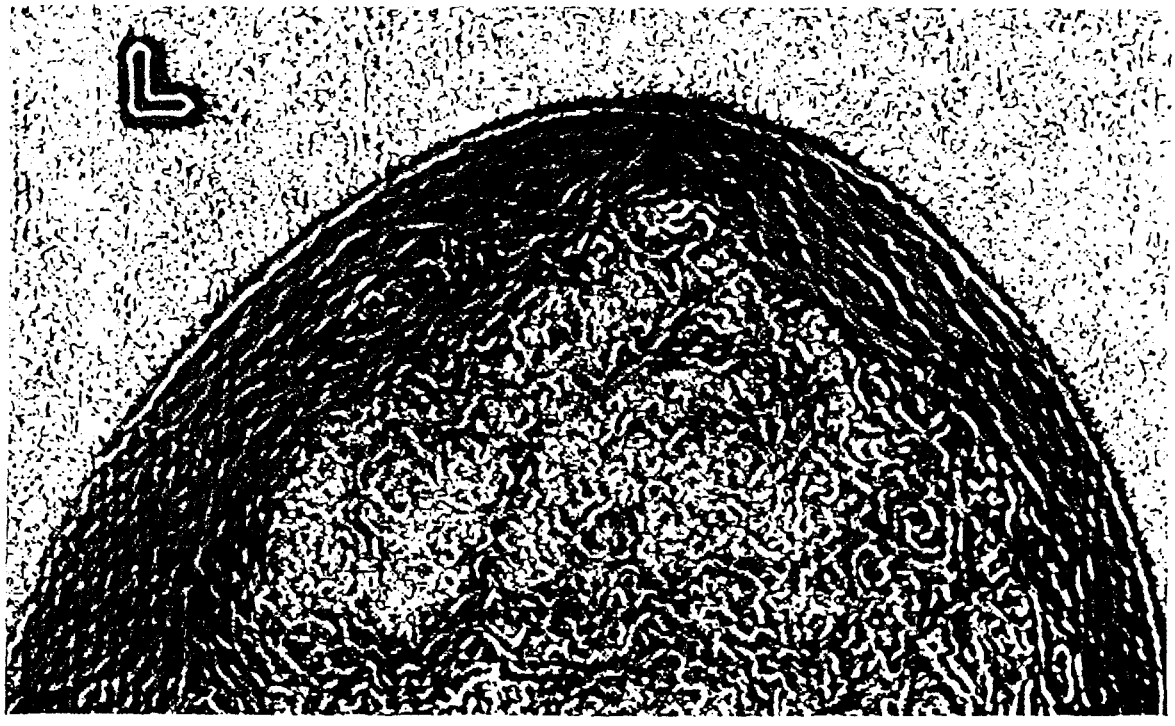

Figure A.3.1 (b) Left breast, fractal image.

Figure A.3.1 (c) Left breast, correlation coefficient image.

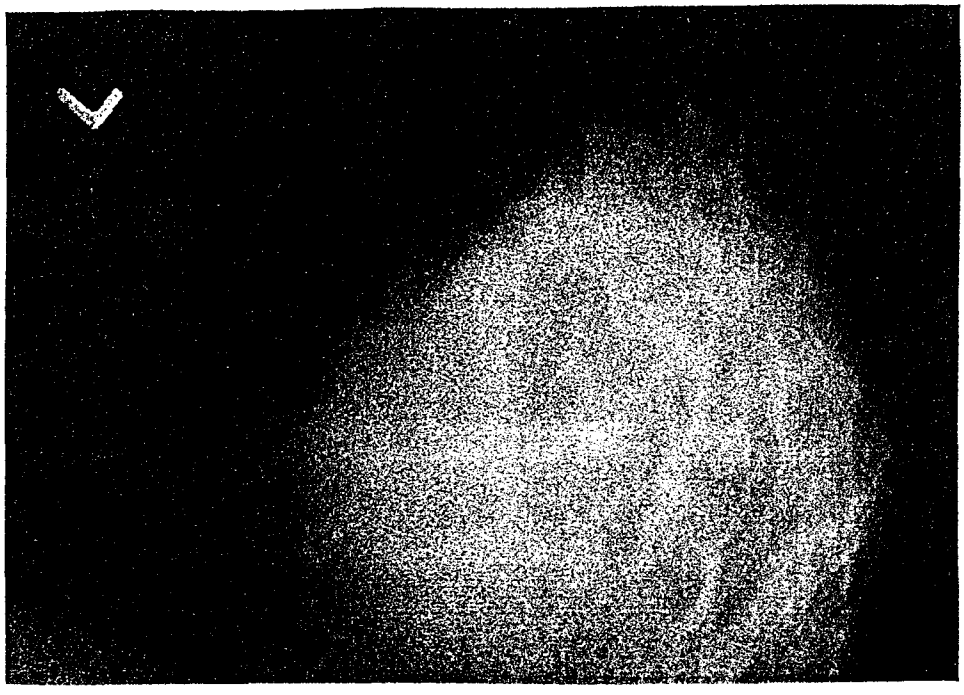

Figure A.3.2 (a) Left side breast, x-ray image.

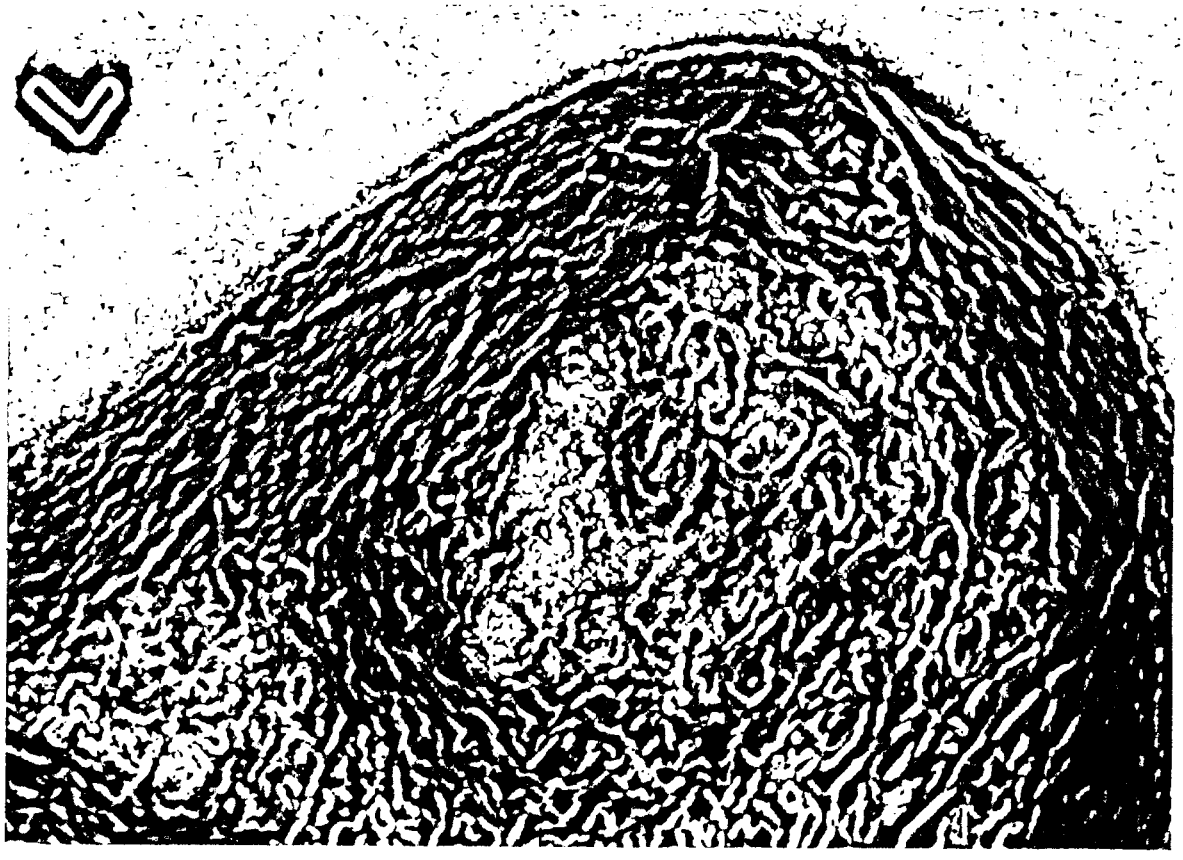

Figure A.3.2 (b) Left side breast, fractal image.

Figure A.3.3 (a) Right breast, x-ray image.

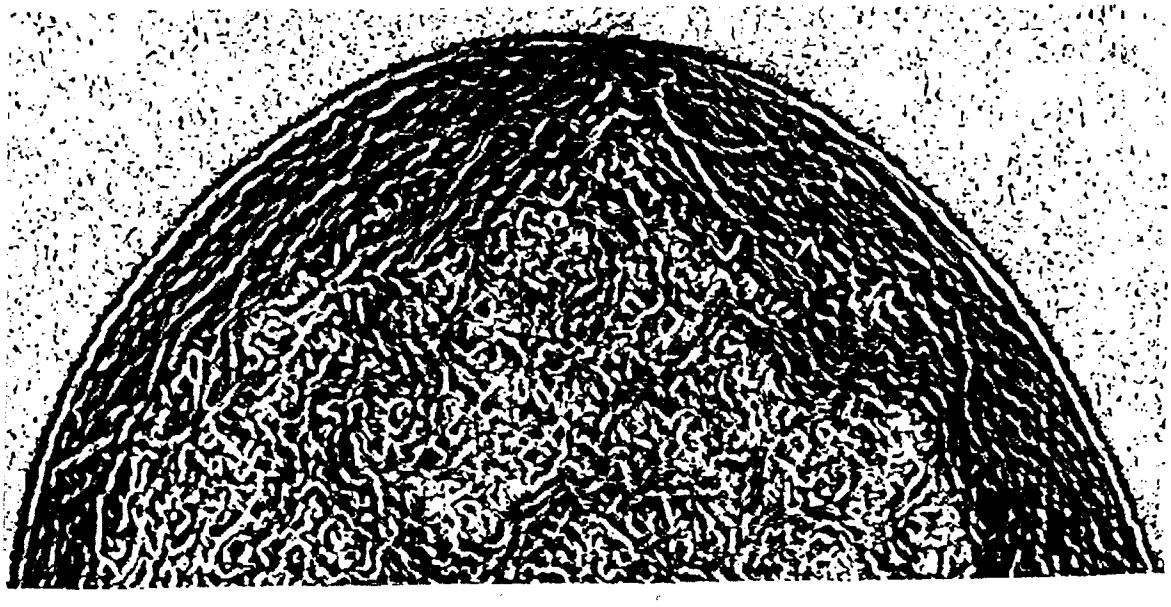

Figure A.3.3 (b) Right breast, fractal image.

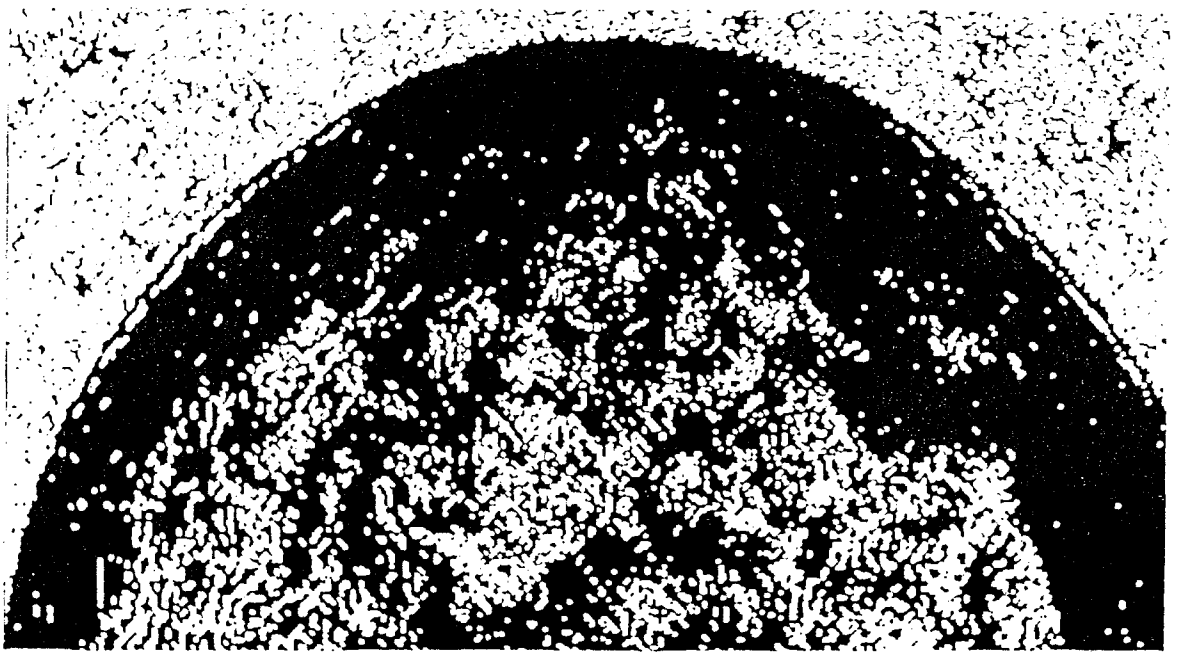

Figure A.3.3 (c) Right breast, correlation coefficient image.

Figure A.3.4 (a) Right side breast, x-ray image.

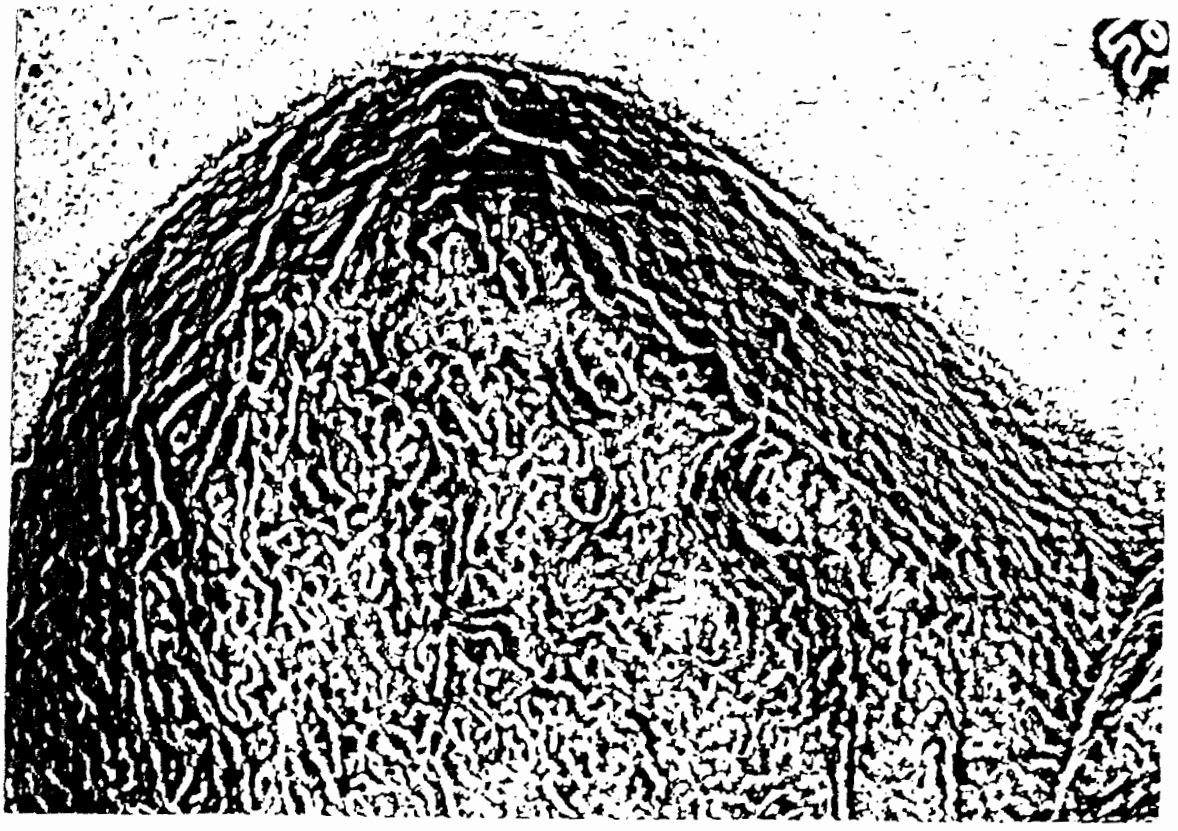

Figure A.3.4 (b) Right side breast, fractal image.

Patient 4:

Age: 44

Diagnosis: Mammography of both breasts. Radiographic dense breast tissue (DY Wolfe classification) without evidence of a malignant lesion, skin thickening or nipple retraction. Ultrasound and light scans show a non-uniform pattern indicative of fibrocystic breast disease. The light scan and ultrasound indicate the presence of a cyst in the periareolar areas of both the left and right breasts not observed by mammography.

Figure A.4.1 (a) Left breast, x-ray image.

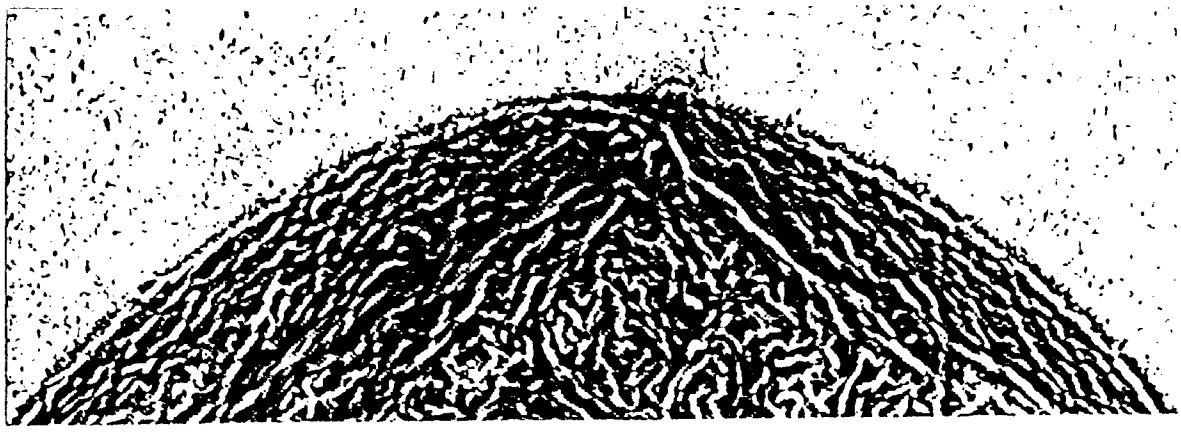

Figure A.4.1 (b) Left breast, fractal image.

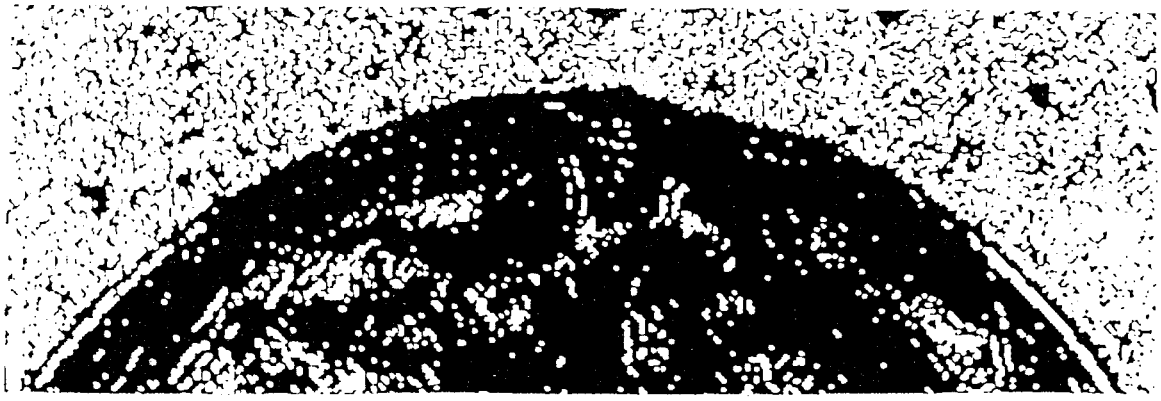

Figure A.4.1 (c) Left breast, correlation coefficient image.

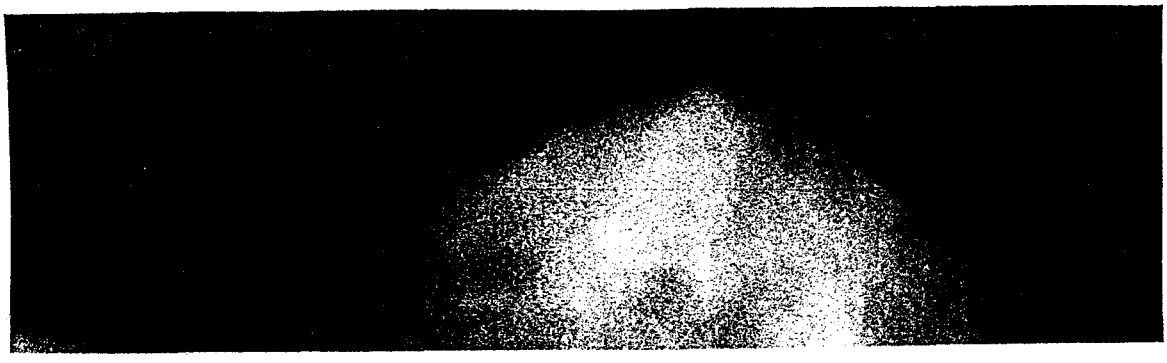

Figure A.4.2 (a) Left side breast, x-ray image.

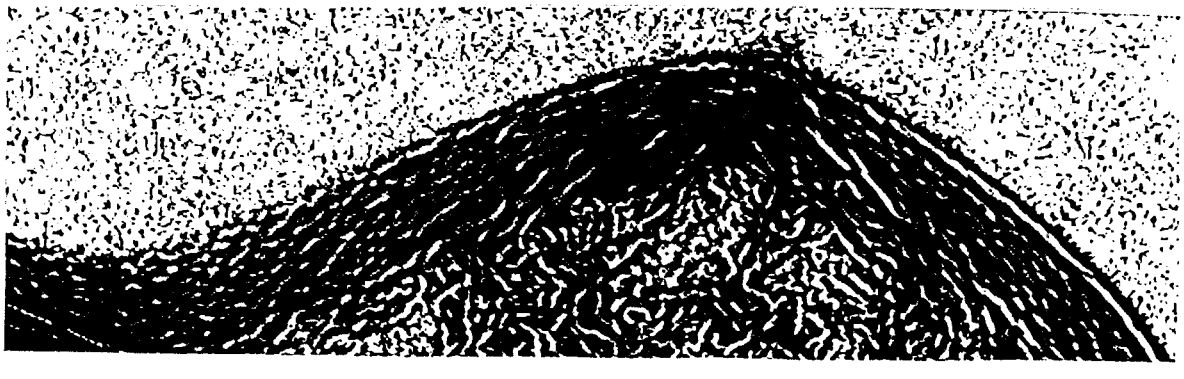

Figure A.4.2 (b) Left side breast, fractal image.

Figure A.4.3 (a) Right breast, x-ray image.

Figure A.4.3 (b) Right breast, fractal image.

Figure A.4.3 (c) Right breast, correlation coefficient image.

Figure A.4.4 (a) Right side breast, x-ray image.

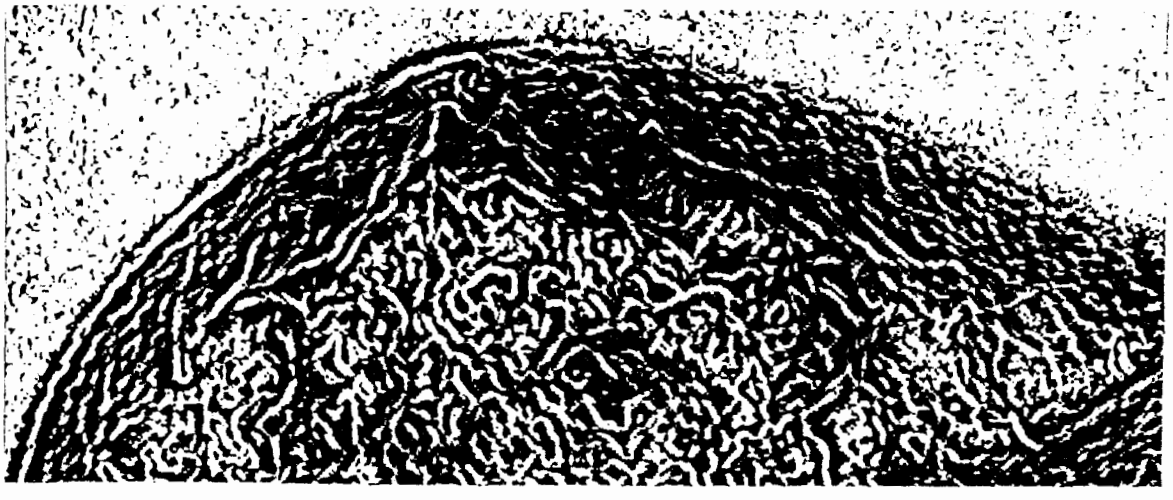

Figure A.4.4 (b) Right side breast, fractal image.

Patient 5:

Age: 47

Diagnosis: Mammography of both breasts. Radiographic dense breast tissue (DY Wolfe classification) without evidence of a malignant lesion, skin thickening or nipple retraction. Ultrasound and light scans show a non-uniform pattern indicative of fibrocystic breast disease. The light scan and ultrasound indicate the presence of a cyst in the left breast not observed by mammography.

Figure A.5.1 (a) Left breast, x-ray image.

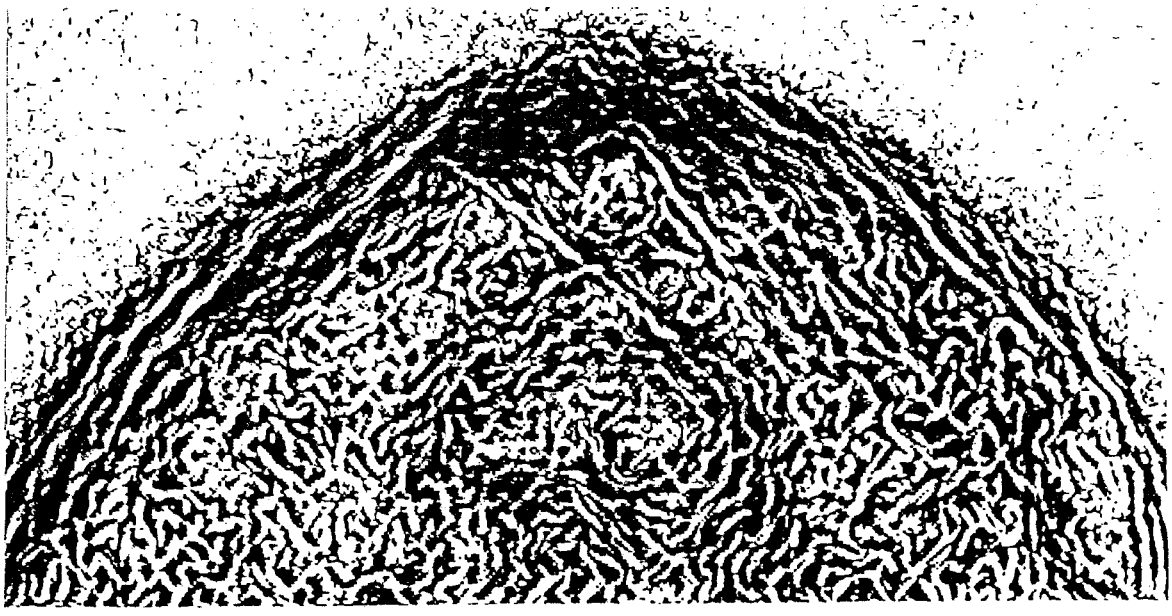

Figure A.5.1 (b) Left breast, fractal image.

Figure A.5.1 (c) Left breast, correlation coefficient image.

Patient 6:

Age: 39

Diagnosis: Mammography of both breasts. Radiographic dense breast tissue (DY Wolfe classification) without evidence of a malignant lesion, skin thickening or nipple retraction. Ultrasound and light scans show a non-uniform pattern indicative of fibrocystic changes. There is no evidence of a lesion suspicious for malignancy. The patient was given a negative mammographic report.

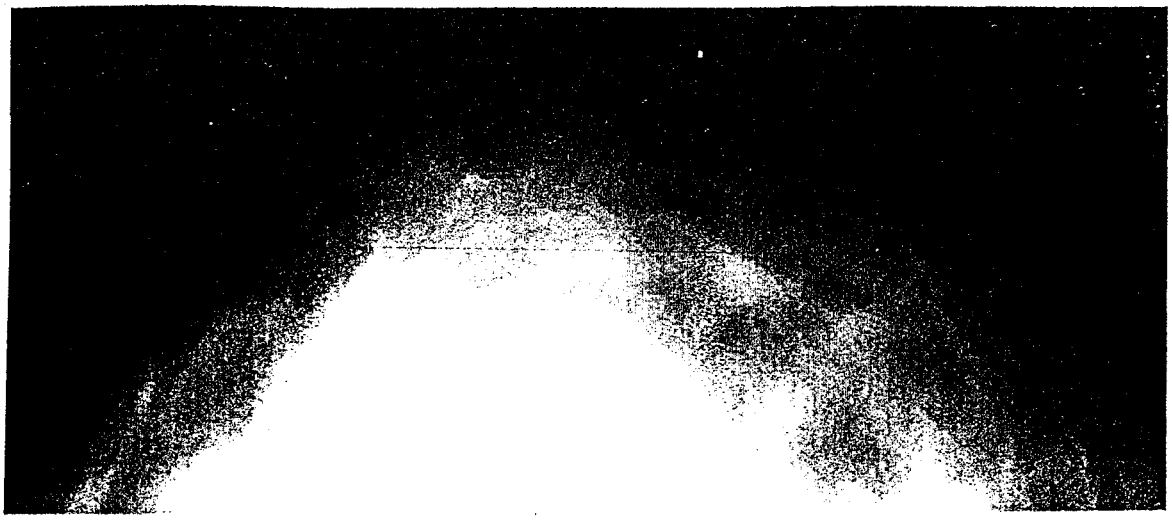

Figure A.6.1 (a) Left breast, x-ray image.

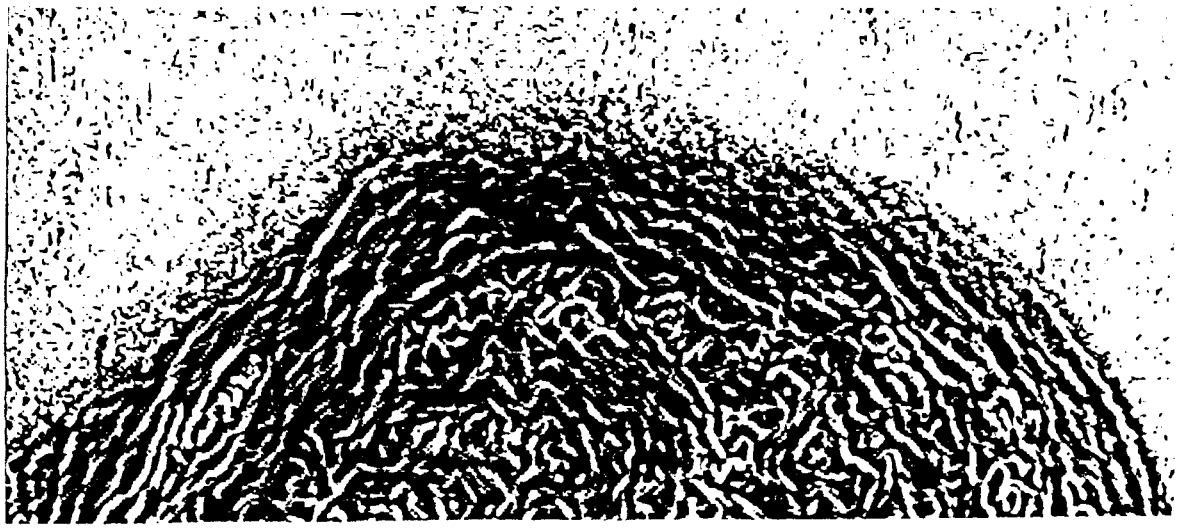

Figure A.6.1 (b) Left breast, fractal image.

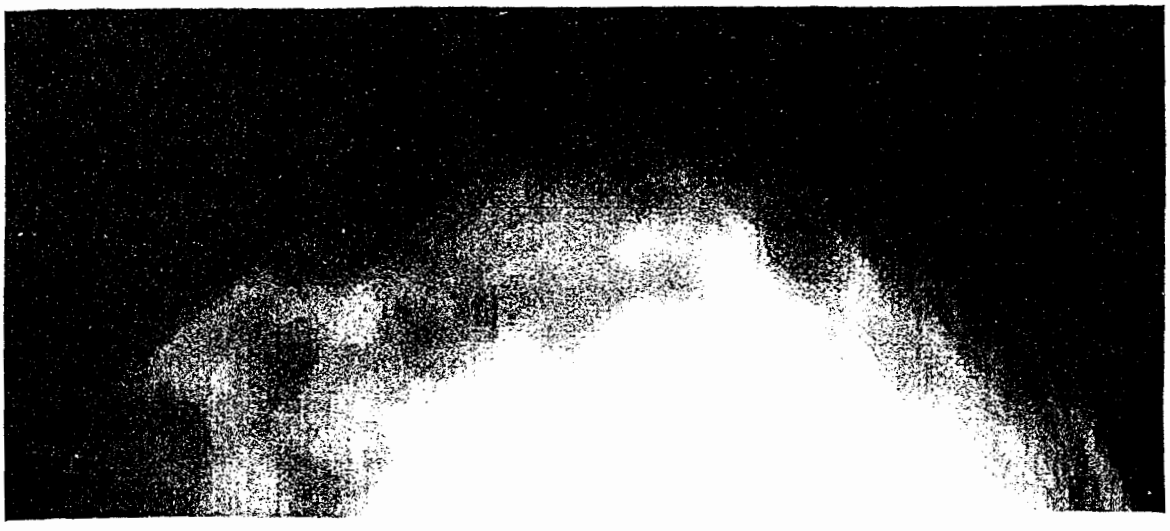

Figure A.6.2 (a) Right breast, x-ray image.

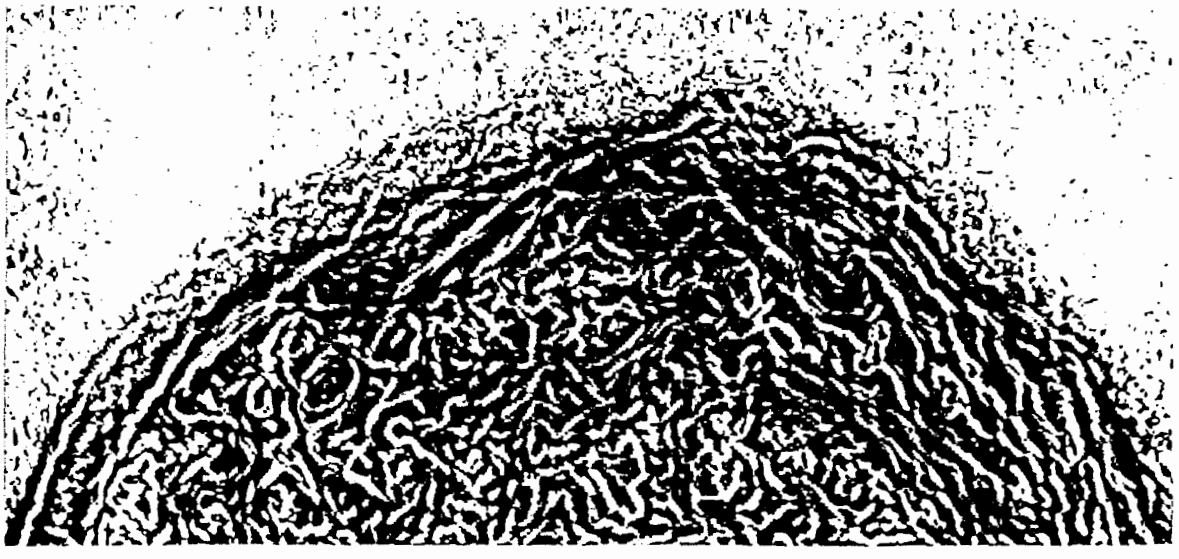

Figure A.6.2 (b) Right breast, fractal image.

Patient 7:

Age: 36

Diagnosis: Mammography of both breasts. Radiographic dense breast tissue (DY Wolfe classification) without evidence of a malignant lesion, skin thickening or nipple retraction. Ultrasound and light scans show a non-uniform pattern indicative of fibrocystic changes. There is no evidence of a lesion suspicious for malignancy. The patient was given a negative mammographic report.

Figure A.7.1 (a) Left breast, x-ray image.

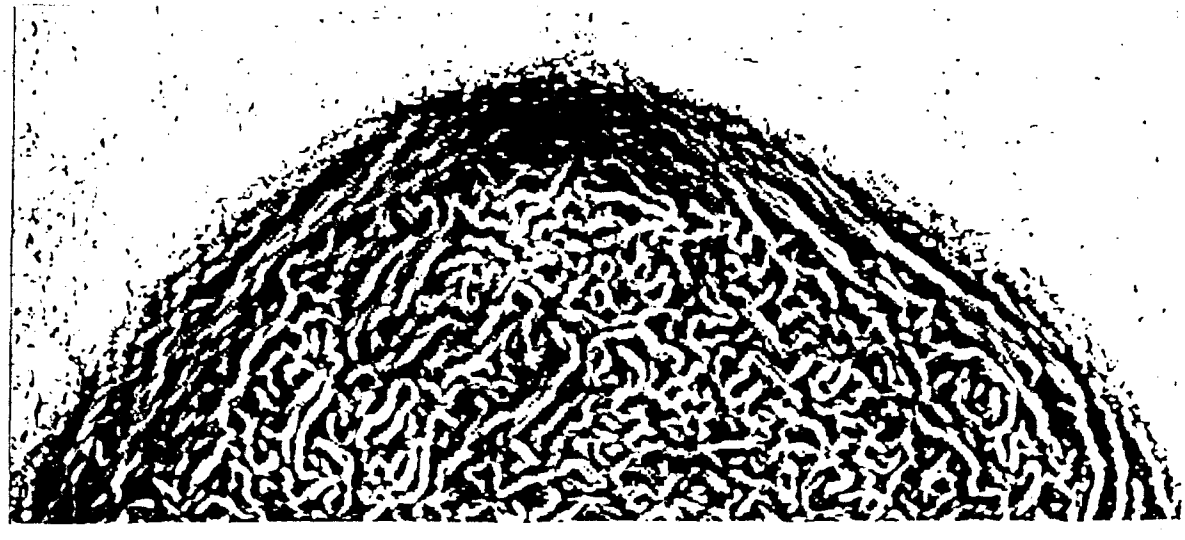

Figure A.7.1 (b) Left breast, fractal image.

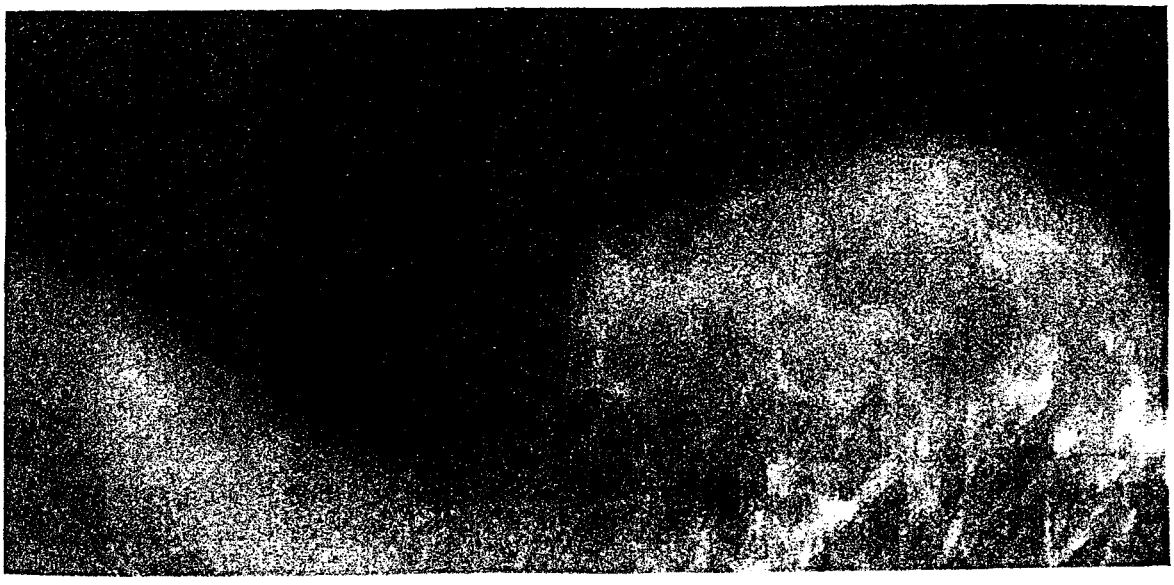

Figure A.7.2 (a) Left side breast, x-ray image.

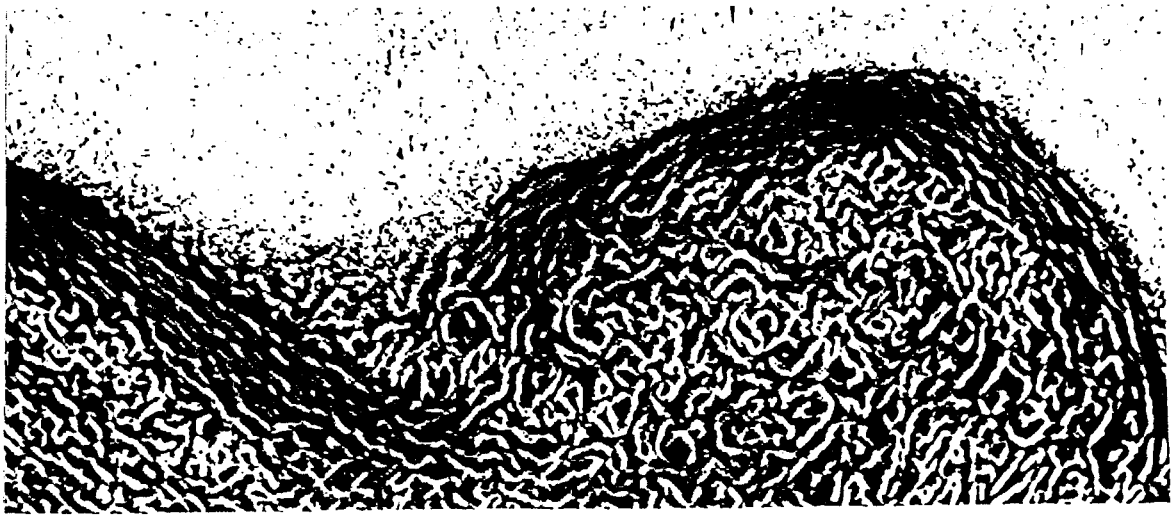

Figure A.7.2 (b) Left side breast, fractal image.

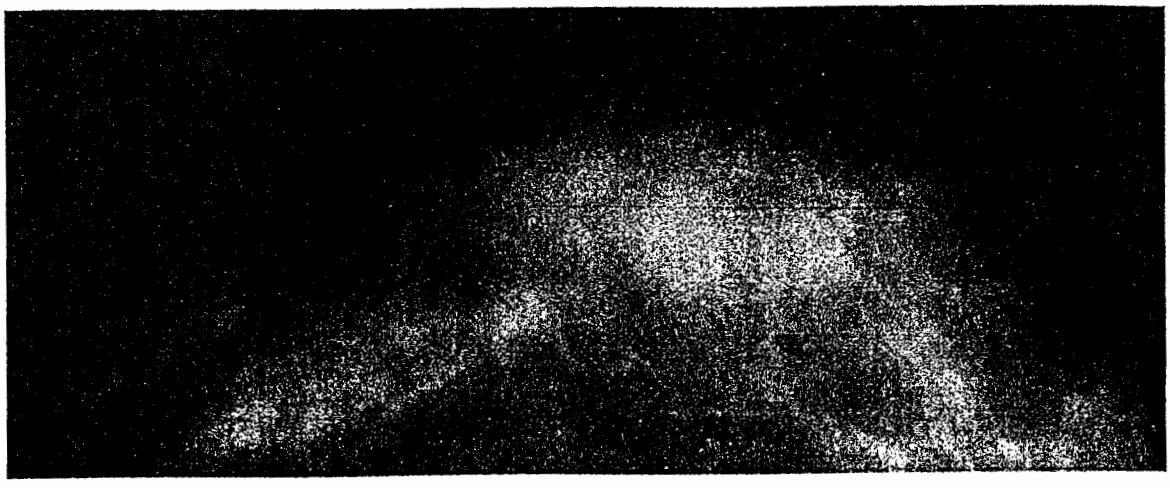

Figure A.7.3 (a) Right breast, x-ray image.

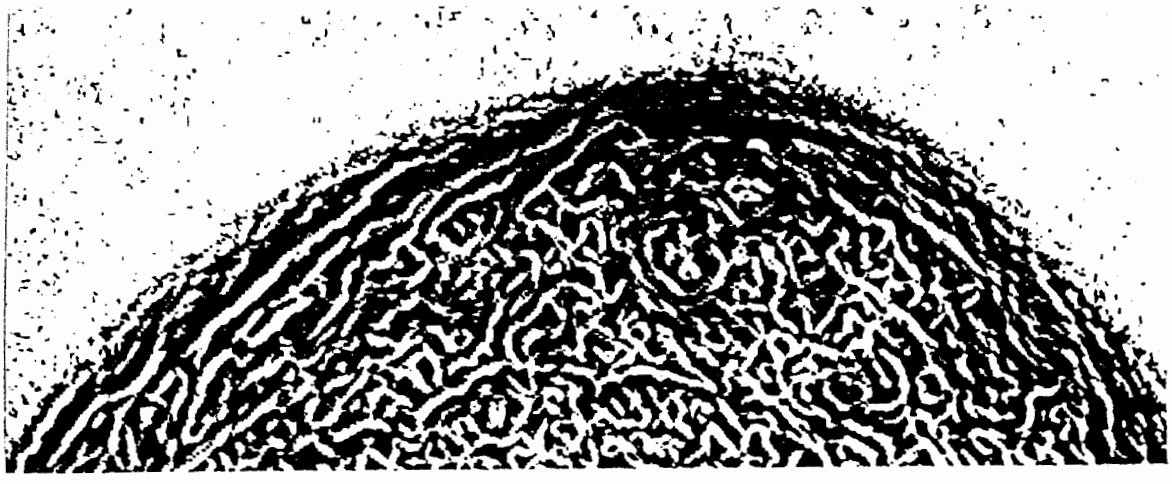

Figure A.7.3 (b) Right breast, fractal image.

Patient 8:

Age: 64

Diagnosis: Mammography of both breasts. Mammography of right breast indicates a malignant lesion at the 12 o'clock position. Ultrasound, light scans and pathological report confirm the malignancy. A right mastectomy was performed. Mammography of the left breast indicates dense breast tissue without evidence of a malignant lesion, skin thickening or nipple retraction. A left mastectomy was performed within one year of having taken this mammogram.

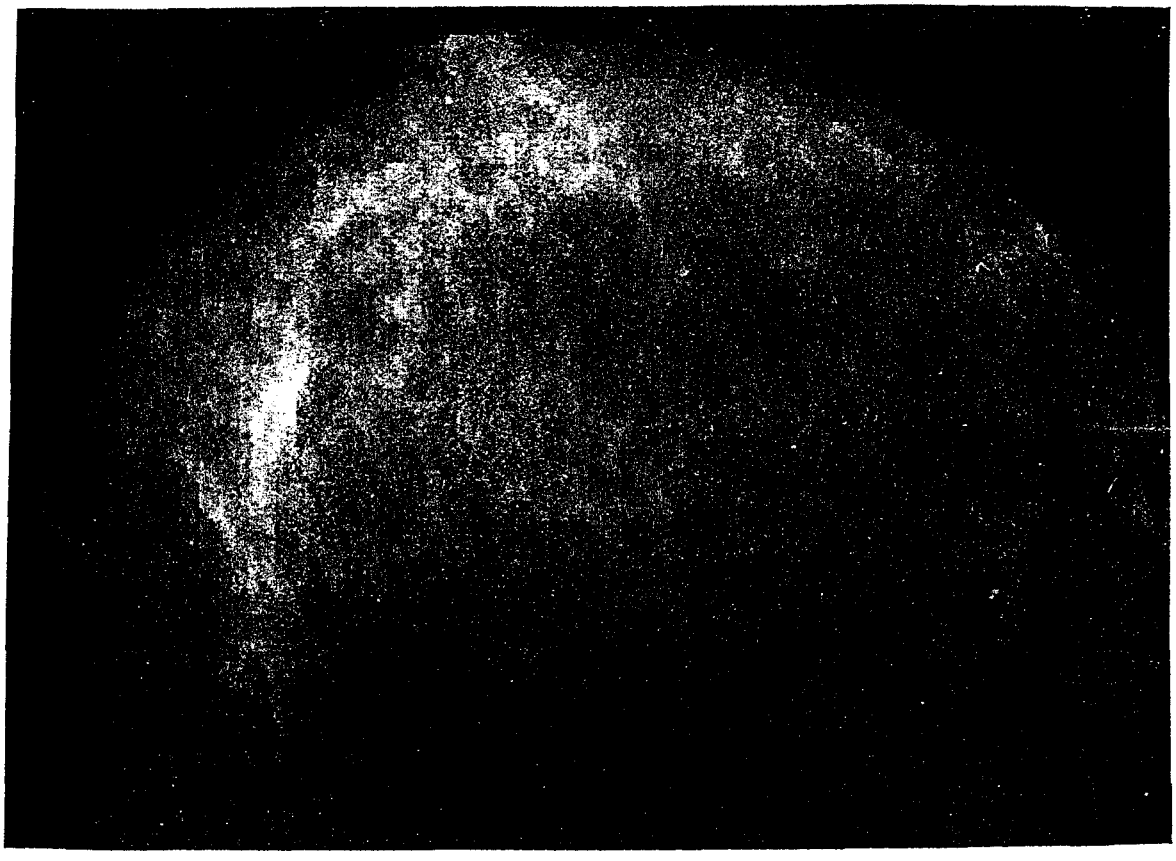

Figure A.8.1 (a) Left breast, x-ray image.

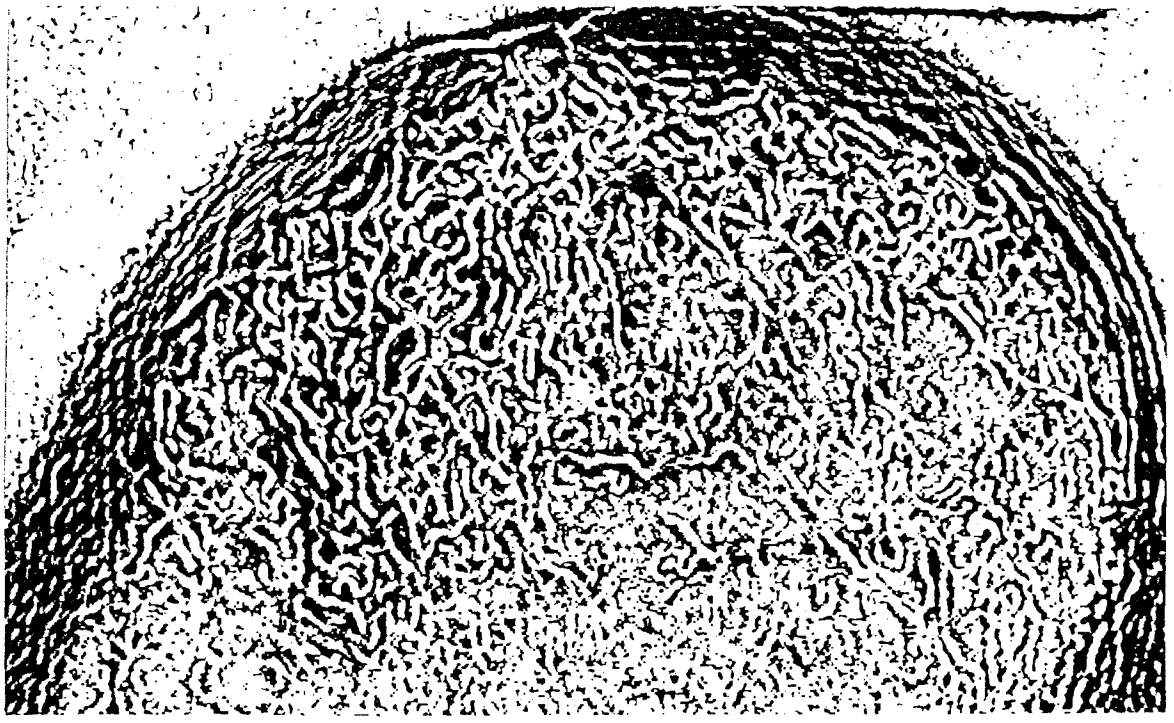

Figure A.8.1 (b) Left breast, fractal image.

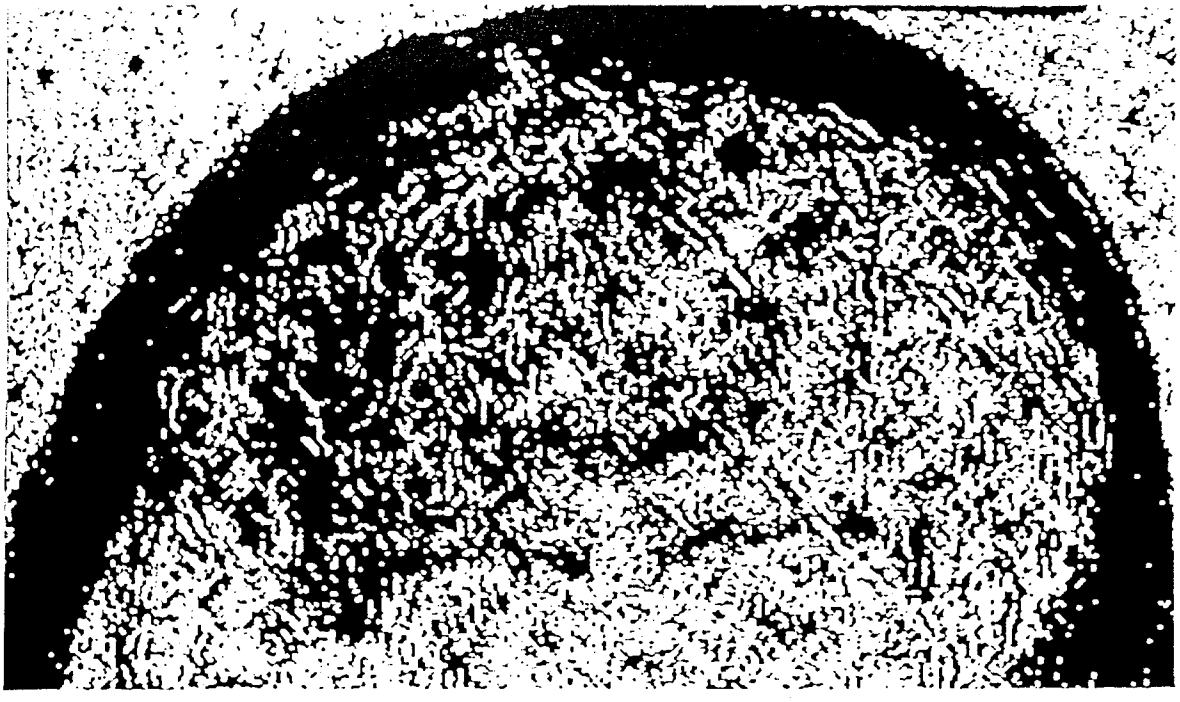

Figure A.8.1 (c) Left breast, correlation coefficient image.

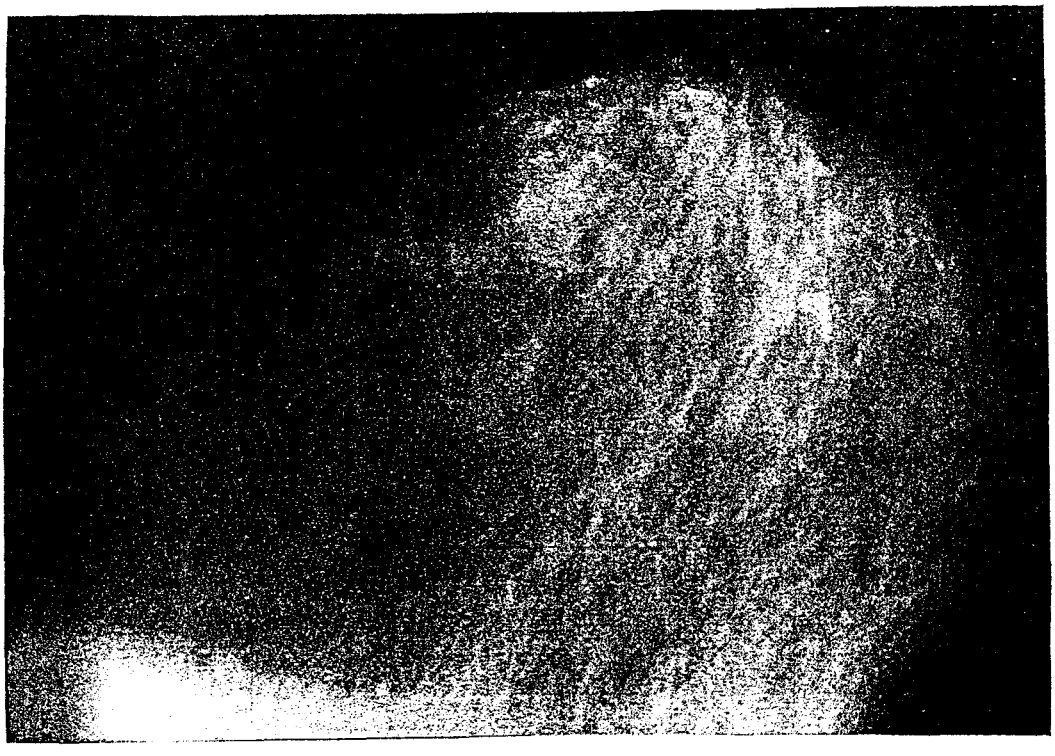

Figure A.8.2 (a) Left side breast, x-ray image.

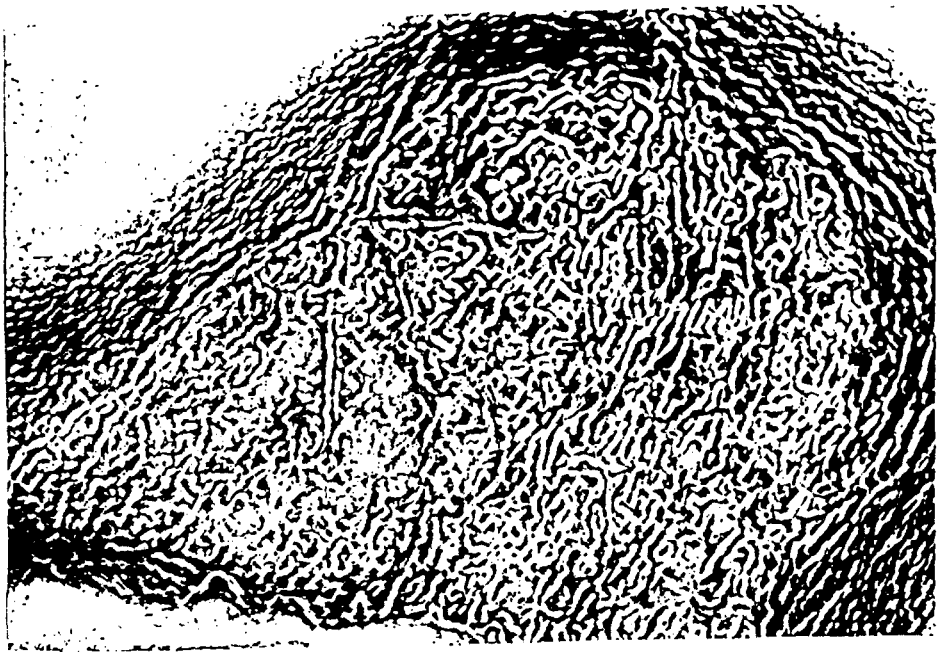

Figure A.8.2 (b) Left side breast, fractal image.

Figure A.8.3 (a) Right breast, x-ray image.

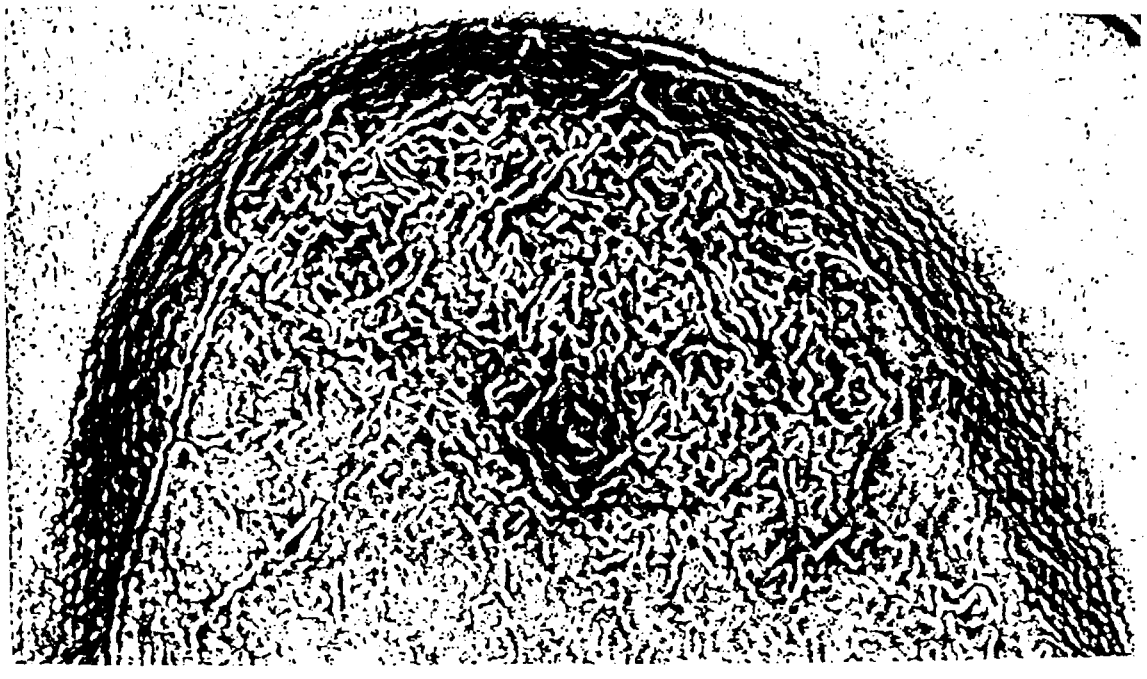

Figure A.8.3 (b) Right breast, fractal image.

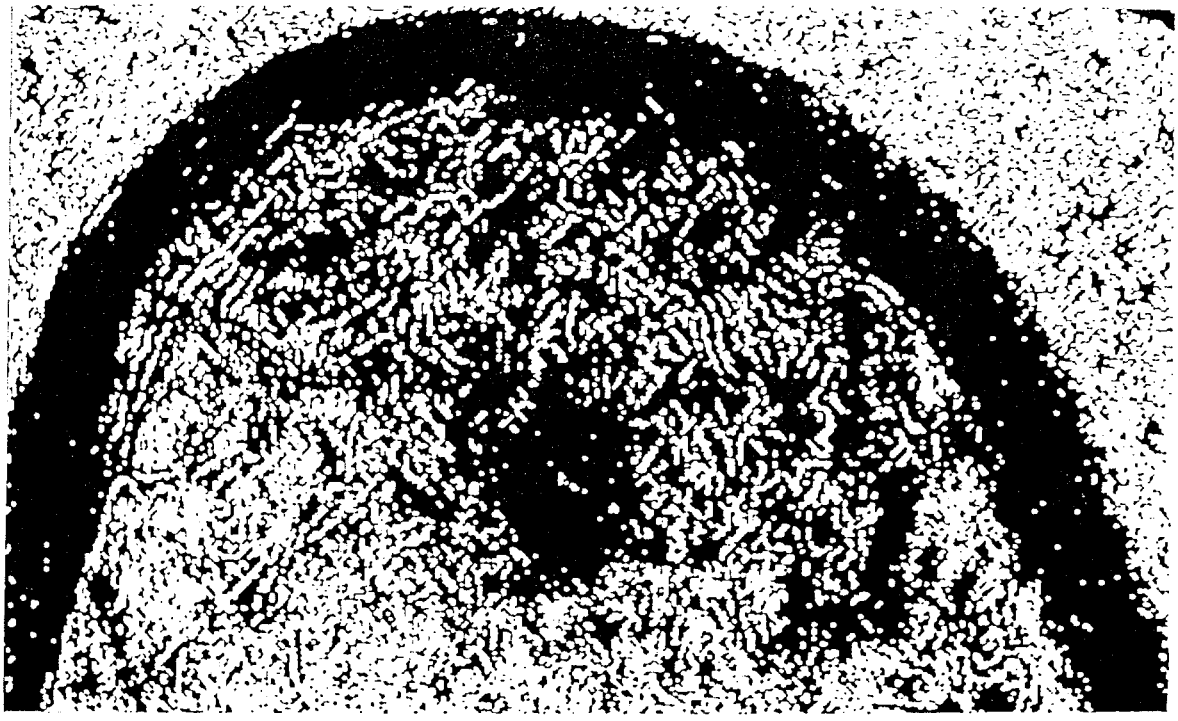

Figure A.8.3 (c) Right breast, correlation coefficient image.

Figure A.8.4 (a) Right side breast, x-ray image.

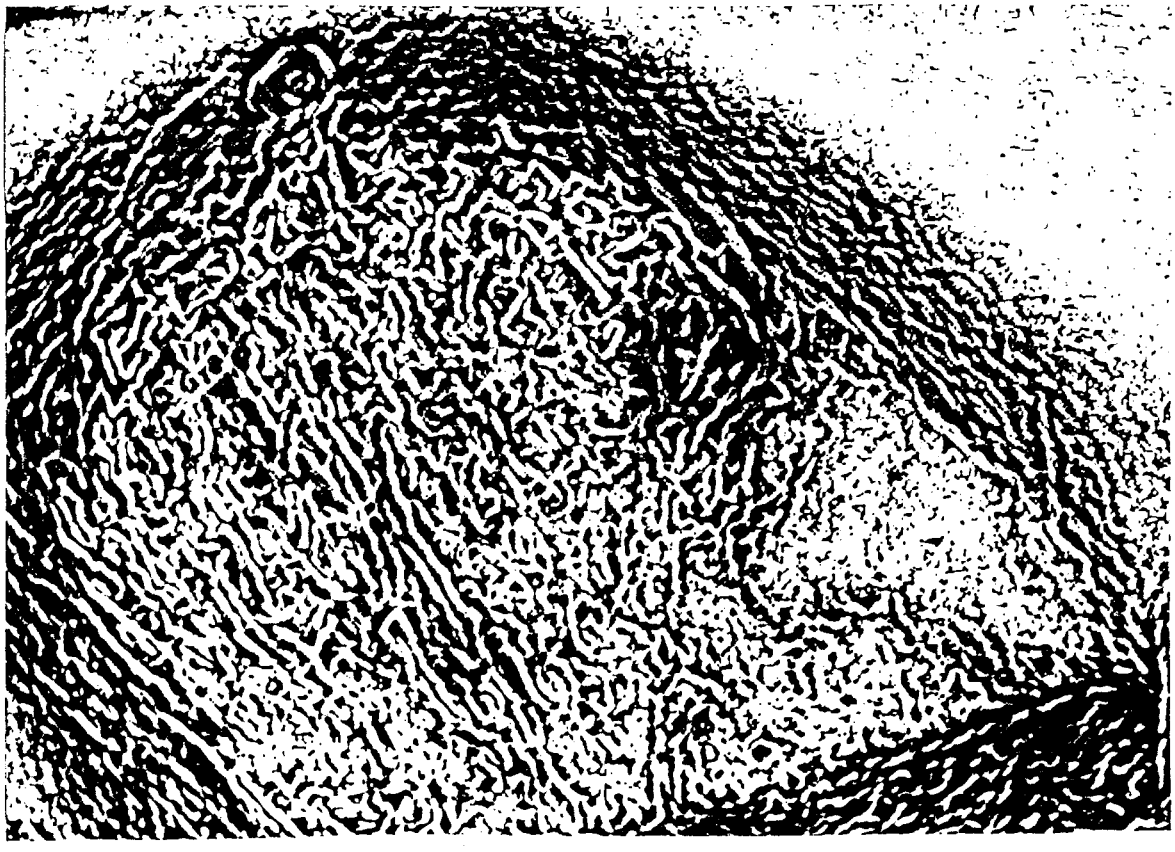

Figure A.8.4 (b) Right side breast, fractal image.

Patient 9:

Age: 30

Diagnosis: Chest x-ray demonstrates the presence of an oval mass approximately 3 cm in diameter in the right lower lung zone. The patient was diagnosed as having poorly differentiated squamous cell bronchogenic carcinoma of the right lower lobe.

Figure A.9.1 (a) Chest, x-ray image.

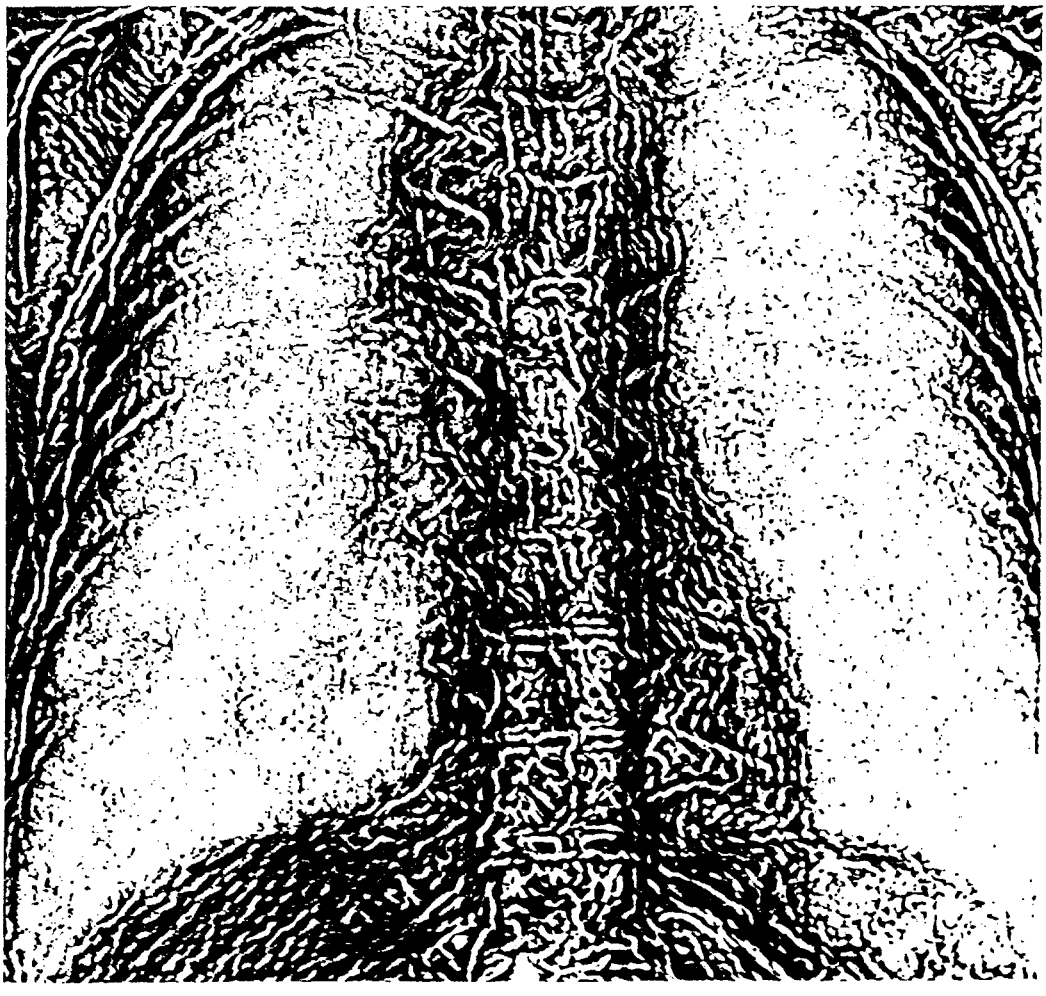

Figure A.9.1 (b) Chest, fractal image.

References

[Adel81] Adler, R.J.
The Geometry of Random Fields
John Wiley & Sons Ltd., Chichester, 1981

[AnHu77] Andrews, H.C. and Hunt, B.R.
Digital Image Restoration
Prentice-Hall, Inc., Englewood Cliffs, 1977

[AcGo72] Ackerman, L.V., Gose, E.
"Breast lesion classification by computer and xeroradiography"
Cancer, **(30)**, 1972, 1025-1035

[AWNB87] Armstrong, P., Wastie, M., Norman, A., and Brenbridge, A.
Diagnostic Imaging, 2nd Ed.
Blackwell Scientific Publications, Oxford, 1987

[Cao88] Cao, Q., Brosnan, T., Macovski, A., Nishimura, D.
"Least squares approach in measurement-dependent filtering for selective medical images"
IEEE Transactions on Medical Imaging, **(7:2)**, June 1988, 154-160

[Carg88] Cargill, E., Barrett, H., Fiete, R., Ker, M., Patton, D., Seeley, G.
"Fractal physiology and nuclear medicine scans"
SPIE Medical Imaging II, **(914)**, 1988, 355-361

[CBRE88] Caseldine, J., Blamey, R., Roebuck, E., and Elston, C.
Breast Disease for Radiographers
John Wright, London, 1988

[CDVM87] Chan, H.-P., Doi, K., Vyborny, C., Metz, C., MacMahon, H., Jokich, P., Galhotra, S.
"Digital mammography: development of a computer-aided system for detection of microcalcifications"
SPIE Medical Imaging, **767**, 1987, 367-370

[CDVS87] Claessens, M., Delcour, C., Vandenbosch, G., Struyven, J.
"A computer and automatic method for the determination of vessel diameters"
Ann Radiol (Paris), **30 (2)**, 1987, 110-114

[ChDF89] Chen, C.-C., DaPonte, J., and Fox., M.
"Fractal feature analysis and classification in medical imaging"
IEEE Transactions on Medical Imaging, **8 (2)**, June 1987, 133-142

[Conn85] Conners, R.
"Computer vision in digital radiography"
Proc. Intl. Symp. Computer Assisted Radiology—CAR '85, 1985, 451-460

[CSHJ90] Caldwell, C., Stapleton, S., Holdsworth, D.,Jong, R., Weiser, W., Cooke, G., Yaffe, M.
"Characterization of mammary parenchymal pattern by fractal dimension"
Physics in Medicine and Biology, **35 (2)**, 1990, 235-247

[DaFo88] DaPonte, J., Fox., M.
"Enhancement of chest radiographs with gradient operators"
IEEE Transactions on Medical Imaging, **7 (2)**, 1988, 109-117

[DBGo86] Dhawan, A., Buelloni, G., Gordon, R.
"Enhancement of mammographic features by optimal adaptive neighborhood image processing"
IEEE Transactions on Medical Imaging, **(MI-5:1)**, 1986, 8-15

[Dell87] Dellepiane, S., Serpico, S., Vernazza, G., Viviani, R.
"Fractal-based image analysis in radiological applications"
SPIE Visual Communications and Image Processing II (1987), **845**, 1987, 396-403

[DhLe88] Dhawan, A.P., Le Royer,
"Mammographic feature enhancement by computerized image processing"
Computer Methods and Programs Biomedicine, **(27)**, 1988, 23-35

[DLGo86] Dhawan, A., Le Royer, E., Gordon, R.
"Adaptive neighborhood image processing for feature enhancement of film-mammograms"
Proc IEEE 8th Ann Conf Eng Med and Biol Soc , 1986, 1096-1100

[Evans87] Evans, David J.
Video Camera Calibration and Radiometric Correction
Master of Science Thesis in the Department of Geography
Simon Fraser University, 1987

[Falc85] Falconer, K.J.
The geometry of fractal sets
Cambridge University Press, Cambridge, 1985

[FaOl87] Fam, B., and Olson, S.
"X-ray enhancement in the presence of noise"
SPIE Medical Imaging, **767**, 1987, 416-426

[Feig79] Feig, S., Schwartz, G., Nerlinger, R., Edeiken, J.
"Prognostic factors of breast neoplasms detected on screening by mammography and physical examination"
Radiology, **(133)**, 1979, 577-582

[Fink89] Fink, D. G. and Christiansen, D.
Electronics Engineers' Handbook
3rd Edition, McGraw-Hill Book Company, New York, 1989

[GBCo87] Gold, R., Bassett, L., Coulson, W.
"Diagnosis"
Breast Cancer Detection, 2nd Ed., (Bassett, L. and Gold, R. (Eds.))
Grune & Stratton, Inc., Orlando, 1987, 15-65

[GBKS87] Gold, R., Bassett, L., Kimme-Smith, C.
"Introduction to Breast Imaging: State of the Art and Future Directions"
Breast Cancer Detection, 2nd Ed., (Bassett, L. and Gold, R. (Eds.))
Grune & Stratton, Inc., Orlando, 1987, 3-13

[GDMa87] Giger, M., Doi, K., MacMahon, H.
"Computerized detection of lung nodules in digital chest radiographs"
SPIE Medical Imaging, **767**, 1987, 384-386

[GoRa84] Gordon, R., Rangayyan, R.M.
"Feature enhancement of film mammograms using fixed and adaptive neighborhoods"
Applied Optics, (**23**), 1984, 560-564, *Correction. ibid.* 2055

[GoWe87] Goldberger, A.L., West, B.J.,
"Fractals in physiology and medicine"
The Yale Journal of Biology and Medicine, (**60**), 1987, 421-435.

[GRRW87] Gale, A., Roebuck, E., Riley, P., Worthington, B.
"Computer aids to mammographic diagnosis"
The British Journal of Radiology, (**60**), September 1987, 887-891

[Hara79] Haralick, R.M.
"Statistical and structural approaches to texture"
Proceedings of the IEEE, **67** (**5**), 1979, 786-804

[HHKi85] Harris, J., Hellman, S., and Kinne, D.
"Limited surgery and radiotherapy for early breast cancer"
New England Journal of Medicine, **313**, 1985, 1365-1368

[HKMS87] Hakim, N., Kaufman, J., Mont, M., Schmukler, R., Ohley, W., Lundahl, T., Meadows, H., Soifer, T., Siffert, R.
"A digital image processing approach to diagnosis of osteoporosis"
IEEE Proceedings Twentieth Asilomar Conference on Signals, Systems and Computers, 1987, 631-634

[HSAA79] Hand, W., Semmlow, J., Ackerman, L., Alcorn, F.,
"Computer screening of xeromammograms: a technique for defining suspicious areas of the breast"
Comput Biomed Res, (**12**), 1979, 445-460

[IFFlib90] Department of Computing Science
Image File Format (IFF) Software Library
Simon Fraser University, 1990

[KCRW89] Kuklinski, W., Chandra, K., Ruttirmann, U., Webber, R.
"Application of fractal texture analysis to segmentation of dental radiographs"
SPIE Medical Imaging III: Image Processing, **1092**, 1989, 111-117

[KeCh89] Keller, J., Chen, S.
"Texture description and segmentation through fractal geometry"
Computer Vision, Graphics, and Image Processing, **45**, 1989, 150-166

[KHNM87] Kaufman, J., Hakim, N., Nasser, P., Mont, M., Klion, M., Pilla, A., Siffert, R.
"Application of digital image processing and pattern recognition to diagnosis of osteoporosis"
Proc. of the IEEE Ninth Annual Conference of the Engineering in Medicine and Biology Society, 1987, 1334-1335

[KOSk77] Kimme, C., O'Loughlin, B.J., Sklansky, J.
"Automatic detection of suspicious abnormalities in breast radiographs"
Data structures, computer graphics, and pattern recognition,
(Klinger, A., Fu, K., and Kunii,T. (Eds.))
New York: Academic Press, 1977, 427-447

[Knic90] Knickerbocker, N.
"Combating breast cancer"
Your Better Health Magazine, Vol. 1 No. 1,
B.C. Ministry of Health, Victoria, 1990, 5

[KSFW79] Kimme-Smith, C., Frankl, G., Wassel, G., Sklansy, J.
"Toward reliable measurements of breast parenchymal patterns"
Proc 6th Conf on Computer Applications in Radiology and Computer Aided Analysis of Radiological Images,
Newport Beach, CA, June 1979, 118-121

[Lama85] Lamarque, J.-L.
An Atlas and Text of the Breast
Sheridan House Inc., Dobbs Ferry, 1985

[LLBi88] Lai, S., Li, X., Bischof, W.
"Automated detection of breast tumor"
Proceedings Vision Interface '88, June 1988, 35-40

[LLBi89] Lai, S., Li, X., Bischof, W.
"On techniques for detecting circumscribed masses in mammograms"
IEEE Transactions on Medical Imaging, **(8:4)**, December 1989, 377-386

[Loats88] Loats, H.L., Lloyd, D.G., Pittenger, M., Tucker, R.W., Unnerstall, J.R.
"Biomedical image analysis applications"
Imaging Techniques in Biology and Medicine
(Swenberg, C.E., Conklin, J.J. (Eds.))
Academic Press, Inc., San Diego, 1988, 1-75

[LOKS86] Lundahl, T., Ohley, W., Kay, S., Siffert, R.
"Fractional brownian motion: a maximum likelihood estimator and its application to image texture"
IEEE Transactions on Medical Imaging, **MI-5:3**, September 1986, 152-161

[LOKW86] Lundahl, T., Ohley, W., Kay, S., White, H., Williams, D., Most, A.
"Texture analysis of diagnostic x-ray images by use of fractals"
SPIE Visual Communications and Image Processing (1986), **707**, 1986, 23-30

[Mand83] Mandelbrot, B.B.,
The Fractal Geometry of Nature,
New York: W.H. Freeman and Company, 1983

[MaVN68] Mandelbrot, B.B. and Van Ness, J.W.
"Fractional Brownian motions, fractional noises and applications"
SIAM Review, **10 (4)**, October 1968, 422-437

[MASR84] Montague, E., Ames, F., Schell, S. and Romsdahl, M.
"Conservative surgery and irradiation as an alternative to mastectomy in the treatment of clinically favourable breast cancer"
Cancer, **54**, 1984, 2668-2672

[MCOB85] Magnin, I., Cluzeau, F., Odet, C., Bremond, A.
"Mammographic texture analysis: an evaluation of risk for developing breast cancer"
SPIE Application of Optical Instrumentation in Medicine XIII (1985), **535**, 1985, 378-384

[MeYa84] Medioni, G. and Yasumoto, Y.
"A note of using the fractal dimension for segmentation"
IEEE Proc. of the Workshop on Computer Vision Representation and Control, Annapolis, Maryland, 1984, 25-30

[Mosk87] Moskowitz, M.
"Benefit and Risk"
Breast Cancer Detection, 2nd Ed., (Bassett, L. and Gold, R. (Eds.))
Grune & Stratton, Inc., Orlando, 1987, 131-142

[Mosk88] Moskowitz, M.
"Breast Imaging"
Cancer of the Breast, 3rd Ed., (Donegan, W., and Spratt, J. (Eds.)),
W.B. Saunders Company, Philadelphia, 1988, 167-205

[MRSc87] Mussigmann, U., Rueff, M., Schmutz, M.
"Fractal based algorithms for texture analysis"
SPIE Automated Inspection and High Speed Vision Architectures (1987), **849**, 1987, 109-116

[OhLu87] Ohley, W.J., Lundahl, T.
"Discrete 2-dimensional fractional brownian motion as a model for medical images"
SPIE Visual Communications and Image Processing II (1987), **845**, 1987, 227-232

[Pent84] Pentland, A.
"Fractal-based description of natural scenes"
IEEE Transactions on Pattern Analysis and Machine Intelligence, **(PAMI-6:6)**, November 1984, 661-674

[Rabk87] Rabkin, I.
"Computer-assisted roentgenologic diagnosis of diseases of organs and systems"
Vestn Rentgenol Radiol (USSR), **313 (1)**, 1987, 7-10

[RaNg86] Rangayyan, R., and Nguyen, H.
"Pixel-independent Image processing tachniques for enhancement of features in mammograms"
IEEE/Eighth Annual Conference of the Engineering in Medicine and Biology Society, Fort Worth, Texas, 1986, 1113-1117

[RaSh87] Rabbani, M., and Shaw, R.
"The influence of grain threshold on quantum mottle in radiographic screen-film systems"
SPIE Medical Imaging, **767**, 1987, 226-235

[SBDS86] Smathers, R., Bush, E., Drace, J., Stevens, M., Sommer, F., Brown Jr., B., Karras, B.
"Mammographic microcalcifications: detection with xerography, screen-film, and digitized film display"
Radiology, **159 (3)**, June 1986, 673-677

[Selz84] Selzer, R.
"Computer processing of radiographic images'
SPIE Diagnostic Imaging Applications, **516**, 1984, 16-27

[SiHo71] Silverberg, F., Holleb, A.
"Cancer statistics"
C. Cancer J. Clinc., **21**, 1971, 13-31

[Spie79] Spiesberger, W.
"Mammogram inspection by computer"
IEEE Trans Biomed Eng, **(BME-26)**, 1979, 213-219

[SSWA85] Sommer, F., Smathers, R., Wheat, R., Alvarez, R. Brody, W., and Cassel, D.
"Digital processing of film radiographs"
AJR, **144 (1)**, 1985, 191-196

[StHa88] Stein, M. and Hartt, K.
"Nonparametric estimation of fractal dimension"
SPIE Visual Communications and Image Processing '88, **1001**, 1988, 132-137

[SWGS77] Smith, K.T., Wagner, S.L., Guenther, R.B., Solmon, D.C.
"The diagnosis of breast cancer in mammograms by the evaluation of density patterns"
Radiology, **125**, 1977, 383-386

[Vehel90] Vehel, J.L.
"About lacunarity, some links between fractal and integral geometry, and an application to texture segmentation"
IEEE Proceedings Third International Conference on Computer Vision, Osaka, Japan, December 4-7 1990, 380-384

[Vern87] Vernazza, G.
"Performances of different fractal-dimension extimators of natural image texture"
Applied Control, Filtering and Signal Processing: Proceedings of the IASTED International Symposium, 1987, 138-142

[Voss85] Voss, R.F.
"Random fractal forgeries"
Fundamental Algorithms for Computer Graphics (Ed. Earnshaw, R.A.) Springer-Verlag, Berlin Heidelberg, 1985, 805-835

[VZLu86] Veronesi, U., Zucali, R., and Luini, A.
"Local control and survival in early breast cancer: the Milan trial"
Int Jour Radiat Oncology Biol Phys, **12**, 1986, 717-720

[WeGo87] West, B.J., Goldberger, A.L.
"Physiology in Factal Dimensions"
American Scientist, (**75**), July-August 1987, 354-365.

[Whit84] White, A.
"Early detection of breast microcalcification"
Proc. of the Second South African Symposium on Digital Image Processing, July 1984, 114-127

[Wins67] Winsberg, F., Elkin, M., Macy, J., Bordas, V., Weymouth, W.
"Detection of radiographic abnormalities in mammograms by means of optical scanning and computer analysis,"
Radiology, **89**, 1967, 211-215

[WMCT75] Wee, W.G., Moskowitz, M., Chang, N.C., Ting, V.C., Pemmeraju, S. "Evaluation of mammographic calcification using a computer program" *Radiology*, **116**, 1975, 717-720

[Wolf83] Wolfe, J.N., *Xeroradiography of the Breast*, 2nd Ed. Charles C Thomas Publisher, Springfield, Illinois, 1983

[Yu83] Yu, F.T.S. *Optical Information Processing* New York: John Wiley & Sons, 1983, 102-128

[ZhGo88] Zhou, X., Gordon, R. "Detection of early breast cancer: an overview and future prospects" *CRC Critical Reviews in Biomedical Engineering*, **17(3)**, 1989, 203-255